DISS. ETH NO. 27387

EMERGENCE AND EVOLUTION OF FERROELECTRICITY IN OXIDE HETEROSTRUCTURES

A thesis submitted to attain the degree of

DOCTOR OF SCIENCES of ETH ZURICH
(Dr. sc. ETH Zurich)

presented by

NIVES STRKALJ

M. Sc. in Physics, University of Zagreb
born on 04.04.1992
citizen of Croatia

accepted on the recommendation of

Prof. Dr. Manfred Fiebig
Prof. Dr. Morgan Trassin
Prof. Dr. Nicola A. Spaldin
Prof. Dr. Patrycja Paruch
2021

Declaration of originality

I hereby declare that the following submitted thesis is original work which I alone have authored and which is written in my own words.

Title: Emergence and evolution of ferroelectricity in oxide heterostructures

Author: Nives Strkalj

Supervisor: Prof. Dr. Manfred Fiebig

With my signature I declare that I have been informed regarding normal academic citation rules and that I have read and understood the information on “Citation etiquette". The citation conventions usual to the discipline in question here have been respected.

Furthermore, I declare that I have truthfully documented all methods, data, and operational procedures and not manipulated any data. All persons who have substantially supported me in my work are identified in the Acknowledgement and Contributions to this thesis.

The above work may be tested electronically for plagiarism.

Zurich, 15.01.2021

Nives Strkalj

Acknowledgment

I am deeply grateful for the support that I have received throughout my PhD studies from my colleagues, friends and family.

First and foremost, I would like to thank Prof. Dr. Manfred Fiebig and Dr. Morgan Trassin for giving me the opportunity to work on an exciting research project and a pioneering experimental setup. Your strive for excellence, never-ending optimism, and unselfishness in passing the knowledge to your students shaped my course as a researcher. I would also like to thank Prof. Dr. Nicola A. Spaldin, Prof. Dr. Patrycja Paruch, and Prof. Dr. Pietro Gambardella for taking part in my thesis committee.

This work would not have been possible without collaborations outside and within the FERROIC group. I want to express my gratitude to you all. I would like to especially thank Prof. Dr. Nicola A. Spaldin and Dr. Chiara Gattinoni for their support with ab initio calculations. Sharing their interest in the intricate effects of interfaces on ferroelectricity in thin films has helped build the core of this work. Furthermore, I thank Dr. Marta D. Rossell, Dr. Marco Campanini and Alexander Vogel for their support with STEM analysis.

I would like to thank the FERROIC group for an amazing working atmosphere which made my time with you very rewarding. In particular, I would like to thank the NEAT lab for enriching my understanding of oxide heterostructures. I thank Dr. Johanna Nordlander for experiencing many of the joys and troubles of PhD life in parallel with me which enhanced the former and mildened the latter. I thank Dr. Gabriele De Luca for introducing me to optical characterization, in particular second-harmonic generation. I thank Dr. Jakob Schaab, Elzbieta Gradauskaite and Marco Bernet for sharing their expertise in PFM measurements. I thank Dr. Thomas Weber and Martin Sarott for the help with the XRD analysis of superlattices. I thank Amadé Bortis for his work on the model of SHG response of phase coexistence. I thank Prof. Dr. Shovon Pal for terahertz time-domain spectroscopy measurements and many great discussions.

I would also like to thank Chia-Jung Yang for the excercise sessions, for keeping secrets and for being a good friend. I thank Dr. Jannis Lehmann for his encouragements and for sharing a passion for all things lab-related. I thank Dr. Lukas Kürten and his family for helping me and my family survive home-office.

Hvala dragim prijateljima i kolegama u Zürichu na lijepim zajedničkim trenucima. Hvala mom suprugu Antoniju, na sreći kojom mi obasjava život, na idealizmu i na hrabrosti. Hvala našem sinu Petru što nas podsjeća na bitno. Hvala i našim obiteljima što su nam pružile čvrst temelj, sigurnu luku i dobar primjer. Posebno hvala mojoj obitelji što me od malena podržavala u bavljenju prirodnim znanostima. Hvala mojim noni i didi što su me poticali da sanjam velike snove.
Hvala Gospodine.

Abstract

Oxide heterostructures have emerged over the last decade as a promising platform for energy-efficient electronics. Among oxides, ferroelectric materials, owing to their spontaneous polarization that can be controlled by an electric field, stand out as natural memory elements for low-power devices. In devices, thin films of ferroelectric materials need to be prepared with a high degree of control over the ferroelectric response. Regions of a ferroelectric material where electric-dipole moments point in the same direction are referred to as domains. Domain structure is the key property in applications because it determines the switching path of polarization and possible polarization states.

The domain structure is commonly set already during the integration of a ferroelectric layer into a heterostructure. The two interfaces of a ferroelectric layer, the interface towards the substrate (bottom) and the interface towards the surface (top), predominantly govern the ferroelectric response. While the influence of the bottom interface is set already *during* the deposition of the ferroelectric layer, the influence of the top interface evolves even *after* the deposition of the ferroelectric layer. Understanding the ferroelectric response of a thin film thus requires understanding the interplay of the contributions of the two interfaces. However, disentangling the contributions of interfaces is difficult post-deposition, and conventional techniques for the characterization of ferroelectric materials cannot be used during the thin-film synthesis.

In this thesis, we use second harmonic generation as a non-invasive nonlinear optical tool for directly investigating the emergence and evolution of ferroelectricity in oxide heterostructures. We develop the use of in situ second harmonic generation to study ferroelectricity during the thin-film deposition in real time. We use this approach, which is unique in the world, to study ferroelectricity in two model systems: barium titanate and lead titanate.

In the first two projects, we unravel the dynamics of the polarization during the growth of ferroelectric-based heterostructures. We first study the dynamics of polarization during the integration of the ferroelectric layer into a prototypical device architecture of a capacitor. Surprisingly, we observe a polarization suppression during the deposition of the top electrode as a result of the transiently insufficient charge screening at the top interface. This insight enables us to stabilize a robust single-domain configuration in a ferroelectric-based capacitor.

We take this a step further to explore the interface-governed polarization in the second project. We observe only the influence of the bottom interface on the polarization direction during the growth and the influence of both interfaces on the polarization direction once the growth is halted. We establish the concept of competition and cooperation of interfaces in the setting of the polarization direction. We find that in the case of matching interface contributions, we can even stabilize a robust single-domain configuration in an unfavorable electrostatic environment.

In the next two projects, we move on to investigating complex arrays of dipole moments and ordered multi-domain structures in ferroelectric|dielectric multilayers. Using the non-invasive optical characterization ex-situ, we detect phase coexistence and interlayer coupling of polarization in such multilayers. We furthermore manipulate an ordered multi-domain configuration forming at the nanoscale into stable single-domain regions using electric fields of a scanning-probe tip.

The results presented in this thesis demonstrate that the thin-film synthesis is the decisive point for setting the ferroelectric response that is observed post-deposition. The developed approach for monitoring polarization during the growth is thus essential for understanding and engineering polarization in ferroelectric-based heterostructures. Our observation of the emergence and evolution of ferroelectricity in oxide heterostructures not only complements the standard characterization, but allows access to previously overlooked polarization dynamics. The access to these transient polarization states that occur during the synthesis is instrumental in explaining the often unexpected ferroelectric response once the synthesis is completed. Moreover, based on the information obtained during the synthesis, we tune the growth process to stabilize the coveted robust single-domain polarization in the ultrathin regime. We furthermore show the potential of following the same approach in studying more complex ordering of dipole moments and open up a path towards the use of this approach operando. Ultimately, we provide new routes to engineer the domain structure in ferroelectric layers displaying improved functionalities.

Zusammenfassung

Oxidische Heterostrukturen haben sich im letzten Jahrzehnt als vielversprechende Plattform für energieeffiziente Elektronik entwickelt. Unter den Oxiden zeichnen sich ferroelektrische Materialien aufgrund ihrer spontanen Polarisation, die durch ein elektrisches Feld gesteuert werden kann, als natürliche Speicherelemente für Geräte mit niedrigem Stromverbrauch aus. In Geräten müssen dünne Schichten aus ferroelektrischen Materialien mit einem hohen Grad an Kontrolle über die ferroelektrische Reaktion hergestellt werden. Bereiche eines ferroelektrischen Materials, in denen die elektrischen Dipolmomente in dieselbe Richtung zeigen, werden als Domänen bezeichnet. Die Domänenstruktur ist die Schlüsseleigenschaft in der Anwendung, da sie den Schaltweg der Polarisation und die möglichen Polarisationszustände bestimmt.

Die Domänenstruktur wird in der Regel bereits bei der Integration einer ferroelektrischen Schicht in eine Heterostruktur festgelegt. Die beiden Grenzflächen einer ferroelektrischen Schicht, die Grenzfläche zum Substrat (unten) und die Grenzfläche zur Oberfläche (oben), bestimmen maßgeblich das ferroelektrische Verhalten. Während der Einfluss der unteren Grenzfläche bereits während der Abscheidung der ferroelektrischen Schicht festgelegt wird, entwickelt sich der Einfluss der oberen Grenzfläche sogar erst nach der Abscheidung der ferroelektrischen Schicht. Um das ferroelektrische Verhalten einer dünnen Schicht zu verstehen, muss man also das Zusammenspiel der Beiträge der beiden Grenzflächen verstehen. Es ist jedoch schwierig, die Beiträge der Grenzflächen nach der Abscheidung zu entwirren, und herkömmliche Techniken zur Charakterisierung ferroelektrischer Materialien können während der Dünnschichtsynthese nicht verwendet werden.

In dieser Arbeit verwenden wir die Erzeugung der zweiten Harmonischen als nicht-invasives nichtlinear-optisches Werkzeug, um die Entstehung und Entwicklung der Ferroelektrizität in oxidischen Heterostrukturen direkt zu untersuchen. Wir entwickeln den Einsatz der in situ Erzeugung der zweiten Harmonischen, um die Ferroelektrizität während der Dünnschichtabscheidung in Echtzeit zu untersuchen. Wir nutzen diesen weltweit einzigartigen Ansatz, um die Ferroelektrizität in zwei Modellsystemen zu untersuchen: Bariumtitanat und Bleititanat.

In den ersten beiden Projekten entschlüsseln wir die Dynamik der Polarisation während des Wachstums von Heterostrukturen auf ferroelektrischer Basis. Zunächst untersuchen wir die Dynamik der Polarisation während der Integra-

tion der ferroelektrischen Schicht in eine prototypische Bauelementarchitektur eines Kondensators. Überraschenderweise beobachten wir eine Polarisationsunterdrückung während der Abscheidung der oberen Elektrode als Folge der vorübergehend unzureichenden Ladungsabschirmung an der oberen Grenzfläche. Diese Erkenntnis ermöglicht es uns, eine robuste Single-Domain-Konfiguration in einem ferroelektrisch basierten Kondensator zu stabilisieren.

Wir gehen noch einen Schritt weiter und untersuchen die grenzflächengesteuerte Polarisation im zweiten Projekt. Wir beobachten nur den Einfluss der unteren Grenzfläche auf die Polarisationsrichtung während des Wachstums und den Einfluss beider Grenzflächen auf die Polarisationsrichtung, sobald das Wachstum gestoppt ist. Wir etablieren das Konzept der Konkurrenz und Kooperation von Grenzflächen bei der Einstellung der Polarisationsrichtung. Wir finden, dass wir im Falle übereinstimmender Grenzflächenbeiträge sogar eine robuste Single-Domain-Konfiguration in einer ungünstigen elektrostatischen Umgebung stabilisieren können.

In den nächsten beiden Projekten gehen wir dazu über, komplexe Anordnungen von Dipolmomenten und geordnete Multidomänenstrukturen in ferroelektrischen|dielektrischen Multilayern zu untersuchen. Mit Hilfe der nichtinvasiven optischen Charakterisierung ex-situ detektieren wir die Phasenkoexistenz und die Interlayer-Kopplung der Polarisation in solchen Multilayern. Des Weiteren manipulieren wir eine geordnete Multidomänenkonfiguration, die sich auf der Nanoskala bildet, mit Hilfe elektrischer Felder einer Scanning-Probe-Spitze in stabile Einzeldomänenbereiche.

Die in dieser Arbeit vorgestellten Ergebnisse zeigen, dass die Dünnschichtsynthese der entscheidende Punkt für die Einstellung der ferroelektrischen Antwort ist, die nach der Abscheidung beobachtet wird. Der entwickelte Ansatz zur Überwachung der Polarisation während des Wachstums ist daher essentiell für das Verständnis und das Engineering der Polarisation in ferroelektrisch basierten Heterostrukturen. Unsere Beobachtung der Entstehung und Entwicklung der Ferroelektrizität in Oxid-Heterostrukturen ergänzt nicht nur die Standardcharakterisierung, sondern ermöglicht auch den Zugang zu bisher übersehenen Polarisationsdynamiken. Der Zugang zu diesen transienten Polarisationszuständen, die während der Synthese auftreten, ist entscheidend für die Erklärung der oft unerwarteten ferroelektrischen Reaktion nach Abschluss der Synthese. Basierend auf den Informationen, die wir während der Synthese erhalten, können wir den Wachstumsprozess so abstimmen, dass die begehrte robuste Single-Domain-Polarisation im ultradünnen Bereich stabilisiert wird. Darüber hinaus zeigen wir das Potenzial des gleichen Ansatzes bei der Untersuchung komplexerer Anordnungen von Dipolmomenten und eröffnen einen Weg zur Anwendung dieses Ansatzes operando. Letztendlich bieten wir neue Wege, um die Domänenstruktur in ferroelektrischen Schichten mit verbesserten Funktionalitäten zu entwickeln.

Contents

1 Introduction 1

2 Ferroelectric thin films 5
- 2.1 Ferroelectricity 5
  - 2.1.1 Electrostatics of electric polarization 5
  - 2.1.2 Electric polarization in materials 6
- 2.2 Depolarizing field in ferroelectric thin films 9
  - 2.2.1 Effects of screening of electric field on out-of-plane polarization in thin films with a finite thickness 10
  - 2.2.2 Comparison with magnetism 11
- 2.3 Engineering the domain structure in epitaxial films 11
  - 2.3.1 Charge screening 12
  - 2.3.2 Epitaxial strain 13
- 2.4 Ferroelectric-based applications 15

3 Experimental methods 17
- 3.1 Pulsed laser deposition 17
- 3.2 Optical second harmonic generation 19
  - 3.2.1 Experimental setup 20
  - 3.2.2 Optical second harmonic generation in thin films 21
- 3.3 In-situ optical second harmonic generation 23
  - 3.3.1 Experimental setup 24
  - 3.3.2 Critical thickness of ferroelectric thin films 25
  - 3.3.3 Curie temperature of ferroelectric thin films 25
- 3.4 Scanning probe microscopy 25
- 3.5 X-ray diffraction 26
- 3.6 Scanning transmission electron microscopy 28
- 3.7 Terahertz time-domain spectroscopy 28
- 3.8 X-ray photoelectron spectroscopy 30

4 Transient electrostatics in ferroelectric-based capacitors 33
- 4.1 Polarization suppression in ferroelectric-based capacitors 34

4.2 Transient enhancement of depolarizing field 35
4.3 Discussion and outlook 36

5 Polarization dynamics in ultrathin ferroelectrics 39
5.1 Separation of the impact of an individual interface on the polarization state 40
5.2 Consequences of competitive and cooperative configurations of interfaces 41
5.3 Discussion and outlook 43

6 Non-invasive probing of phase coexistence in ferroelectric|dielectric heterostructures 45
6.1 Ordering of dipole moments in a ferroelectric|dielectric superlattice 46
6.2 Optical response of phase coexistence 47
6.3 Discussion and outlook 48

7 Manipulation of in-plane polarization using electric trailing field 51
7.1 Stabilization of in-plane polarization 51
7.2 Manipulating nanoscale domains with in-plane polarization by the electric trailing field 52
7.3 Discussion and outlook 53

8 Conclusion and outlook 55

Contributions to this thesis 57

Appendices 59

A Depolarizing-field effects in epitaxial heterostructures 61

B In-situ monitoring of interface proximity effects on polarization in ultrathin ferroelectrics 69

C Optical second harmonic signature of phase coexistence in ferroelectric|dielectric heterostructures 77

D Stabilization and manipulation of in-plane polarization in a ferroelectric-dielectric superlattice 93

Glossary 101

Bibliography 103

Data accessibility 121

Introduction

1

The amount of created and stored data is growing exponentially [1]. Storing and processing these requires increasing amounts of electric energy. The global demand for electric energy for electronic devices is thus on a constant rise, which presents a societal challenge in the face of the climate crisis [2]. The search for materials for energy-efficient devices is an important part of solving this challenge.

In electronic applications, materials are used in their thin-film form. For reliable applications, a high level of control over the functional property needs to be achieved. The prerequisite of a controlled functional property is the production of “ideal” films, i. e. epitaxial films with low defect levels. In the last 20 years, in addition to semiconductor films, it is also possible to produce thin films of most complex oxides with comparably high quality [3, 4]. Oxides are attractive components for the next generation of electronic devices because they exhibit a wide range of easily tunable properties that are not present in semiconductors. In the broad emerging field of oxide electronics, ferroelectric thin films, as studied in this thesis, emerge as a promising platform for low-power devices [5–9].

Since the discovery of ferroelectricity in Rochelle salt in 1920 by J. Valasek [10], ferroelectrics, especially oxides with perovskite structure, are increasingly used for their pyroelectric and piezoelectric properties, their high dielectric constant and their nonlinear optical effects. More recently, ferroelectric films exploiting the polarization itself are developed for energy-efficient device components. For example, the local dipole moments inside the ferroelectric can be understood as “natural” bit elements for ferroelectric-based memories [11–15]. The advantage of ferroelectric-based memories to the currently widespread memories is their energy-efficiency because the memory state is non-volatile and set with electric fields.

Ferroelectric materials are implemented in devices in the form of ultrathin films that have a thickness of only a few nanometers. The ferroelectric properties of such thin films are highly susceptible to the influence of their interfaces [16]. Epitaxial strain imposed by the substrate enhances the ferroelectric-paraelectric transition temperature, often above the growth temperature. As a result, the polarization is already determined during growth. However, in a typical growth chamber, there are only means for monitoring the structural sample quality, but not the functional property of the film (its ferroelectricity). Additionally, most samples are heterostructures that consist of several layers which influence each other's properties in ways which are difficult to disentangle after the growth. The lack of control over polarization during the thin-film synthesis and integration of ferroelectric layers into heterostructures leads to unreliable polarization properties which hinder their use in applications.

Here we seek to illuminate the specific properties that arise during the deposition of ultrathin ferroelectric films. Detecting and controlling the polarization in ultrathin ferroelectric layers extends throughout this thesis. We explore the physics of polarization in prototypical systems of ferroelectrics with perovskite structure using a non-invasive nonlinear optical method [17, 18]. Such optical probing of polarization states is ideal for in-situ and operando measurements. Ultimately, this work sheds light on the emergence and evolution of ferroelectricity, vital for designing the polarization for targeted applications [19, 20].

The following main questions form the cornerstones of this thesis:

(1) **What previously inaccessible polarization dynamics can we unravel with nonlinear optics during the deposition of ultrathin ferroelectric films?** Understanding the ferroelectric response of a ferroelectric-based heterostructure is difficult because of the combined effect of interfaces, which cannot be easily disentangled post-deposition . We access the polarization dynamics during the growth of ultrathin films to explain the surprising ferroelectric response post-deposition. For example, we evidence the polarization suppression during the integration of a ferroelectric layer into a ferroelectric-based capacitor [21–24] and the polarization reconstruction under the effects of defect formation at ferroelectric interfaces [25–28].

(2) **How can we use this new access to polarization during the film growth via nonlinear optics to favor a desired ferroelectric response?** Engineering the polarization has so far been restricted to only one interface [29–36]. By observing the polarization at each stage of heterostructure growth, we can evaluate the individual contributions of interfaces in the setting of the domain structure and the polarization direction of a ferroelectric layer. We use these findings to tune the growth process and the heterostructure itself to stabilize robust single-domain configurations in the ultrathin regime.

(3) **Can we use nonlinear optics to characterize the more complex ordering of dipole moments in multilayers and can we deterministically manipulate polarization in such structures using electric fields?** Identification of so-called complex arrays of dipole moments typically relies on destructive or arduous methods [37–45]. We non-invasively detect the presence of phase coexistence and interlayer coupling using nonlinear optics, which could be invaluable for future operando studies. In a related system hosting an ordered multi-domain structure, we perform another step towards operando studies: controlled manipulation of polarization with electric fields.

The thesis is structured as follows:

In **Chapter 2**, we introduce ferroelectricity, the depolarizing field, the engineering of the domain structure in epitaxial films, and ferroelectric-based applications. We explain these concepts in relation to the challenges of integrating ultrathin ferroelectrics into device architectures and introduce the model systems investigated in this thesis.

Chapter 3 provides an overview of the experimental techniques used throughout this thesis for the structural and ferroelectric characterization of films. In addition to the brief introductions of standard characterization techniques, we elaborate on optical second harmonic generation as the main characterization technique of this work. The emphasis is on its unique implementation into the pulsed laser deposition process, which enables tracking the emergence and evolution of ferroelectricity during growth.

Chapter 4 and **Chapter 5** are devoted to addressing (1) and (2) i. e., to transient phenomena during the growth of ferroelectric-based heterostructures. In **Chapter 4**, we discuss charge screening at ferroelectric interfaces in $BaTiO_3$-based capacitor. We present the observation of the emergence of polarization during the growth of the ferroelectric layer and an unexpected suppression of polarization during the growth of the top electrode. We find the origin of this net polarization suppression in the thickness-dependent charge screening properties of the top electrode. The understanding of the origin of the polarization suppression leads us to a path to stabilize robust net polarization in a ferroelectric-based capacitor. In **Chapter 5**, we investigate the polarization dynamics during ongoing and halted growth of a ferroelectric layer to separate the impact of individual interfaces on the polarization state in $PbTiO_3$. We develop the concept of interface configurations which determine the polarization state in a ferroelectric film with polarization perpendicular to the sample plane. We present the consequences of interface configurations on the polarization state post-deposition and identify a configuration with a robust polarization in unfavorable electrostatic conditions.

In **Chapter 6** and **Chapter 7**, we move on to (3) i. e. to studying polarization ordering that arises in ferroelectric|dielectric multilayers of $PbTiO_3|SrTiO_3$ with a net polarization parallel to the sample plane. In **Chapter 6**, we detect phase coexistence and interlayer coupling of polarization using the non-invasive tabletop approach discussed above: second harmonic generation. In **Chapter 7**, we manipulate the as-grown multi-domain structure in ferroelectric|dielectric superlattice to single domain regions using in-plane electric trailing fields.

Ferroelectric thin films

2

2.1 Ferroelectricity

Ferroics are materials that are characterized by their switchable long-range ordered structure, which can be in shape (ferroelastic), charge (ferroelectric) or magnetic moment (ferromagnetic). An extensive description of ferroics can be found in *Introduction to Ferroic Materials* by Vinod K. Wadhawan [46], and *Introduction to Solid State Physics* by C. Kittel [47]. I discuss here the basic properties of ferroelectric materials. A longer description of ferroelectrics can be found in, for example, *Principles and Applications of Ferroelectrics and Related Materials* by M. E. Lines and A. M. Glass [48].

2.1.1 Electrostatics of electric polarization

We consider the electrostatics of electric polarization, first for the case of a single electric dipole and then for a polarized medium.

Electric dipole

A pair of electric charges of equal magnitude q but opposite sign, separated by a distance d, is termed an electric dipole. The dipole moment **p** of this pair of charges can be expressed as $\mathbf{p} = q\mathbf{d}$, where **d** is the displacement vector. By convention, the direction of the dipole moment is chosen to be from the negative charge to the positive charge. When following this convention, the electric dipole is aligned parallel to the external electric field $\mathbf{E}_{\mathrm{ext}}$, see Fig. 2.1(a).

The electric field produced by an electric dipole is equivalent to the field of its two constituent charges, and at a distance $z \gg d$ equals

$$\mathbf{E}_{\mathrm{dip}} = \frac{1}{4\pi\varepsilon_0}\frac{-\mathbf{p}}{z^3}, \tag{2.1}$$

where ε_0 is the electric constant. Within the dipole, the electric field produced by the two constituent charges is opposite to the direction of the dipole moment, see Fig 2.1(b).

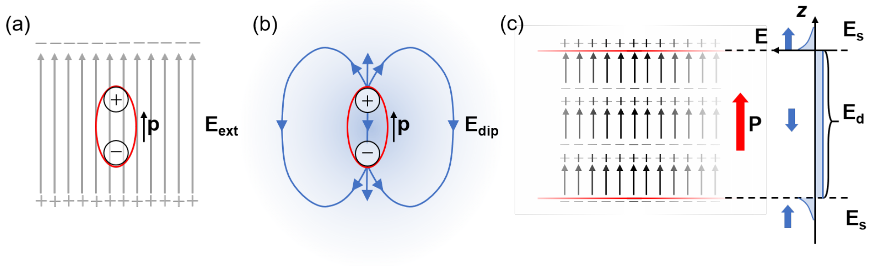

Figure 2.1: (a) Schematic of the alignment of an electric dipole with a dipole moment **p** in an external electric field $\mathbf{E_{ext}}$. (b) Schematic of the electric field $\mathbf{E_{dip}}$ that is produced by an electric dipole. (c) Schematic of the dipole moments and bound charge in a polarized medium. The resulting magnitude and direction of the electric field **E** inside and outside are shown at different positions z. The electric field inside the medium is termed the depolarizing field $\mathbf{E_d}$ and the electric field outside the medium is termed the electric stray field $\mathbf{E_s}$.

Polarized medium

The discussion below applies to the macroscopic scale, while microscopic fields inside a polarized medium depend on the choice of the inspected volume and the exact position with respect to the local dipole moments.

In a polarized medium, a macroscopic number of aligned dipole moments can be identified. The polarization **P** is defined as the dipole moment per unit volume. The electric field that is induced by the polarization itself is equivalent to the sum of the electric fields produced by all charges within the polarized medium. This electric field can be found to correspond to the field of the bound charge at the interface $\sigma_\mathrm{b} \equiv \mathbf{P} \cdot \hat{\mathbf{n}}$ and the bound charge in the volume $\rho_\mathrm{b} \equiv -\nabla \cdot \mathbf{P}$. For uniformly polarized media, the electric field in the medium is equivalent to the electric field of the bound charge at the interface, see Fig. 2.1(c). The electric field is produced by the bound charge both *outside* the polarized medium, as well as *inside* the medium. Inside the medium, the electric field is opposite to the direction of the polarization and is therefore termed the depolarizing field $\mathbf{E_d}$. Outside the medium, the electric field is termed the electric stray field $\mathbf{E_s}$.

2.1.2 Electric polarization in materials

Electric polarization in materials commonly occurs on the level of the unit cell (u. c.) of a polar crystal by the formation of local dipole moments. Dipole moments arise from two contributions: the electronic contribution that results from the displacement of the electronic shells with respect to the atomic core and the ionic contribution that results from the displacement of ions with respect to each other.

Electric polarization in materials can be either spontaneous or induced by an electric field.

The appearance of a spontaneous polarization $\mathbf{P_s}$ can be understood to be a result of freezing of a phonon mode that is referred to as the "soft mode" [49, 50]. In this case, the polar configuration is energetically more stable than the non-polar configuration. Materials exhibiting spontaneous polarization are called pyroelectric. In the absence of external fields, the electric displacement field is related to the polarization and its electric field as

$$\mathbf{D} = \varepsilon_0 \mathbf{E} + \mathbf{P}. \tag{2.2}$$

Additionally, polarization can be induced by an external electric field in so-called dielectric materials. In the linear approximation, polarization induced by an external electric field equals $\mathbf{P_{ind}} = \varepsilon_0 \chi \mathbf{E_{ext}}$, where χ is the susceptibility of a material. The induced electric displacement field is

$$\mathbf{D_{ind}} = \varepsilon_0 \mathbf{E_{ext}} + \mathbf{P_{ind}} \varepsilon_0 (1 + \chi) \mathbf{E_{ext}} = \varepsilon_0 \varepsilon_r \mathbf{E_{ext}}, \tag{2.3}$$

where ε_r is the relative permittivity of a material $\varepsilon_r = \chi + 1$.

Ferroelectrics

Ferroelectrics are materials possessing a spontaneous electric polarization $\mathbf{P_s}$ that can be reoriented through the application of an external electric field.

In ferroelectrics, there are either two or more degenerate polarization states. Different polarization states can coexist within a ferroelectric material. Each region with a uniform polarization state is called a domain, and two domains are separated by a domain wall. An abstract arrangement of polarization in domains with respect to domain walls is referred to as a domain structure. Ordered multi-domain structures arise to satisfy competing local and non-local energetics [51, 52]. A specific arrangement of domains in a sample is referred to as a domain configuration.

Ferroelectrics have a hysteretic dependence of polarization on electric field, meaning that there is a finite coercive field E_c at which the polarization direction is reversed (Fig. 2.2(a)). Ferroelectricity disappears above a Curie temperature T_C at which the material becomes paraelectric (Fig. 2.2(b)).

Doman size

The domain size w in all ferroic films typically scales according to the square root of the film thickness t [52–55]: $w = \beta\sqrt{t}$, where β a prefactor that depends on the typical length scale of domain walls, which is in the case of ferroelectrics about 6 $\mathrm{nm}^{1/2}$ [56–58]. When the domain size is below the film thickness, the square-root law is no longer obeyed, and the equilibrium domain size is predicted to increases with decreasing film thickness [59, 60].

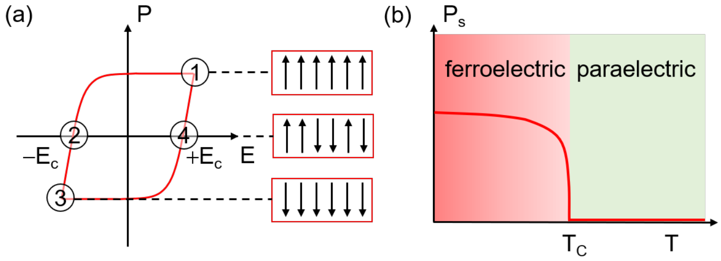

Figure 2.2: (a) Idealized hysteretic dependence of polarization P in a ferroelectric on electric field E. The coercive field is indicated as E_c. ①,③ A single-domain configuration. ②,④ A multi-domain configuration with no net polarization. (b) Temperature dependence of spontaneous polarization P_s in a ferroelectric material with a Curie temperature T_C.

Materials

In this thesis, we focus on the technologically most important ferroelectrics: oxides with a perovskite structure. The structure of perovskite oxides with the chemical formula ABO_3 consists of alternating atomic planes of AO and BO_2, as schematized in Fig. 2.3(a).

The tetragonal crystal structure can be described as a rectangular prism with a square base *a* by *a* and height *c*. Domains with polarization along *a* are referred to as *a*-domains. More specifically, *a*-domains with polarization along [100] are termed a_1-domains and domains with polarization along [010] are termed a_2-domains. Domains with polarization along the base diagonal are referred to as *aa*-domains. In analogy, *aa*-domains with polarization along [110] are termed aa_1-domains and domains with polarization along $[1\bar{1}0]$ are termed aa_2-domains. Domains with polarization along *c* are referred to as *c*-domains.

The local dipole moments are a result of the ionic (B-site and oxygen) and electronic displacement with respect to the center of mass of the A-site ions. We use here the two classic examples of ferroelectric perovskites, $BaTiO_3$ (BTO) and $PbTiO_3$ (PTO), as model systems. Both of these systems exhibit a tetragonal crystal structure with 4*mm* point-group symmetry in the ferroelectric phase. The electric dipole moment in BTO results from the ionic displacement of the titanium ion with respect to the barium and oxygen ions and points in the direction of the titanium-ion displacement [61, 62], see Fig. 2.3(b-d). The dipole moment in PTO additionally has significant contributions from the displacement of the electrons (lead 6s lone pair) and oxygen ions [63–65] with respect to the lead ions. In the case of PTO, these additional contributions reverse the direction of the dipole moment with respect to the direction of the titanium-ion displacement. An overview of properties of BTO [66, 67] and PTO [68, 69] is given in Table 2.1.

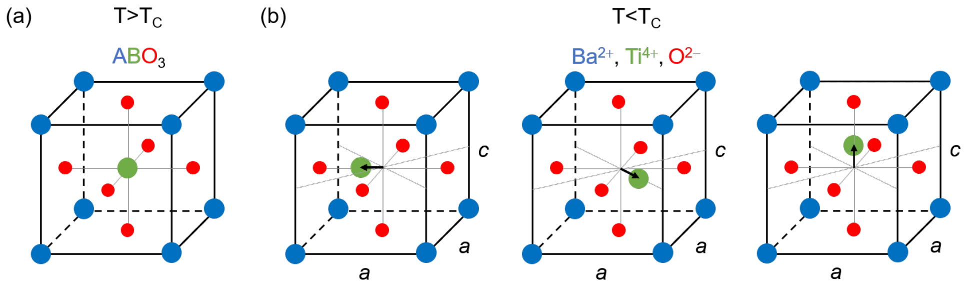

Figure 2.3: (a) Schematic of the perovskite crystal structure. (b–d) Schematic of ionic displacement (black arrow) of the Ti^{4+} cation (b) along the *a* edge of the u. c. (left), (c) along the base diagonal (middle), and (d) along the *c* edge of the u. c. (right).

	point group	T_C (°C)	P_s (μC/cm^2)	*a* (Å)	*c* in (Å)	*c*/*a*
BTO	4*mm*	120	26	3.996	4.034	1.0095
PTO	4*mm*	490	60	3.905	4.130	1.0590

Table 2.1: An overview of the point group, Curie temperature T_C, spontaneous polarization P_s and lattice constants at room temperature for BTO and PTO.

2.2 Depolarizing field in ferroelectric thin films

The ferroelectric properties of thin films significantly differ from those of their bulk counterparts because of the increasing role of the film's interfaces with the decreasing film thickness. We will discuss one of the limiting aspects for the technological advancement of ferroelectric thin films: the effects of the depolarizing field.

The energy minimum of the system is a balance between the energy reduction from the spontaneous displacement of charges in a polarized medium and the energy increase associated with the resulting electric field. The energy reduction from the spontaneous displacement of charges in a polarized medium is proportional to the volume of the material. The energy increase associated with the electric field produced by a polarized medium is [48]

$$W = \frac{1}{2}\int_V \mathbf{D}\cdot\mathbf{E}\,\mathrm{d}V, \tag{2.4}$$

where V is the volume of the medium. To reduce W, we need to suppress the net polarization or screen the bound charge because $\mathbf{E}$ arises from the bound charge at the interface of the polarized medium.

Because of its origin, the depolarizing field $\mathbf{E_d}$, as defined in Subsection 2.1.1, depends on the geometry of the system and the orientation of the polarization. This relation can be described using a depolarizing tensor for a general ellipsoid shape of the system. In specific cases, the depolarizing tensor can be expressed as a simple factor. For example, for a uniformly polarized sphere we have $\mathbf{E_d} = -\frac{1}{3\varepsilon_0}\mathbf{P}$, for an infinitely thin film with a polarization perpendicular to the film surface (out-of-plane) $\mathbf{E_d} = -\frac{1}{\varepsilon_0}\mathbf{P}$ and for a film with a polarization parallel to the film surface (in-plane) $\mathbf{E_d} = 0$.

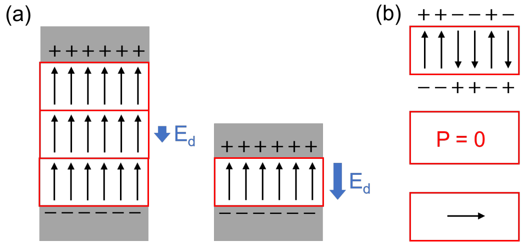

Figure 2.4: (a) Schematic of the dipole moments (black arrows) and bound charge for decreasing thickness of a ferroelectric-based capacitor in which the polarization points out-of-plane. The resulting electric field inside the film is termed the depolarizing field $\mathbf{E_d}$. (b) Schematics of possible scenarios of net polarization suppression: splitting into a multi-domain configuration (top), reduction of Curie temperature (middle), rotation of polarization to in-plane (bottom).

2.2.1 Effects of screening of electric field on out-of-plane polarization in thin films with a finite thickness

The balance between the energy reduction from the spontaneous displacement of charges in a polarized medium and the energy increase associated with the resulting electric field depends on the film thickness $d > 0$ and the screening environment. For simplicity, we consider a ferroelectric-based capacitor in which the polarization **P** of the ferroelectric layer is independent of thickness. For ideal screening of surface charge at the ferroelectric interfaces by the mobile charge in the electrodes, there is no remaining depolarizing field ($\mathbf{E_d} = 0$) and polarization can be stable at any thickness. In real electrodes, however, the mobile charge is always distributed at a finite thickness next to the ferroelectric interfaces which is defined as the screening length λ. There is thus always a finite depolarizing field which can be expressed as $\mathbf{E_d} = -\frac{2\lambda}{\varepsilon_0 d}\mathbf{P}$, see Fig 2.4(a). The energy reduction from a uniform spontaneous out-of-plane displacement of charges is proportional to the film thickness d. By considering Eq. 2.2 and Eq. 2.4, we find that the increase of energy associated with the depolarizing field for has two terms proportional to $1/d$ and $\ln d/d_0$, where d_0 is the minimal thickness of the polarized medium (typically a single u. c.). Outside the film, the electric stray field does not directly depend on the film thickness. The energy balance thus shifts in favor of the electric field when reducing the film thickness. As a result, the net polarization needs to be suppressed below a certain thickness. Note that in the absence of charge screening, a suppression of the net polarization is predicted at any thickness of the ferroelectric layer [70].

The suppression of the net polarization can occur through the formation of domains [71], reduction of Curie temperature [72] or rotation of polarization to the in-plane direction, see Fig. 2.4(b). Multi-domain breakdown occurs as result of the balance between the energy required to form a domain wall and the electrostatic energy of out-of-plane domains. The bound charge at ferroelectric interfaces, which produces the electric field, can be screened by free electric charges, see details in Subsection 2.3.1.

2.2.2 Comparison with magnetism

For a magnetized medium, the magnetization **M**, magnetic induction **B** and magnetic field **H** are equivalent to the polarization **P**, electric field **E** and electric displacement field **D**, respectively. In analogy to the identification of the electric field inside the material as depolarizing field $\mathbf{E_d}$ and the electric field outside the medium as electric stray field $\mathbf{E_s}$, one can identify the magnetic field inside the medium as demagnetizing field $\mathbf{H_d}$ and the magnetic field outside the medium as magnetic stray field $\mathbf{H_s}$.

The demagnetizing field depends on the the geometry of the system and the orientation of magnetization in the same manner as the depolarizing field, i. e., the demagnetizing tensor corresponds to the depolarizing tensor. Therefore, for specific cases of a uniformly magnetized sphere $\mathbf{H_d}= -\frac{1}{3}\mathbf{M}$, for an infinitely thin film with out-of-plane magnetization $\mathbf{H_d} = -\mathbf{M}$ and for a film with in-plane magnetization $\mathbf{H_d} = 0$.

On the microscopic scale, however, the magnetic dipole cannot be separated into its monopoles, unlike the electric dipole. As a result, the screening of the magnetic field is in practice more difficult than the screening of the electric field. Screening of the magnetic field can be achieved by either a magnetized medium that has a high permeability or an equivalent magnetic field in the opposite direction produced by an external source.

2.3 Engineering the domain structure in epitaxial films

The ferroelectric response is governed by intrinsic contributions, such as spontaneous polarization and energy to form a domain wall, and extrinsic contributions, such as history and environment. Because of the high interface-to-volume ratio in ferroelectric thin films, extrinsic contributions at interfaces play a dominant role in setting the ferroelectric state. Controlling the interfaces of thin films thus creates a framework for tuning the ferroelectricity towards a targeted application [19, 20], see Section 2.4. The common denominator of all applications of ferroelectrics is the need for a robust and controlled domain structure.

Despite significant advances in the growth quality of ferroelectric-perovskite thin films [3], it is still challenging to master the impact of interfaces on the ferroelectric response. The reason behind this difficulty is the complex interplay of electrostatic and elastic conditions in the setting of the domain structure [73, 74]. I will discuss two basic approaches, charge screening and epitaxial strain, which have been used throughout this thesis to engineer the ferroelectric response in epitaxial thin films. A review on recent work on engineering the ferroic domains in thin films is published as [75]: N. Strkalj, E. Gradauskaite, J. Nordlander, and M. Trassin, "Design and Manipulation of Ferroic Domains in Complex Oxide Heterostructures", *Materials* **12**, 3108 (2019).

2.3.1 Charge screening

For a film with out-of-plane polarization, the bound charge at the ferroelectric interfaces generates an electric field. In the absence of screening of the bound charge, this electric field triggers the suppression of the net polarization, see an example in Fig. 2.5(a). To achieve a robust out-of-plane polarization, the depolarizing field needs to be minimized by screening the bound charge at both interfaces. We define the bottom interface as the interface towards the substrate and the top interface as the interface towards the surface.

The setting of polarization direction at a metal|ferroelectric interface is understood in terms of the position of the Fermi level of the metallic layer with respect to the valence and conduction bands in the ferroelectric film [76, 77]. Depending on the alignment of the energy bands, either electrons or holes are readily available in the metallic buffer for the screening of the bound charge at the interface of the ferroelectric film. The efficiency of the screening depends on the polarity of the charge that is to be screened. At a ferroelectric interface, the difference in screening efficiency leads to the preferential polarity of the bound charge and thus the preferential polarization direction.

To screen the bound charge at the bottom interface, one commonly introduces a metallic buffer electrode between the substrate and the ferroelectric film [29, 78]. In the case of an ideal metallic buffer, the mobile charge in the metal exactly compensates the bound charge. Complete screening of the bound charge would require the screening charge to be directly at the interface. In real metals, the screening charge is distributed over a finite distance from the interface which is defined as the screening length λ [79, 80], see Fig. 2.5(b). The screening length for metallic layers is in the range of 0.1 nm [81, 82]. At a metal|ferroelectric interface, the effect of the screening length is equivalent to the existence of a thin insulating layer between the ideal metal and the ferroelectric film [83]. The finite screening length creates a limit on the film thickness for stable out-of-plane polarization. This threshold value is referred to as critical thickness. The critical thickness to overcome the depolarizing field depends on the choice of the metal|ferroelectric pair.

Screening the bound charge at the bottom interface can alternatively be achieved by atomic-scale interface engineering [74]. The interface in a perovskite structure terminates in either an AO or BO_2 atomic plane which can be inherently charged as a result of a valency mismatch, for example as AO^+ and BO_2^- (Fig. 2.5(c)). Because the positively charged AO^+ plane can screen negative charges, this interface termination promotes a polarization pointing upwards, away from the interface. The negatively charged BO_2^- plane can screen positive charges and this interface termination thus promotes a polarization pointing downwards, towards the interface.

The screening at the top interface can be equivalently achieved by introducing a metallic top electrode or by a charge-screening environment such as oxygen gas [32, 33, 84, 85] or liquids [34–36] (Fig. 2.5(d)).

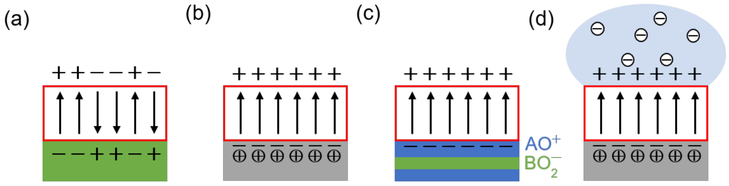

Figure 2.5: (a) Schematic of a multi-domain configuration in the absence of charge screening. (b) Charge screening at the bottom interface through a metallic buffer electrode. The region of the screening length λ is shaded blue. (c) Charge screening at the bottom interface through atomic-scale interface engineering. AO^+ and BO_2^- refer to the charged atomic planes of the perovskite structure. (d) Charge screening at the top interface through a charge-rich environment.

Materials

The use of oxide electrodes in ferroelectric-based heterostructures offers several advantages compared to the use of conventional electrodes, such as the possibility to grow epitaxial layers on top of the electrode, a lower leakage current and a longer fatigue endurance [86]. In this thesis, we used two typical oxide electrodes, $SrRuO_3$ (SRO) and $La_{0.7}Sr_{0.3}MnO_3$ (LSMO). As a bottom metallic buffer, SRO commonly terminates as SrO which promotes polarization pointing away from the metal|ferroelectric interface as a result of the above-discussed band alignment [87]. On the contrary, LSMO has charged interface planes and can thus be engineered to favor either polarization pointing away or towards the metal|ferroelectric interface which will be further discussed in Chapter 5.

2.3.2 Epitaxial strain

Epitaxy is a type of material deposition in which new crystalline layers are formed with a well-defined orientation with respect to the crystalline substrate [88]. The phase of the thin film is set by the atomic arrangement at the surface of the substrate. Epitaxial thin films sustain stress from the substrate because of the lattice mismatch between the crystal structure of the film and the substrate.

In epitaxially strained films, the in-plane lattice parameters of the thin film adapt to the lattice parameters of the substrate. The biaxial in-plane strain can then be calculated as

$$\eta = \frac{a_{\text{substrate}} - a_{\text{film}}}{a_{\text{substrate}}}, \tag{2.5}$$

where $a_{\text{substrate}}$ and a_{film} are the in-plane lattice constants of the substrate and the film, respectively. For this definition of strain, the sign of η is positive for tensile strain and negative for compressive strain, see Fig. 2.6. Strain evolves with temperature as a result of different thermal expansion coefficients of the substrate and the film [89]. Because the elastic energy of maintaining the strain scales with volume (here thickness) and because the strain is fixed at an interface, strain relaxation occurs above a certain thickness [90].

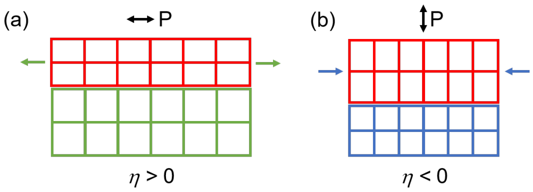

Figure 2.6: (a,b) Schematic of (a) tensile ($\eta > 0$) and (b) compressive ($\eta < 0$) epitaxial strain applied to the thin film (red) by the substrate (green and blue). Black arrows indicate the polarization (P) axes promoted in the ferroelectric thin film by the epitaxial strain.

Furthermore, since the polarization is coupled to the crystal structure, strain has a large impact on the polarization magnitude [91], domain structure [73, 92] and can even induce ferroelectricity in materials that are not normally ferroelectric [93–95]. In general, compressive strain promotes a uniaxial out-of-plane polarization with a domain structure governed by charge screening at interfaces. Tensile strain promotes multiaxial in-plane polarization with a domain structure governed by elastic stress and dipolar interactions within the ferroelectric layer. A ferroelectric film can also relax the strain imposed by the substrate by forming a multi-domain structure with domain walls at which polarization in the two neighboring domains is at 90° [96].

Materials

In this thesis, we used three typical oxide substrates: cubic (001)-oriented $SrTiO_3$ (STO), orthorhombic (110)-oriented $DyScO_3$ (DSO) and orthorhombic(110)-oriented $GdScO_3$ (GSO). The orthorhombic u. c. with lattice constants *a*, *b* and *c* can be viewed as a pseudocubic u. c. with approximately equal lattice constants along [110], [$1\bar{1}0$] and [001] of the orthorhombic u. c. In the (110) plane of the orthorhombic substrate, the lattice constants of the pseudocubic u. c. are similar to the lattice constants of typical perovskites, which allows for epitaxial growth.

An overview of the (pseudocubic) lattice constants of the substrates [97–99] and the resulting in-plane strain imposed on BTO and PTO is given in Table 2.2.

	a_{pc} (Å)	b_{pc} (Å)	$(a_{pc}+b_{pc})/2$ (Å)	η_{BTO}	η_{PTO}
STO	3.905	3.905	3.905	-2.3%	0%
DSO	3.943	3.945	3.944	-1.3%	1%
GSO	3.961	3.965	3.963	-0.8%	1.5%

Table 2.2: An overview of the (pseudocubic) lattice constants at room temperature and the in-plane strain imposed on BTO and PTO by (001)-oriented STO, (110)-oriented DSO and (110)-oriented GSO substrate.

2.4 Ferroelectric-based applications

All ferroelectric materials are also pyroelectric and piezoelectric. Many applications of ferroelectric materials do not directly exploit the polarization, but the pyroelectric effect, the piezoelectric effect, the high dielectric constant and nonlinear optical effects in ferroelectric materials. For example, the enhanced piezoelectric response in ferroelectrics has led to their use as transducing elements in distance sensors, actuators [100] and energy harvesting [101]. Furthermore, because of their non-centrosymmetric crystal structure, ferroelectrics are a source of nonlinear optical effects, such as second-harmonic generation, and also electro-optic effects, which are relevant for photonic applications [102–105].

More recently, thin ferroelectric films have been integrated with microelectronics [14, 19, 20]. In ferroelectric thin films, it is commonly the polarization itself which is the functional property of the material. In such applications, repeated reversal of the polarization direction is required using electric fields. During the application of the electric field, the domain configuration changes through nucleation and expansion of domains with a polarization projection pointing in the direction of the applied field. The possible polarization states, the switching path and the net polarization are determined by the domain configuration. Controlling the domain configuration is thus essential in applications of ferroelectric thin films.

For most such applications, a single-domain configuration with a maximized net polarization is desired to maximize the prospective ON/OFF ratio of a device sketched in Fig. 2.7. Because of the reversible permanent electric polarization, ferroelectrics can be used in device concepts such as ferroelectric memories [12, 13, 106–114] and field-effect transistors [115, 116]. One can further use the polarization-induced bound charge at the interfaces of the ferroelectric thin film for catalysis [117–121] or electrical energy storage in capacitors [122, 123].

However, there are also some applications which benefit from a multi-domain configuration. Multi-domain configurations are attractive for applications requiring an existence of several intermediate stable states, such as neuromorphic computing [124, 125]. Furthermore, there is an emerging interest in so-called complex arrays of dipole moments [37–45, 126–132] as a promising platform for voltage amplification via negative capacitance [122, 123, 133–136].

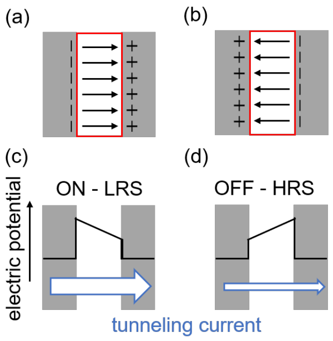
(a)
(b)
(c)
(d)
ON - LRS
OFF - HRS
electric potential
tunneling current

Figure 2.7: (a-d) Schematic of an example of a ferroelectric-based memory element based on the principle of quantum tunnelling. (a,b) Polarization direction and the resulting bound charge in a ferroelectric-based capacitor. (c,d) Electric potential across the capacitor (black lines) and the tunnelling current (blue arrow) (c) for the ON — low-resistance state (LRS) and (d) for the OFF — high-resistance state (HRS).

Experimental methods

3

The development in the growth of epitaxial thin films now allows producing high-quality ferroelectric thin films with precise control of the layer thickness down to the u. c. level [137]. Oxide thin films presented in this thesis were all grown by pulsed laser deposition (PLD). During the growth, thickness and quality of the films were monitored using reflection high-energy electron diffraction (RHEED). Additionally, a unique in-situ optical second harmonic generation (ISHG) technique was developed in our lab as a part of this thesis to monitor the emergence and evolution of ferroelectric properties during the growth. After deposition, I characterized structural and ferroelectric properties of our films using optical SHG, scanning probe microscopy (SPM) and x-ray diffraction (XRD). Further post-deposition characterization was performed by our collaborators, namely scanning transmission electron microscopy (STEM) by Marta Rossell, Marco Campanini, and Alexander Vogel at the Electron Microscopy Center at Empa, Switzerland, terahertz time-domain spectroscopy (THz-TDS) by Shovon Pal at ETH Zurich, and x-ray photoelectron spectroscopy (XPS) by Antonella Rossi at ETH Zurich. I will present a brief background of each of these experimental methods with the main focus on optical SHG.

3.1 Pulsed laser deposition

Pulsed laser deposition is a physical vapor deposition technique in which a high-power pulsed laser beam is focused inside a vacuum chamber to ablate the target material from a crystal pellet and create a plasma of the material, which propagates to a heated crystalline substrate [138, 139], see Fig. 3.1(a). The targets are bulk crystals or ceramic pellets. The compositional excess in the target may compensate for the volatility of an element in the desired material such as Pb or Bi.

PLD is a versatile film-growth technique because of its many control parameters such as choice and the pressure of the background gas, the laser repetition rate, laser fluence, and temperature of the substrate.

A prerequisite for high-quality deposition is a controlled atmosphere during the deposition. To achieve this, a high vacuum at a pressure of $p < 10^{-6}$ mbar is

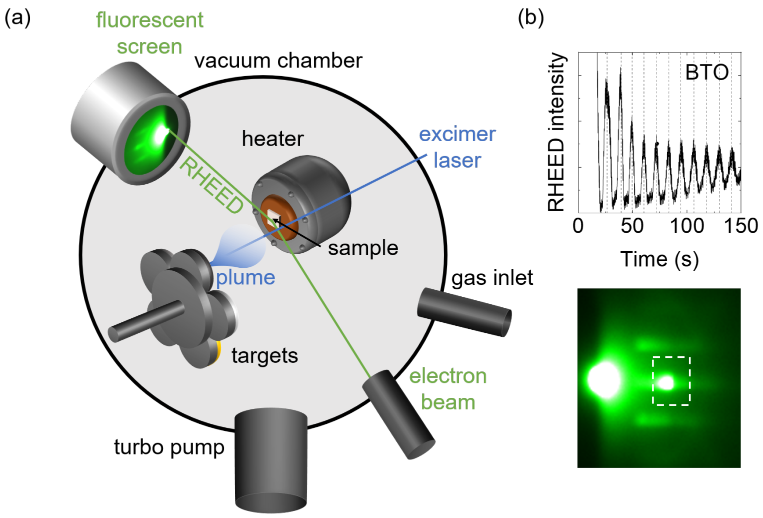

Figure 3.1: (a) Schematic of a pulsed-laser-deposition chamber. (b) Time dependence of intensity of a diffraction spot in the RHEED pattern during the growth of a BTO film on SRO-buffered (110)-oriented GSO substrate. (top) The electron diffraction pattern during the growth. The dashed white outline denotes the specular reflection at which the intensity was measured. (bottom)

maintained in the growth chamber before the deposition to prevent the incorporation of residual gas into the growing film. During the deposition of oxide thin films, an oxygen gas with a pressure of typically 10^{-1} mbar is introduced to promote the oxidation of the ablated species and to reduce the formation of oxygen vacancies.

In this thesis, we use laser pulses from a KrF excimer laser with a wavelength $\lambda = 248$ nm and a pulse duration of 20 ns to ablate the material from the target. The PLD laser has a typical repetition rate in the range of 1–10 Hz and the laser fluence on the target is in the order of 1 Jcm^{-2}. The laser frequency and fluence are the most important parameters determining the growth rate. Depending on the material, a slower growth rate may be preferred to minimize the formation of defects, or a faster growth rate may be necessary to minimize the loss of volatile elements.

To ensure that the atoms and ions of the deposited material have sufficient mobility to arrange themselves in a crystalline state, the substrate is heated to an elevated temperature in the range of 500–800° C. After the deposition, the cooling rate is set to 1–10 Kmin^{-1}.

Reflection high-energy electron diffraction

For this thesis, RHEED was used to monitor the thickness and quality of the films during the growth. Electron diffraction is performed in grazing incidence to interact mainly with the few top layers of the growing film [140, 141]. The diffraction pattern generally provides information about the crystal structure of the surface, the crystal orientation, the strain and the surface roughness. However, acquisition and analysis of the RHEED pattern during PLD is limited by the oxygen gas pressure causing diffuse scattering of electrons. Therefore RHEED is used for this thesis mainly to follow the evolution of the surface roughness.

A change in surface roughness induces a change in intensity of the specular reflection, which can be used for monitoring the growth mode. In the case of a layer-by-layer growth mode, i. e., when a complete layer forms before the growth of subsequent layers, the intensity of the specular reflection oscillates in time with a period typically corresponding to the deposition of one u. c., see Fig. 3.1(b). Full coverage of a surface corresponds to a maximum in intensity, while half-coverage corresponds to a minimum in intensity. If the surface roughness increases or the two-dimensional growth mode changes, the amplitude of oscillations decreases or eventually vanishes [142].

3.2 Optical second harmonic generation

In this section, we introduce the basics of optical SHG as a probe of ferroelectric properties in thin films. For a review of recent work about the use of SHG as a probe of ferroic thin films, see [18]: J. Nordlander, G. De Luca, N. Strkalj, M. Fiebig, M. Trassin, "Probing Ferroic States in Oxide Thin Films Using Optical Second Harmonic Generation", *Applied Sciences* **8**, 570 (2018).

The light-matter interaction in crystals exhibiting ferroelectric order can be approximated by the leading-order electric-dipole contribution because any further contributions such as the magnetic-dipole and electric-quadrupole contributions are commonly negligible [143].

In the leading-order electric-dipole approximation, the light-matter interaction is described by

$$P(t) = \epsilon_0[\chi^{(1)}E(t) + \chi^{(2)}E^2(t) + ...], \tag{3.1}$$

where $P(t)$ is the induced polarization in the material, ϵ_0 is the vacuum permittivity, $\chi^{(n)}$ is the n-th order electric susceptibility of the material and $E(t)$ is the time-varying electric-field of the light [144, 145].

The induced polarization $P(t)$ acts as a source of electromagnetic radiation. For low electric-field amplitudes of the incoming light field, the outgoing light is dominated by linear processes. In addition to the linear processes, for intense light fields such as those provided by a laser light, nonlinear processes start to come into play. The most important experimental advantage of nonlinear processes in comparison to linear processes is the avoidance of background radiation; although the amplitude of the higher harmonic light might be low, the different frequency of the nonlinear light allows for convenient separation from the incident light by frequency filters [18, 146, 147].

SHG is the simplest nonlinear process and can be understood as frequency doubling of a light wave in a material, i. e., conversion of two incident photons with frequency ω into a single outgoing photon with frequency 2ω, see Fig. 3.2(a). We

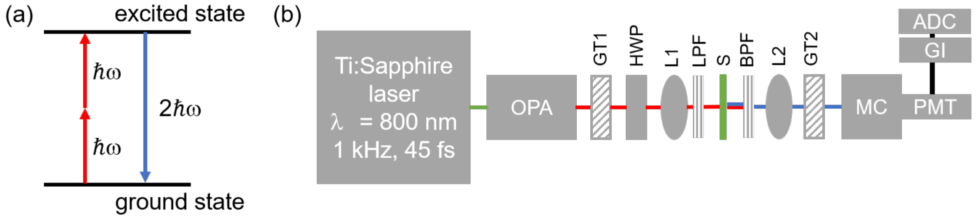

Figure 3.2: (a) Schematic of the quantum mechanical description of optical SHG. (b) Schematic of the SHG experimental setup used for this thesis.

can then describe the induced second-order polarization as

$$P_i^{(2)}(2\omega) = \epsilon_0 \chi_{ijk}^{(2)} E_j(\omega) E_k(\omega). \tag{3.2}$$

Here, the $\chi^{(2)}$ tensor is linked to the symmetry of the crystal by the Neumann principle [148]: The symmetry elements of any physical property of a crystal must include the symmetry elements of the point group of the crystal. In the leading-order electric-dipole approximation, SHG is non-zero in the absence of inversion symmetry, such as in the case of crystals exhibiting ferroelectric order. SHG is thus a powerful tool to characterize domain structure and domain configuration in ferroelectric thin films [30, 149–158].

3.2.1 Experimental setup

The experimental setup used in this thesis is depicted in Fig. 3.2(b). Light pulses from a Ti:Sapphire laser at a wavelength of 800 nm with a pulse duration of 45 fs and a repetition rate of 1 kHz are used to pump an optical parametric amplifier (OPA), which enables tuning the wavelength of the incident beam. We avoid probing resonant electronic excitations by choosing a wavelength corresponding to a photon energy away from any inherent absorption of the studied ferroelectric materials. The incident beam was thus set to 1200 nm (1.03 eV). The incident light polarization is set with a Glan-Taylor prism (GT1) and a half-wave plate (HWP), which is mounted on a motorized rotation stage. The light is then focused onto the sample (S) with a lens (L1). A long-pass filter (LPF) is used before the sample to filter any frequency-doubled induced by optical components. After the sample, a band-pass filter (BPF) is used to block the incident beam at the fundamental wavelength and transmit only the SHG light induced by the sample. The light is collected by a lens (L2). The polarization of the SHG light is analyzed with a GT prism (GT2), which is mounted on a motorized stage. The SHG wavelength is selected in the monochromator (MC). The optical pulses are converted into an electrical current using a photomultiplier tube (PMT). The signal is acquired by a gated integrator (GI) and converted into a digital format by an analog-digital converter (ADC).

Polarimetry measurement

The laboratory coordinate system is chosen such that x is the axis orthogonal to the optical table and light propagates along z. Laser-light pulses propagate into the sample with a linear polarization oriented along the angle α with respect to x of the laboratory coordinate system. The generated nonlinear signal at twice the frequency is analyzed in its polarization state using an analyzer oriented at an angle β with respect to x of the laboratory coordinate system. The independent rotation of polarizer and analyzer at angles α and β, respectively, is used in polarimetry measurements to access the frequency-doubled light generated by different components of the $\chi^{(2)}$ tensor. One can, thus, map the $\chi^{(2)}$ tensor and relate it to a particular crystal structure.

Light propagation direction relative to the sample normal

The electromagnetic fields of a light wave oscillate perpendicular to the direction of wave propagation. We distinguish the measurement geometries by the angle between the light propagation direction and the sample normal. In SHG experiments, when light propagates along the sample normal (normal incidence), we access only the inversion-symmetry breaking in the plane perpendicular to the surface normal of the sample (in-plane). When light propagates at a finite angle to the sample normal (tilted incidence), we are sensitive to inversion-symmetry breaking which occurs both in the planes perpendicular and parallel to the surface normal of the sample (in-plane and out-of-plane). The closer the angle between the light propagation and the sample normal is to 90° (grazing incidence), the more sensitive we are to the inversion-symmetry breaking which occurs parallel to the surface normal of the sample (out-of-plane).

3.2.2 Optical second harmonic generation in thin films

When measuring SHG in thin films, additional aspects need to be taken into consideration in comparison to SHG in bulk crystals.

Thickness

In the case of ferroelectric films thinner than 10 nm, the amplitude of the SHG signal is proportional to the thickness of the films [18, 147]. Therefore the SHG intensity is proportional to the square of the thickness. For films thicker than 10 nm, multiple reflections at interfaces ($\gtrsim$100 nm), phase mismatch of the incident and the generated light ($\gtrsim$1 µm) and optical absorption ($\gtrsim$10 µm) need to be considered. Note that optical absorption and reflectance can be considerable even for films as thin as 10 nm for metallic layers. Substrates may further absorb the fundamental and SHG light, or produce SHG themselves. It is, therefore, necessary to always measure the linear and nonlinear optical properties of the substrates independently. Throughout this thesis, films are measured in the reflection geometry to minimize the influence of the substrates.

Interfaces and surfaces

In thin films, several interfaces are inevitably present, such as the substrate|film and the film|air interface (surface). Because the inversion symmetry is broken at interfaces, they produce an electric-dipole type SHG response [159, 160]. SHG of interfaces can furthermore have a comparable amplitude to the SHG of the film which can hamper the analysis of the SHG signal. It is therefore essential to carefully consider the interference of these responses.

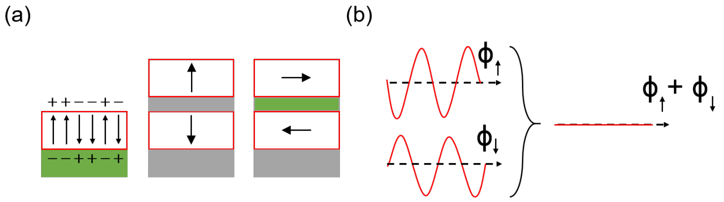

Figure 3.3: (a) Schematics of thin-film heterostructures with zero net polarization: multi-domain configuration (left), two layers with opposite out-of-plane polarization (middle) and two layers with opposite in-plane polarization. Black arrows represent the direction of polarization. Dielectric layers are denoted in green and metallic layers in grey. (b) Destructive interference of SHG contributions from domains with oppositely oriented polarization ($\phi_\uparrow$, $\phi_\downarrow$) because of the phase difference of $180°$.

Domains

For ferroelectric films with thickness below 1 µm, the domain size is usually below the diffraction-limited SHG resolution of the optical detection scheme ($\lambda_{\mathrm{SHG}}/2$), see Subsection 2.1.2. As a result, the SHG response originates from interference of SHG waves generated in all probed domains and not from individual domains. In the case of probing domains with antiparallel orientation of polarization of equal volume proportion, the SHG waves of domains with the opposite polarization directions destructively interfere which can lead to a cancellation of SHG response, see Fig. 3.3.

The SHG response of ferroelectric films with a multi-domain configuration might be different from the SHG response of its individual domains In the case of a heterostructure with several SHG-active layers, the SHG responses of individual layers interferes.

3.3 In-situ optical second harmonic generation

The methodical backbone of the investigations presented in this thesis is ISHG. Optical SHG is a non-invasive technique that can function at a large working distance. Therefore, it is ideal for probing properties of a material during its growth. Indeed, ISHG analysis of the surface symmetry has been previously used as a diagnostic tool for adsorption on semiconductors [161] and the determination of the critical thickness and interim magnetic phases in ferromagnetic thin films [162]. Here we employ ISHG for the first time to study the emergence and evolution of ferroelectricity during the growth.

The conceptual precursor measurements for the ISHG implementation were conducted by Gabriele De Luca and myself [17]. These preliminary results on using ISHG for probing ferroelectricity were published as [17]: G. De Luca, N. Strkalj, S. Manz, C. Bouillet, M. Fiebig, and M. Trassin. "Nanoscale design of polarization in ultrathin ferroelectric heterostructure", *Nat. Commun.* **8**, 1419 (2017).

As a part of our theses, Johanna Nordlander and myself developed ISHG into an actual tool for monitoring ferroelectricity during the growth within the framework of the ERC Advanced Grant "INSEETO". We jointly performed the methodological changes to the ISHG setup, which were required to bridge the gap between the proof-of-principle measurements and the advanced use of ISHG. Our work paved the way for the commercialization of the ISHG setup as a part of the ERC Proof of Concept Grant "POLARIS", which will lead to a device prototype that will eventually open up ISHG to the use of non-experts in the form of a marketable device.

I will now focus on the crucial insights provided by ISHG that are unique to this thesis. Because the ferroelectric response of the systems I studied is already determined during the growth, ISHG is essential for understanding and engineering ferroelectricity in these systems.

Tracking ferroelectricity during the growth with ISHG is of fundamental interest because it allows unprecedented access to transient phenomena occurring during the integration of ferroelectric layers into heterostructures. For example, unexpected polarization dynamics is observed during the growth of ferroelectric-based heterostructures as a result of interface contributions to the polarization response. ISHG thus not only complements the extensive post-deposition characterization but also reveals polarization states that would otherwise be entirely overlooked after the completed deposition. By observing the polarization states during the growth, we bring understanding to the impact of interface-related electrostatic effects on ferroelectric response after the growth.

This understanding of the final ferroelectric response, as provided by ISHG, is indispensable for tuning the functionality of ferroelectric layers. Monitoring polarization at every step of the heterostructure growth creates the opportunity to engineer the polarization by changing the growth process at any point. The change in the growth process of ferroelectric-based heterostructures has a lasting impact on the ferroelectric response. This new level of control is here used to

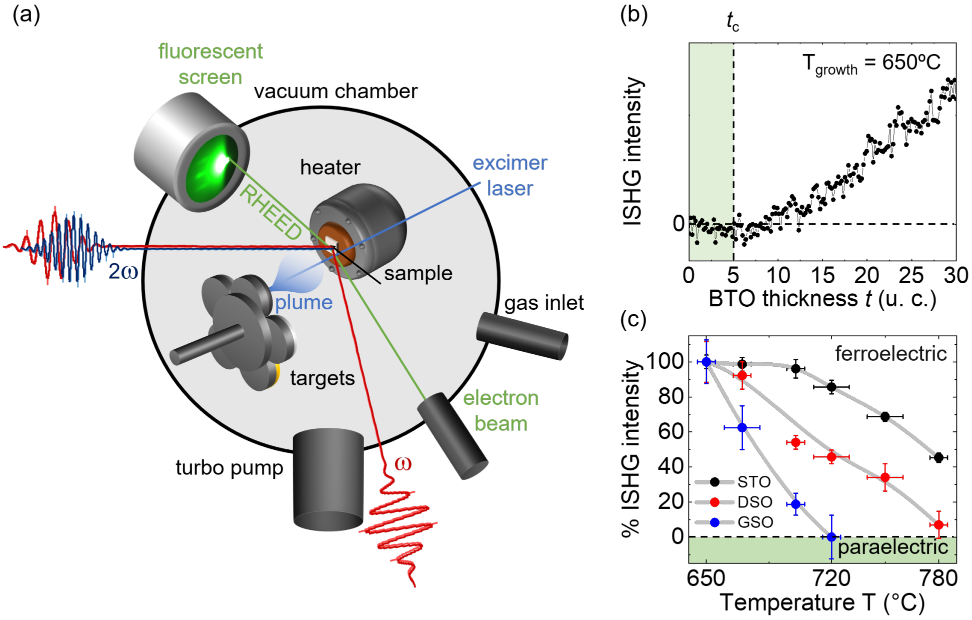
(a)
fluorescent screen
vacuum chamber
heater
excimer laser
RHEED
2ω
sample
plume
gas inlet
targets
electron beam
turbo pump
ω
(b)
t_c
T_{growth} = 650°C
ISHG intensity
0
0
5
10
15
20
25
30
BTO thickness t (u. c.)
(c)
ferroelectric
% ISHG intensity
100
80
60
40
20
0
STO
DSO
GSO
paraelectric
650
720
780
Temperature T (°C)

Figure 3.4: (a) Schematic of the ISHG experimental setup. (b) ISHG signal tracking the BTO thin-film polarization during the growth on an SRO-buffered (001)-oriented STO substrate. The polarization emerges at a critical thickness t_c. (c) SHG intensity as a function of temperature for BTO thin films on different substrates, normalized to the value at the end of the growth process. The Curie temperature of bulk BTO is 120°C [67], but increases above growth temperature with epitaxial strain.

stabilize a robust single-domain configuration in the ultrathin regime required in typical ferroelectric-based applications. Such control is of immense importance in the applications of ferroelectric thin films because the as-grown domain structure determines the possible polarization states and the switching path between them.

3.3.1 Experimental setup

Our growth chamber restricts the measurement mode for ISHG to a configuration at which light gets reflected under 45° with respect to the sample surface normal (90° as full reflection angle). The incident light with a pulse energy of typically 30 µJ is focused onto the sample with a spot size of 250 µm in diameter. The frequency-doubled light is collected with a lens and led to the detection system by a pair of motorized mirrors. ISHG intensity is typically integrated for 1 s at fixed settings of the polarizer and the analyzer. Note that in the current measurement configuration, ISHG is sensitive to the SHG response of the film's interfaces and is thus limited in probing multilayers with low SHG yield.

3.3.2 Critical thickness of ferroelectric thin films

Using ISHG, the critical thickness of a ferroelectric film can be measured in dependence of the metallic buffer electrode and growth parameters, see Fig. 3.4(b).

Gabriele De Luca and myself developed a model to account for the thickness-dependent ISHG evolution in relation to the polarization of the ferroelectric layer. Below the critical thickness, a thickness-independent surface signal with an SHG amplitude of $P_{\mathrm{S}}(2\omega)$ is observed. Past the critical thickness the ISHG intensity can be expressed as

$$I(2\omega, t) \propto |P_{\mathrm{S}}(2\omega) + (t - t_{\mathrm{c}}) P_{\mathrm{FE}}(2\omega, t) e^{i\delta}|^2 \tag{3.3}$$

with t being the film thickness, t_c the critical thickness for ferroelectricity, $P_{\mathrm{FE}}(2\omega, t)$ the SHG amplitude of the thickness-dependent ferroelectric response, and δ is a phase between the surface-induced and ferroelectric-induced SHG contributions. The thickness-dependence of the electric polarization $P_{\mathrm{FE}}(2\omega)$ can thus be calculated from the ISHG-intensity evolution.

3.3.3 Curie temperature of ferroelectric thin films

Although the Curie temperatures of bulk ferroelectric materials are commonly below the growth temperatures, epitaxial strain can substantially enhance the Curie temperatures, see Fig. 3.4(c). In fact, the Curie temperature can be raised above the growth temperature for most ferroelectrics with a perovskite structure [163] such as BTO [17, 30, 164–167], PTO [84, 87, 155, 156, 168], Pb(Zr,Ti)O_3 (PZT) [156] and BiFeO_3 (BFO) [17].

As a result of the enhancement of the Curie temperature, a spontaneous-polarization-related ISHG signal can be measured during the growth.

3.4 Scanning probe microscopy

Scanning probe microscopy (SPM) is a technique that uses a physical probe to study surfaces. An image of the surface is obtained by scanning a probe in close proximity to the sample and measuring the interaction between the probe and the sample. The probe is typically a cantilever with a sharp tip. The forces between the tip and the sample are monitored by tracking the reflex of a laser beam from the back of the cantilever on a photodiode.

For this thesis, we use two types of scanning probe microscopy: atomic force microscopy (AFM) and piezoresponse force microscopy (PFM). A schematic of the SPM setup and some typical AFM and PFM images are shown in Fig. 3.5.

In AFM, van-der-Waals forces or contact forces between the tip and the sample are used to measure the sample topography or mechanical properties. The vertical resolution of the AFM is about 0.1 nm. The lateral resolution of the AFM is determined by the radius of the tip apex and is usually in the order of

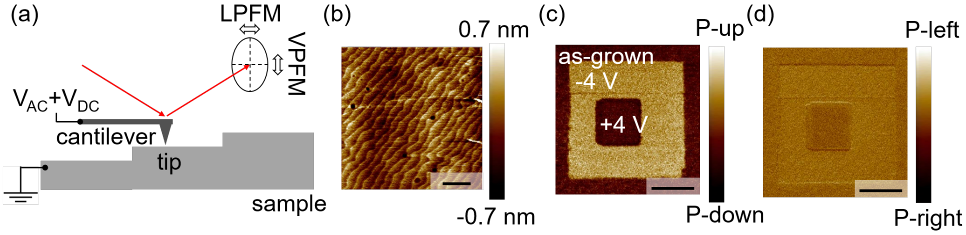

Figure 3.5: (a) Schematic of the SPM setup. (b) AFM topography image of atomic step terraces on the surface of a PTO film on LSMO-buffered (001)-oriented STO substrate. (c) VPFM and (d) LPFM from an area of the film where the as-grown down-polarized (dark) state has been switched to an up-polarized (bright) state in the outer square and back to a down-polarized state in the inner square by a DC voltage applied to the PFM tip in preceding poling scans. Scale bars are 1 µm.

30 nm. Polarization reversal can be induced by mechanical pressure applied with a scanning-probe tip via the flexoelectric effect [169–172].

In PFM, a conductive tip is brought in contact with the sample and an oscillating voltage (AC) voltage is applied to the tip, while the sample is grounded. For a piezoelectric sample, the applied voltage induces elastic deformations. The oscillations induced by the AC voltage can be easily separated from the AFM signal in the frequency domain. Since all ferroelectric materials are piezoelectric, it is possible to use PFM to visualize the domain configuration in a ferroelectric thin film. Signal calibration and careful separation of vertical (VPFM, deflection and buckling) and lateral (LPFM, torsion) cantilever movements allows mapping of the surface polarization direction [173, 174]. Deflection in the VPFM corresponds to an out-of-plane polarization. Buckling in the VPFM and torsion in the LPFM correspond to an in-plane polarization.

Additionally, a constant voltage (DC) voltage can be applied at the tip to locally manipulates the polarization with an electric field. For a stationary tip, the net electric field is along the sample normal. An electric field is also applied radially to the tip apex in the sample plane. As a result of the tip movement, this in-plane electric field can result in a net trailing field along the slow scanning axis, see details in [175–180] and in Chapter 7.

3.5 X-ray diffraction

X-ray diffraction (XRD) is a standard technique to characterize crystal structures. An x-ray beam enters the sample at an angle ω. Constructive interference of the diffracted x-rays occurs under Bragg condition

$$2d_{hkl}\sin\theta = n\lambda, \tag{3.4}$$

where d_{hkl} is the distance between the crystallographic planes of the crystal with Miller indices hkl, $\theta = \omega$ is the diffraction angle, n is an integer number and λ is the x-ray wavelength [181]. We use a Cu K-α x-ray source with a wavelength of 1.54Å. Distances in reciprocal space δQ can be related to distances in real space d as $\delta Q = 2\pi/d$. The accessible reciprocal space is shown in Fig. 3.6(a).

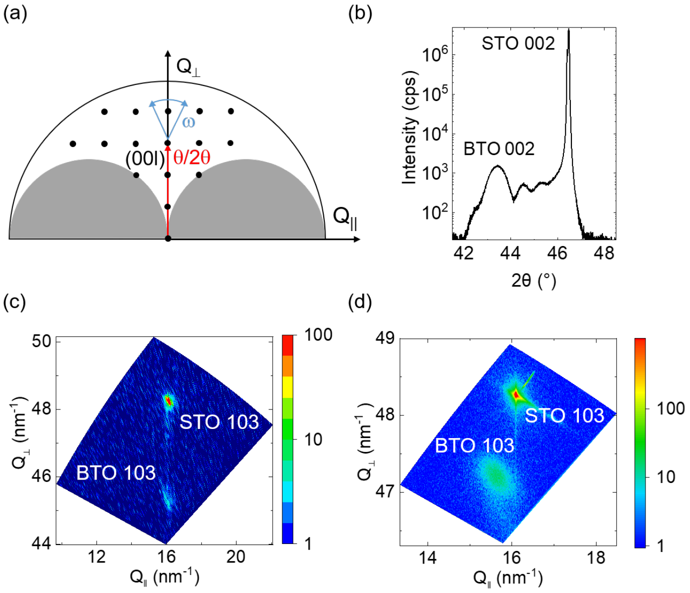

Figure 3.6: (a) Reciprocal space accessible by the diffractometer. The outer semi-circle (black line) is set by the x-ray wavelength, and the inner semi-circles (grey) are set by the measurement geometry. A scan along $Q_{||} = 0$ is termed a $\theta/2\theta$ scan. A scan of the sample tilt is termed ω scan. A combination of these two scans generates a RSM. (b) X-ray intensity in a $\theta/2\theta$ scan around the 002 reflection of BTO. (c,d) RSM mapping of 103 reflections of BTO and STO. (c) The 103 Bragg peaks of a BTO film of 30 u. c. thickness and the STO substrate are measured at the same $Q_{||} = 0$ value (coherently strained). (d) The 103 Bragg peaks of a BTO film of 90 u. c. thickness and the STO substrate are measured at different $Q_{||} = 0$ values (strain relaxation).

Note that XRD can also be combined with the thin-film synthesis, but it requires high x-ray flux of synchrotron facilities and halting the growth process [32, 33, 84, 85, 163–165, 168],

The thickness of the thin films can be quantified using x-ray reflectivity. Under grazing incidence, the x-rays are reflected from all interfaces in the thin film heterostructure (air/film, film/substrate) and interfere with each other resulting in Kiessig fringes in the intensity of the reflected beam as a function of the angle of incidence. The thickness of the layer is related to the periodicity of these fringes. Out-of-plane lattice constants can be measured in the $\theta/2\theta$ scan, see Fig. 3.6(b). The crystallinity of the sample is accessed in the ω scan.

Plenty of additional information can be obtained from the reciprocal-space maps (RSMs). RSMs are generated using a combination of two scans, often the $\theta/2\theta$ and the ω scan. First, out-of-plane and in-plane lattice constants can be measured which can be related to the polarization [23, 182, 183]. This information can be further used to determine the strain state of the film by comparing the in-plane lattice constant of the substrate and the film, see Fig. 3.6(c,d). Second, the presence of different crystal phases and ferroelectric domain variants [184–188] can be detected. Finally, RSMs can resolve nanoscale ordering of domain walls which results in in-plane diffuse scattering around Bragg peaks [189].

3.6 Scanning transmission electron microscopy

In STEM, a tightly focused electron beam is scanned across a thin specimen, and the transmitted and scattered electrons from a localized volume of the material are detected as a function of the spatial position of the electron beam. The thin specimen required for STEM is prepared to access the desired crystallographic orientation.

Transmitted electrons at low angles are collected in the bright field (BF) detector, coherently Bragg scattered electrons at intermediate angles in the annular dark-field (ADF) detector and incoherently scattered electrons at high angles in the high-angle annular dark-field (HAADF) detector, see Fig. 3.7(a). Since the incoherent scattering detected in the HAADF detector electrons is almost exclusively a result of Rutherford scattering from the nucleus of atoms, the images obtained from the HAADF detector are highly sensitive to the atomic number Z. Elements with a higher atomic number produce more scattering, and thus the intensity of the atomic species in the HAADF image is approximately proportional to the square of the atomic number Z^2.

The spatial resolution of STEM images depends on the size of the electron beam, which is strongly limited by the spherical aberration of the objective lens. With aberration corrections, it is possible to routinely produce images with sub-Å-resolution [190] and to detect ionic displacements as small as 5 pm, which allows for mapping dipole moments within a u. c., as shown in Fig. 3.7(c,d). A STEM setup can be further equipped with analytical techniques such as energy dispersive x-ray (EDX) spectroscopy to enable elemental mapping in samples, see Fig. 3.7(b).

STEM detection of local dipole displacements has been the complementary technique to SHG detection of net polarization throughout this thesis. EDX elemental mapping has been used to determine the termination planes and stoichiometry changes at film interfaces in Chapter 4 and Chapter 5, respectively.

3.7 Terahertz time-domain spectroscopy

THz-TDS is a spectroscopic technique in which the material properties are probed with short pulses of THz radiation. The change of both the amplitude and the phase of the THz pulse after the sample is measured. Here we employ THZ-TDS to non-invasively evaluate the optical conductivity of thin metallic layers [191–193].

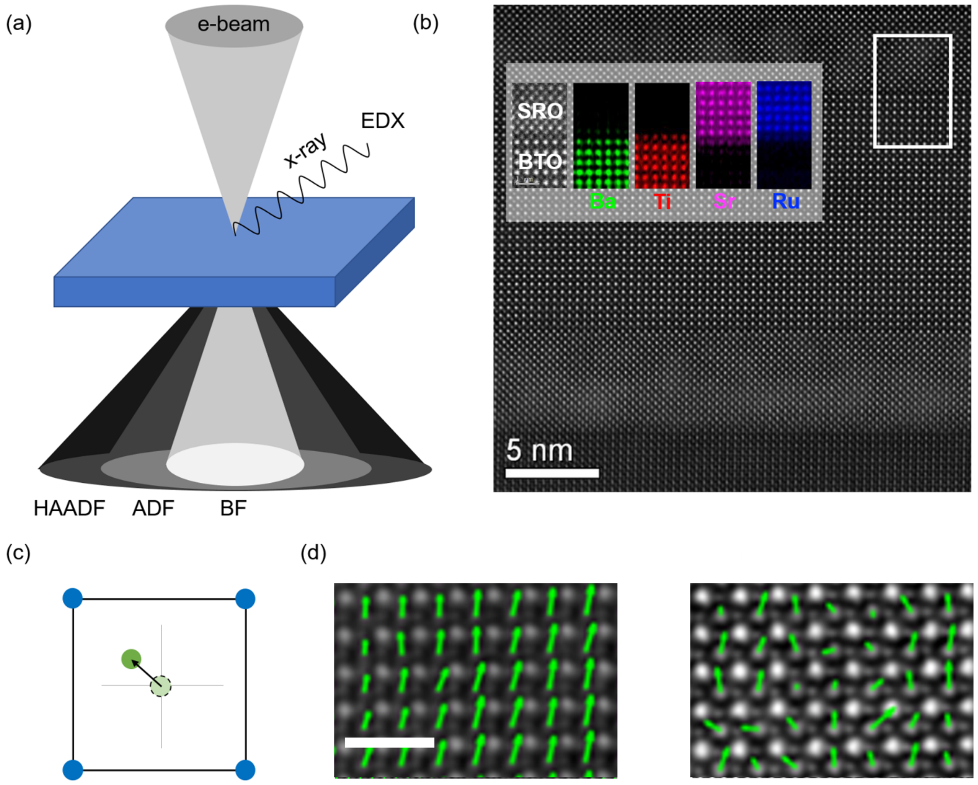

Figure 3.7: (a) Schematic of STEM. An electron beam (e-beam) is scanned across a thin specimen. The transmitted and scattered electrons are detected by the BF, ADF or HAADF detectors. The e-beam ionizes the atoms in the specimen, which upon returning to the ground state emit x-rays that are detected in the EDX detector. (b) A high-magnification HAADF image of a SRO|BTO|SRO capacitor on a (001)-oriented STO substrate. The inset shows elemental mapping obtained by EDX at the BTO|SRO interface within the white outline. (c) Schematic of the ionic displacements used for mapping the dipole moments in the HAADF-STEM images. (d) A single-domain (left) and a multi-domain (right) configuration in the SRO|BTO|SRO capacitor on a (001)-oriented STO substrate. Scale bar is 1 nm.

We measure the time traces of the THz pulses from a reference (mirror) $E_{\text{reference}}(t)$ and the sample $E_{\text{sample}}(t)$, see Fig. 3.8(a). These signals are then Fourier-transformed to obtain the complex spectra in the frequency domain $\tilde{E}_{\text{reference}}(\omega)$ and $\tilde{E}_{\text{sample}}(\omega)$. The amplitude of the complex spectra is referred to as the spectral amplitude, see Fig. 3.8(b). The reflectance is obtained by normalization as $\tilde{R}(\omega) = \tilde{E}_{\text{sample}}(\omega)/\tilde{E}_{\text{reference}}(\omega)$.

The complex conductivity $\tilde{\sigma}(\omega)$ can be calculated from the reflectance, which in the limit of thin film approximation gives

$$\tilde{\sigma}(\omega) = \frac{1}{Z_0 d}\left(\frac{1 + n_{\text{substrate}}(\omega)}{1 - \tilde{R}(\omega)} - 1 - n_{\text{substrate}}(\omega)\right), \tag{3.5}$$

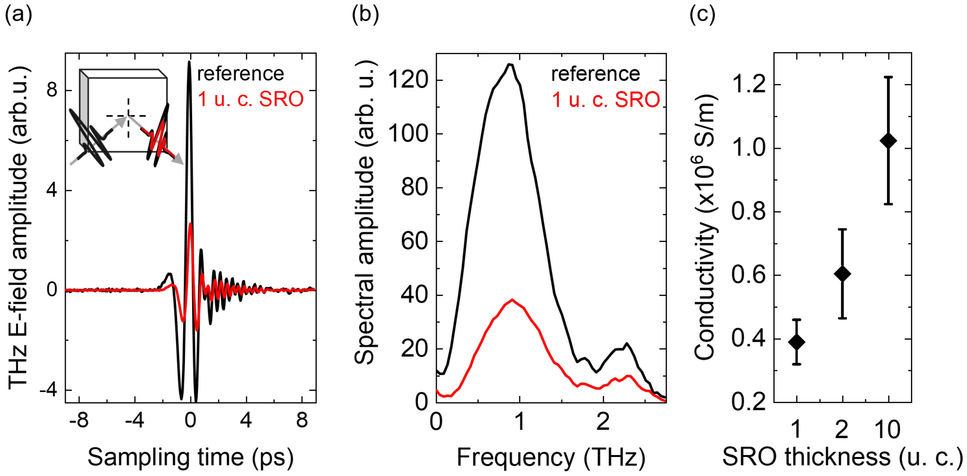

Figure 3.8: (a) The time transients from the reference and the 1-u.-c.-thick SRO layer on a SRO|BTO heterostructure on an (001)-oriented STO substrate. Inset shows the 45°-reflection geometry. (b) The spectral amplitude of the electric fields obtained by the Fourier transforms of the pulses in (a). (c) The weighted average of the real part of the complex optical conductivity of the SRO layer with different thickness.

where Z_0 is the impedance of vacuum, d is the thickness of the metallic layer and $n_{\mathrm{substrate}}(\omega)$ is the refractive index of the substrate (Fig. 3.8(c)). The real part of the complex optical conductivity is related to the DC conductivity in the low-frequency limit ($\omega \to 0$) [194]. The real part of the optical conductivity is responsible for the charge screening and depolarizing effects that are elaborated on in Chapter 2.

3.8 X-ray photoelectron spectroscopy

XPS is a spectroscopic technique based on the photoelectric effect that is used to identify elements within 5 nm of the sample surface [195]. The elements are identified by the binding energy of electrons $\mathrm{E_b}$. X-rays with frequency ν impinge on the sample, and the kinetic energy of the emitted electrons $\mathrm{E_k}$ is measured, see Fig. 3.9(a,b). The binding energy is then derived from the energy conservation of the XPS measurements according to

$$\mathrm{h}\nu = \mathrm{E_k} + \mathrm{E_b}, \tag{3.6}$$

where h is the Planck constant. Moreover, within the probing depth, it is possible to estimate the profile of the composition by performing angle-resolved XPS measurements . For higher emission angles θ (Fig. 3.9(c)), only the electrons from the surface are emitted, while for the lower emission angles, also the electrons from layers below the surface can be detected. XPS is used for determining the surface defects in thin films [36]. We employ XPS to evaluate the growth-induced non-stoichiometry discussed in Chapter 5.

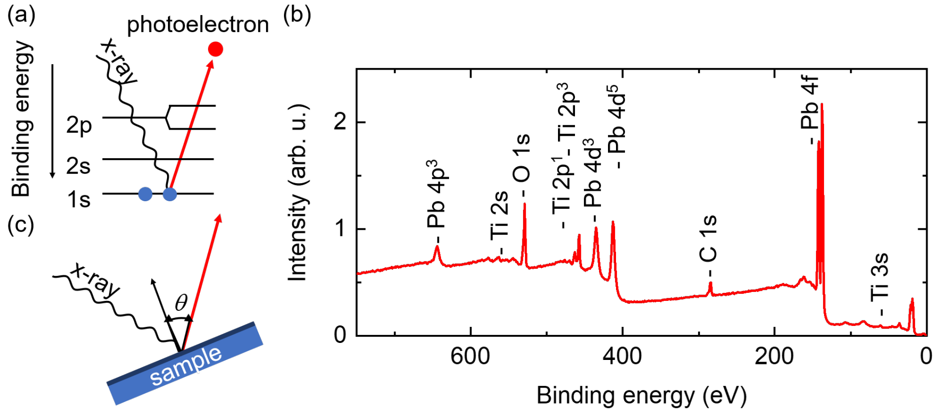

Figure 3.9: (a) Sketch of the quantum mechanical process underlying XPS. (b) A typical XPS spectrum of a PTO thin film on LSMO-buffered (001)-oriented STO substrate. Peaks positions are labelled with the element from which the photoelectron originated and the electron configuration. (c) Schematic of angle-resolved XPS with θ denoting the emission angle.

Transient electrostatics in ferroelectric-based capacitors

4

In this chapter, we discuss the transient electrostatics during the design of a ferroelectric heterostructure on the example of a metal|ferroelectric|metal SRO|BTO|SRO capacitor. In this model system, we resolve a long-standing puzzle of net polarization suppression in the ferroelectric-based capacitor. In a ferroelectric layer beyond its critical thickness, the polarization is commonly stable without the presence of a top electrode but entirely suppressed once the top electrode is introduced. This suppression of polarization in a capacitor is puzzling because the presence of electrodes should provide charge screening at ferroelectric interfaces and thus stabilize, rather than destabilize polarization. Using ISHG, we monitor the evolution of ferroelectricity during the growth of the top SRO layer and find a transient enhancement of the depolarizing field with lasting detrimental effects on the polarization. Exploiting the ISHG response, we are able to correlate the transient enhancement of the depolarizing field to the bad metallic properties of the top electrode when the electrode thickness is below 2 u. c. Beyond advancing the understanding of polarization evolution in heterostructures, the access to the origin of the polarization loss allows us to design a route to stabilize in-situ a net polarization in a thin ferroelectric layer integrated into a capacitor. By thermally annealing the capacitor after a sufficiently thick electrode is deposited, we stabilize an as-grown single-domain configuration of the ferroelectric layer. Hence, with this work we reveal the consequence of the evolution of the electrostatic environment on polarization during the growth. Though the electrostatic environment is only transiently unfavorable, the resulting transient enhancement of the depolarizing field has lasting consequences on the ferroelectric response.

The results summarized in this chapter are published as [30]:
N. Strkalj, G. De Luca, M. Campanini, S. Pal, J. Schaab, C. Gattinoni, N. A. Spaldin, M. D. Rossell, M. Fiebig, and M. Trassin. "Depolarizing-Field Effects in Epitaxial Capacitor Heterostructures", *Phys. Rev. Lett.* **123**, 147601 (2019). The manuscript can be found in its entirety in Appendix A.

4.1 Polarization suppression in ferroelectric-based capacitors

The depolarizing field is long recognized as a notorious and fundamental challenge to the stability of out-of-plane polarization in thin films, even in ferroelectric films with metallic layers at both interfaces for thickness well above the critical thickness of the ferroelectric film [21–24]. It is however difficult to understand the impact of the depolarizing field in ferroelectric capacitors post-deposition because the polarization suppression occurs already during the growth [30, 71, 168] and because the ferroelectric layer is inaccessible for PFM once capped with the top electrode.

We investigate the domain configuration in a ferroelectric-based SRO|BTO|SRO capacitor for a BTO thickness above the critical thickness for ferroelectricity *before* and *after* the deposition of the top SRO layer. An uncapped BTO film of 30 u. c. thickness has a single-domain upwards polarization, see Fig. 4.1(a,b). To access the domain configuration once the ferroelectric layer is integrated into a capacitor, we remove the top electrode by nanomachining with a diamond-coated PFM tip without affecting the BTO polarization (Fig. 4.1(c,d)) [170, 196, 197]. In the exposed BTO area, we find a multi-domain configuration of out-of-plane-polarized domains [57], see Fig. 4.1(e). We therefore attribute the polarization suppression of a ferroelectric-based capacitor to domain formation. Counterintuitively, a ferroelectric film without a top metallic layer can sustain a net polarization, but a ferroelectric film screened at both interfaces by metallic layers forms domains.

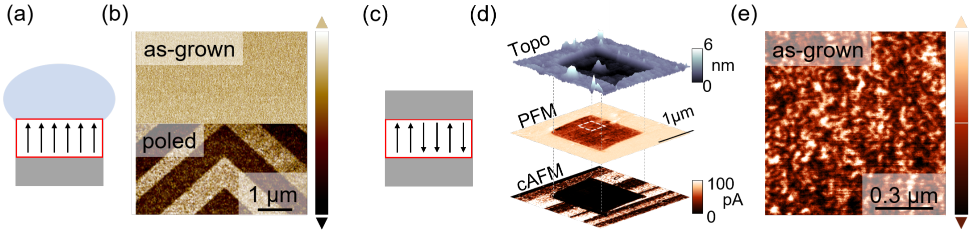

Figure 4.1: (a) Schematic of a single-domain configuration in a SRO|BTO heterostructure. The metallic electrode at the bottom interface is depicted in grey and the charge-screening environment at the top interface in blue. (b) PFM out-of-plane data of the as-grown domain configuration (top) and after repeated poling (bottom). (c) Schematic of a multi-domain configuration in an SRO|BTO|SRO capacitor. (d) Topography and corresponding out-of-plane PFM and conductive atomic force microscopy (cAFM) data after nanomachining away the SRO top electrode to expose the BTO. The removal is visible as a step in the topography image (c), as an enhancement of PFM signal (d), and as suppressed conduction (e) in the exposed BTO area. (e) Resonant PFM out-of-plane data of the as-grown domain configuration.

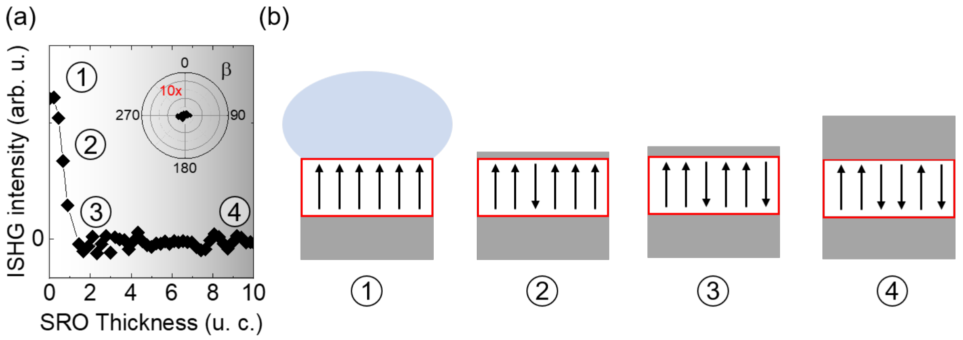

Figure 4.2: (a) ISHG signal tracking the BTO thin film polarization during the growth of top SRO layer. The inset shows the SHG anisotropy obtained after the growth by simultaneously varying the light polarization angle of the incident fundamental (1200 nm) and the detected SHG (600 nm) light. (b) Schematic of charge screening at interfaces of the ferroelectric layer in a BTO|SRO|BTO capacitor at the SRO thickness marked in (a). ① Charge screening through oxygen gas in the growth chamber. ② Absence of charge screening from an insulating SRO layer of 1 u. c. thickness. ③ Absence of charge screening from an insulating SRO layer of 2 u. c. thickness. ④ Charge screening through a metallic SRO layer of 10 u. c. thickness.

4.2 Transient enhancement of depolarizing field

We move on to identifying the cause of the striking domain formation and suppression of net polarization by ISHG. By monitoring the onset of ISHG intensity during the growth of the BTO, we find a critical thickness of 5 u. c. on the SRO buffer of 10 u. c. thickness, see 3.4(b). This critical thickness is in agreement with the theoretical calculations, which predict a critical thickness of 6 u. c. [72, 198]. The polarization is found to saturate for BTO films beyond 20 u. c. thickness.

It is insightful to observe the polarization evolution during the deposition of the top electrode using ISHG, see Fig. 4.2(a). With the start of the SRO deposition, the ISHG intensity abruptly decreases because of the nucleation of domains with downwards polarization in the as-grown domain configuration with upwards polarization (Fig. 4.2(b)①). After the deposition of a single u. c. of the SRO layer, the ISHG intensity is reduced to half (Fig. 4.2(b)②). After the deposition of 2 u. c. of the SRO layer, the ISHG intensity is entirely suppressed (Fig. 4.2(b)③). By continuing the deposition of the SRO layer of 10 u. c. thickness, matching the thickness of the bottom SRO layer, no further change of the ISHG intensity is observed (Fig. 4.2(b)④). No ISHG recovery is detected either during the cooling. We thus conclude that the domain formation occurs during the deposition of the first two u. c. of the SRO top electrode. Note that we excluded other possible causes of the ISHG reduction such as optical absorption, optical damaging, interface defects and strain relaxation.

By a combination of THz-TDS and ab initio calculations, we find that the origin of the domain formation is the thickness-dependent conductivity of the top electrode, here SRO [199–201]. A SRO layer with a thickness below 2 u. c. has a reduced conductivity, and does not provide the required charge screening to the ferroelectric layer for stabilizing a net polarization in contrast to the growth atmosphere which includes oxygen gas and ionic plasma species in the chamber. In this SRO thickness regime, the depolarizing field is thus transiently enhanced. At the thickness at which SRO becomes sufficiently metallic, the domain formation is already completed. No further evolution of the domain configuration is observed.

4.3 Discussion and outlook

Using ISHG, we directly access the impact of a dynamic charge-screening environment on polarization during the growth of a ferroelectric-based capacitor. Our observations explain the polarization suppression in the ultrathin regime of such heterostructures and pave a path to resurrecting a net polarization.

The polarization suppression observed in our ferroelectric-based capacitor is found to be linked to the reduced charge screening capacity of the SRO electrode in its low-thickness regime. The reduced conductivity in the low-thickness regime is not specific to SRO [199–201], but a property of most typical metal oxides, such as $La_{1-x}Sr_xMnO_3$ [202, 203], RuO_2 [204], and $LaNiO_3$ [205, 206]. In the common case of the presence of ferroelectricity during growth, the existence of an insulating state of the oxide electrode when its thickness is still low prevents charge screening at the top ferroelectric interface and causes domain formation in the ferroelectric layer [70, 207].

Now that we have established that domain formation in ferroelectric capacitors occurs as a result of the thickness-dependent conductivity of the top electrode, let us envision ways to resurrect the coveted single-domain configuration.

Thermal annealing

We tune the Curie temperature to an experimentally accessible value by choosing (110)-oriented GSO as the substrate, see Fig. 3.4(c). We complete the capacitor growth as described above. We evidence a multi-domain configuration in the ferroelectric layer by the absence of ISHG response, see Fig. 4.3(a,c). We then increase the temperature to above the Curie temperature, see Fig. 4.3(b). Finally, we cool the capacitor and observe a strong SHG response at room temperature, see Fig. 4.3(c,e). Because now the ferroelectricity emerges in the charge-screening environment of sufficiently thick electrodes (both 10 u. c.), it assumes a single-domain configuration.

Electric-field poling

Alternatively, one can apply an electric field to pole the as-grown multi-domain configuration into a single-domain configuration, see Fig. 4.3(f,g) However, the as-grown multi-domain configuration leads to domain walls that attract defects during the cooling. It is thus more favorable to avoid domain formation in the first place.

The access to the polarization evolution during the integration of a ferroelectric layer into a prototypical device architecture presents a step forward towards controlled domain structures in ferroelectric-based heterostructures which is the key requirement for any ferroelectric application. In Chapter 5, we will use ISHG to unravel the polarization dynamics occurring during the growth process of the ferroelectric layer.

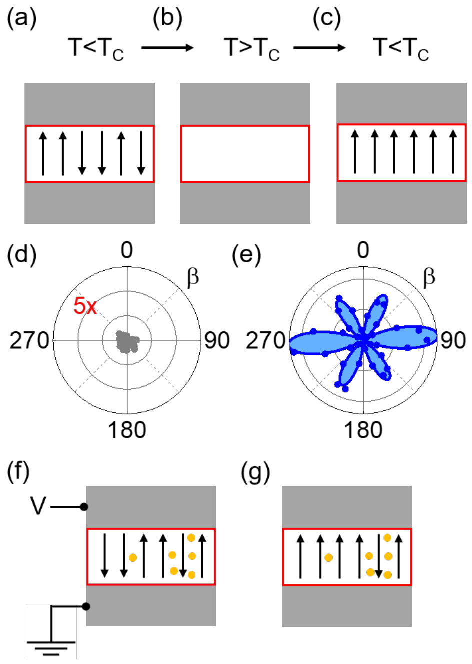

Figure 4.3: (a–c) Sketch of the thermal annealing process, T is the temperature of the heterostructure and T_C is the critical temperature. (d,e) ISHG anisotropy measurements at two stages of the annealing process. (d) After the SRO capping, the SHG yield is zero because of destructive multi-domain SHG interference. (f) Thermal annealing recovers the SHG signal and, hence, a single-domain configuration is stabilized at room temperature. (f–g) Sketch of the electric-field poling. (f) A voltage is applied to the ferroelectric layer with a multi-domain configuration. (g) After the poling, multi-domain configuration remains partially pinned by defects. Yellow dots indicate defects accumulating at domain walls.

Polarization dynamics in ultrathin ferroelectrics

5

In the previous chapter, we saw how using ISHG can unravel the transient enhancement of the depolarizing field with lasting detrimental effects on the net polarization during the growth of the top electrode of a ferroelectric-based capacitor. In this chapter, we explore the dynamics of polarization during the growth process of the ferroelectric layer itself. ISHG allows us to observe the polarization evolution under the influence of only the bottom interface during growth, and under the influence of both interfaces at halted growth. To explain the polarization evolution at a growth interruption, we consider the influence of each interface on the polarization direction. We develop the concept of interface configurations in which we refer to the interfaces as “competitive” when each interface promotes an opposite polarization direction, and as “cooperative” when both interfaces promote the same polarization direction. We investigate the consequences of these interface configurations on the ferroelectric response. We find that competitive interfaces lead to polarization suppression, short retention time of a polarization switch and high susceptibility to a depolarizing field and, thus, multi-domain formation. In contrast, cooperative interfaces lead to polarization enhancement, long retention time of a polarization switch and robustness against the depolarizing field in favour of retaining a single-domain configuration. Such as single-domain configuration is stable in an unfavorable electrostatic environment. This concept of varying interface configurations is envisioned as a powerful route for engineering the polarization in thin-film ferroelectrics towards energy-efficient electronics.

The results presented in this chapter are published as [155]:
N. Strkalj, C. Gattinoni, A. Vogel, M. Campanini, R. Haerdi, A. Rossi, M. D. Rossell, M., N. A. Spaldin, M. Fiebig, and M. Trassin. “In-situ Monitoring of Interface Proximity Effects on Polarization in Ultrathin Ferroelectrics”, *Nat. Commun.* **11**, 5815 (2020). The manuscript can be found in its entirety in Appendix B.

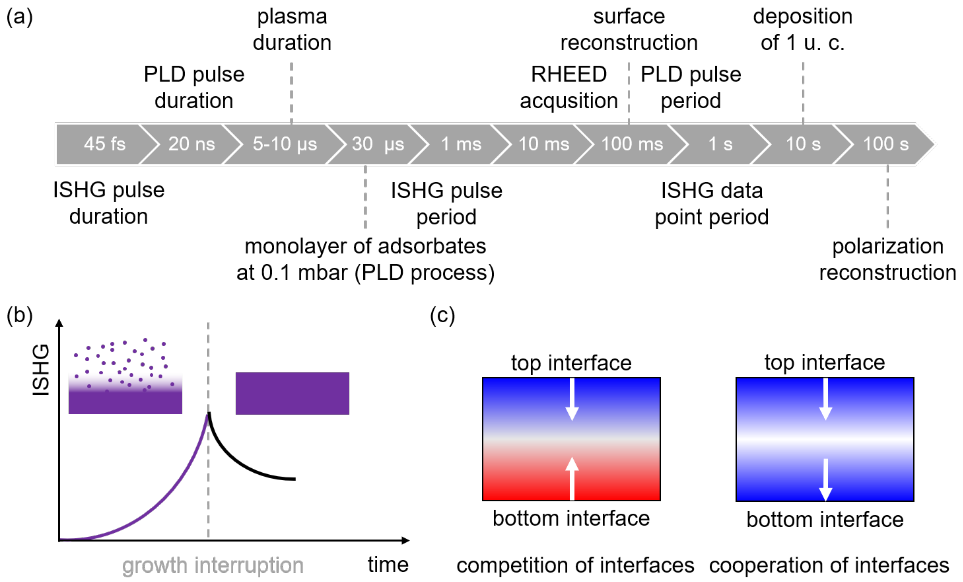
(a)
plasma duration
surface reconstruction
deposition of 1 u. c.
PLD pulse duration
RHEED acqusition
PLD pulse period
45 fs
20 ns
5-10 μs
30 μs
1 ms
10 ms
100 ms
1 s
10 s
100 s
ISHG pulse duration
ISHG pulse period
ISHG data point period
monolayer of adsorbates at 0.1 mbar (PLD process)
polarization reconstruction
(b)
ISHG
growth interruption
time
(c)
top interface
bottom interface
top interface
bottom interface
competition of interfaces
cooperation of interfaces

Figure 5.1: (a) An overview of extrinsic and intrinsic timescales involved in the ISHG probing of ferroelectric thin films. (c) Schematic of the ISHG signal tracking polarization evolution. Insets show schematics of ongoing and halted deposition. During the growth, only the influence of the bottom interface is observed (purple line). Once the growth is interrupted, the joint influence of the bottom and the top interface is observed (black line). (b) Schematic of the concept of competitive (left) and cooperative (right) interfaces.

5.1 Separation of the impact of an individual interface on the polarization state

In ferroelectric thin films, interfaces play a decisive role in determining the final polarization state. For films with out-of-plane polarization, charge screening at interfaces is dominant in setting the polarization direction. So far, either the charge screening at the bottom interface [29, 30, 74] or at the top interface [32–36] was engineered to set the polarization direction. Simultaneously engineering both interfaces is hampered by the lack of experimental access to the contributions of both interfaces individually. ISHG offers us a unique opportunity to separate the impact of an individual interface by monitoring the polarization dynamics during ongoing and halted growth.

To understand the ISHG monitoring of polarization dynamics in the PLD process, it is important to have an overview of the involved timescales, see Fig. 5.1(a).

Extrinsic timescales

For the thin-film synthesis by PLD, we use an excimer laser with a pulse duration of 20 ns, and the pulses are sent every 0.1–1 s. Probing of the thin-film properties during the synthesis is conducted by RHEED and ISHG.

RHEED has an acquisition time of 10–100 ms. For the ISHG measurement, the laser probe has a pulse duration of 45 fs, and pulses are sent once per millisecond and are integrated to one ISHG data point per second. The deposition of a single u. c. lasts about 10 s in all PLD processes conducted throughout this thesis.

Intrinsic timescales

Under the typical oxygen gas pressure of 0.1 mbar, the plasma created in the PLD process has a lifetime of 5–10 µs [208], and it takes 30 µs to cover the surface with a monolayer of adsorbates. The surface reconstruction lasts about 0.1–0.5 s [141, 209]. The polarization reconstruction due to defect migration lasts 100–1000 s [28].

Because the timescale of the polarization reconstruction due to defect migration is much longer ($>$100 s) than the pulse period of the thin-film synthesis (0.1–1 s), the polarization cannot accommodate to the influence of the top interface during the growth, but only when the growth process is halted. By monitoring polarization during ongoing and halted deposition, we can separate the contribution of the individual interfaces in setting the polarization state, see Fig. 5.1(b).

During the growth, we observe the transient polarization governed by only the bottom interface. Once the growth is halted, the polarization reconstructs under the complementary influence of the top interface. The joint effect of both interfaces sets the final ferroelectric response.

We propose a concept of competitive and cooperative configurations of interfaces in which the bottom- and the top-interface contributions favor opposite or equal polarization directions, Fig. 5.1(c). From the change in the ISHG signal when the growth is halted, we can determine the respective interface configuration. At a growth interruption, a reduction of ISHG intensity occurs for the configuration of competitive interfaces and an enhancement of ISHG intensity for the configuration of cooperative interfaces.

5.2 Consequences of competitive and cooperative configurations of interfaces

Here we scrutinize the competitive and cooperative interface configurations in PTO films on (001)-oriented STO. To achieve the two interface configurations, we engineer the charge screening at the bottom interface to favor either upwards or downwards polarization. In contrast, the charge screening at the top interface is found to always favor downwards polarization.

Bottom interface

We employ atomic-scale interface engineering to set the polarization direction at the bottom interface. We use LSMO as the bottom electrode which

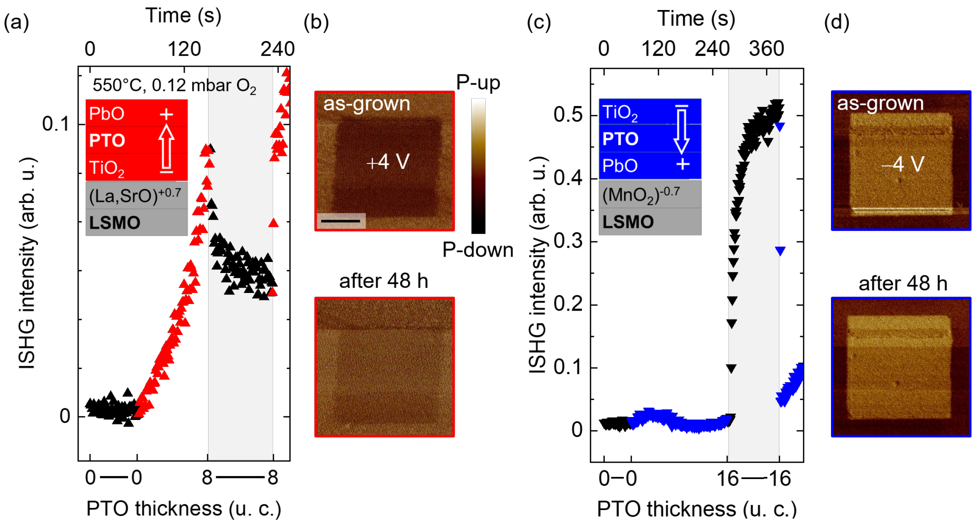

Figure 5.2: (a) ISHG signal tracking the PTO thin film polarization during ongoing (filled red symbols, 0–8 u. c.) and halted (filled black symbols) growth. The time axis for this growth protocol reveals relaxation of the polarization on the order of 10^2 s. The inset shows the chemistries of interfacial planes at the PTO|LSMO interface and the polarization direction set by the bottom interface. (b) PFM out-of-plane data immediately after the poling (±4 V) and 48 h later for the competitive interface configurations. PTO film is 20 u. c. thick and scale bar is 1 µm. (c) ISHG signal during ongoing (filled blue symbols, 0–16 u. c.) and halted (filled black symbols) growth. The inset shows the chemistries of interfacial planes at the PTO|LSMO interface and the polarization direction set by the bottom interface. (d) PFM out-of-plane data immediately after the poling (±4 V) and 48 h later for the cooperative interface configurations. PTO film is 20 u. c. thick and scale bar is 1 µm.

has either a negative MnO$_2^{-0.7}$ or a positive La$_{0.7}$Sr$_{0.3}$O$^{+0.7}$ interface termination. Since the interface termination carries charge, it sets the polarization direction at the bottom interface of the ferroelectric layer to downwards and upwards for the negatively and positively charged interface termination, respectively.

Top interface

Charged defects set the polarization direction at the top interface of the PTO. In specific, we evidence post-deposition excess Pb in the form of Pb adatoms at the top interface by angle-resolved XPS and EDX analysis. We model the effect of the Pb excess by ab initio calculations [87]. We find that the Pb adatoms result in a positively charged top interface upon their adsorption and thus favor downwards-pointing polarization, independent of the influence of the bottom interface.

In our ISHG experiment, we monitor the polarization emergence and evolution during the growth of the PTO films. During halted growth, polarization suppression is observed for competitive interfaces (Fig. 5.2(a)) and polarization enhancement is observed for cooperative interfaces (Fig. 5.2(c)). We highlight the far-reaching consequences of the interface configuration on the robustness of polarization.

We first scrutinize the dipole moments in the ferroelectric layer using STEM post-deposition. For competitive interfaces, STEM evidences a suppression of dipole moments throughout the thickness and a reversal of the direction of dipole moments at the topmost u. c. For cooperative interfaces, a pervasive bulk-like displacement is observed.

We then compare the poling behavior of the PTO layer obtained with the competitive interfaces to the poling behavior of the PTO layer obtained with cooperative interfaces (Fig. 5.3(b,d)). Though the polarization can be locally reversed by an electric field generated by a PFM tip in both interface configuration, the reversal of polarization in the poled area has a longer retention time in the PTO layer with cooperative interfaces than in the PTO layer with cooperative interface.

We finally test the polarization response to a change in the electrostatic environment. We cap the PTO layers with dielectric STO and metallic LSMO, and observe the polarization response using SHG. For both STO and LSMO capping, the PTO layer with the configuration of competitive interfaces suppresses its net polarization through nanoscale domain formation [29, 210–213]. In stark contrast, the PTO layer with the configuration of cooperative interfaces remains in a single-domain configuration, even in the unfavorable electrostatic environment of a capping with a high dielectric permittivity.

5.3 Discussion and outlook

We show how the combined influence of both interfaces in a ferroelectric film determines its ferroelectric response. ISHG enables unprecedented access to contributions of individual interfaces in setting the polarization state that can otherwise not be disentangled post-deposition. With the insight to polarization dynamics using ISHG, we explain the joint effect of interfaces within the concept of competitive and cooperative interface configurations. The understanding of the contributions of both interfaces in setting the final polarization state is shown to be vital for stabilizing a robust polarization, even in an unfavorable electrostatic environment.

We further expect our findings on polarization dynamics to be relevant for all ferroelectric-based heterostructures in which interfacial chemistry and charge imbalance play an important role [214, 215]. Though in our case, the influence of the the top interface was determined by the specific growth process of an A-site volatile ferroelectric, our observations are valid (i) under different conditions at the top interface and (ii) in other ferroelectric materials. (i) For example, in our current heterostructures, the use of a Pb-excess target, fast deposition rate and fast cooling rate results in the Pb excess accumulating at the top interfaces which favors downwards polarization. Changing the target composition or prolonging the

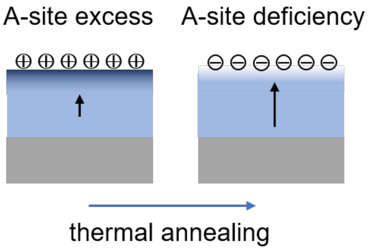

Figure 5.3: Schematic of changing the influence of the top interface by thermal annealing. Annealing converts the structure with A-site excess at the top interface (left) to a structure with A-site deficiency at the top interface (right).

exposure of the heterostructure to elevated temperatures would favor Pb volatility and Pb deficiency [27]. In this scenario, we can imagine that Pb vacancies would form at the top interface which would favor an upwards polarization, see Fig. 5.3. (ii) In analogy to the role of defects in A-site volatile ferroelectrics, other mechanisms could drive the polarization direction at interfaces of other materials such as surface adsorbates or free charge in neigboring layers.

The use of the non-invasive SHG tool to monitor the polarization during the growth is invaluable in engineering polarization in the simple domain structures studied in Chapter 4 and Chapter 5. In Chapter 6, we will explore the potential of the SHG tool in identifying more complex ordering of dipole moments in multilayers.

Non-invasive probing of phase coexistence in ferroelectric|dielectric heterostructures

6

In ferroelectric|dielectric PTO|STO heterostructures, energy contributions of strain and electrostatics are in a delicate equilibrium, which leads to the stabilization of phases that are known is literature as complex phases [37, 38, 40–45, 126–128]. Complex phases host non-collinear dipole moments that form nanoscale arrays which are thus between domains and domain walls. One example of a complex phase is the so-called vortex phase. In the vortex phase, non-collinear dipole moments arrange into a circle and this array is repeated along the orthogonal direction to the plane of the circle. Identifying the presence of complex phases is however challenging because of the ordering of dipole moments along multiple axes. Emergence of phase coexistence can further hamper the investigation. In this chapter, we will shed light on the ordering of dipole moments in PTO|STO heterostructures using SHG. We stabilize the phase coexistence of the ordered multi-domain phase with in-plane polarization and the so-called vortex phase. By measuring and modelling the SHG polarimetry, we detect the presence of phase coexistence both in a PTO|STO superlattice, as well as in a PTO|STO bilayer. We furthermore observe an extended phase- and inverted domain-coupling effect in PTO|STO multilayers leading to an antiparallel alignment of local polarization in neighboring ferroelectric layers. We show that SHG modelling of polarimetry is a promising tool for the identification of new complex phases and their host systems. In a more general context, our results pave the way towards using SHG for monitoring evolution of arrays of dipole moments during the use of ferroelectric-based heterostructures in applications.

The work presented in this chapter is found in the attached manuscript:
N. Strkalj, A. Bortis, M. Campanini, M. D. Rossell, M. Fiebig, and M. Trassin. "Optical second harmonic signature of phase coexistence in ferroelectric|dielectric heterostructures", *in preparation* (2021). The manuscript can be found in its entirety in Appendix C.

6.1 Ordering of dipole moments in a ferroelectric|dielectric superlattice

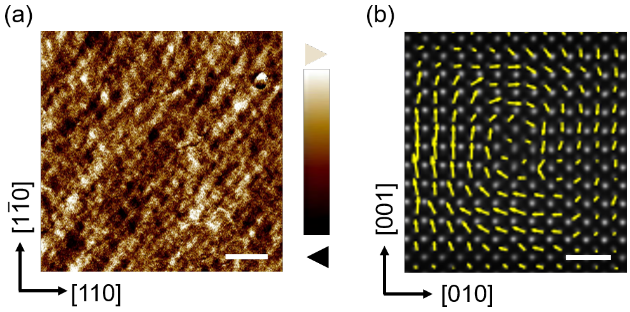

Figure 6.1: (a) LPFM image of the phase coexistence of the a_1/a_2 phase and the vortex phase in a PTO|STO superlattice. Scale bar is 1 µm. (b) Post-deposition STEM map of the dipole moments in the vortex phase in a PTO|STO superlattice. Yellow arrows show the direction and magnitude of the dipole moments. Scale bar is 1 nm.

We deposit a PTO$_{12}$|STO$_{12}$ superlattice on SRO-buffered (110)-oriented DSO substrates [216, 217]. Ferroelectric layers of our superlattice host the phase coexistence of (i) the so-called a_1/a_2 phase and (ii) the so-called vortex phase [38–40, 42, 44]. All directions henceforth refer to the pseudocubic axes of the DSO substrate The phases are separated in stripes with a width of about 200 nm along the [010] direction, and a length of about 2 µm along the [100] direction, see Fig. 6.1(a).

(i) In the a_1/a_2 phase, domains arrange in stripes alternating between a_1-domains and a_2-domains, as introduced in Subsection 2.1.2. Domain walls in the a_1/a_2 domain structure lie along [110] and [1$\bar{1}$0] directions. Individual *a*-domains have a width of about 10 nm. (ii) In the vortex phase, dipole moments are perpendicular to the radial vector from the vortex core and continuously change direction around the vortex core [218], see Fig. 6.1(b). Arrays of dipole moments are further observed to form pairs of vortices and anti-vortices with clockwise and anticlockwise rotation of the dipole moments around the vortex core, respectively. The central axis of the vortices and antivortices is parallel to [010] direction. The vortex phase possesses an additional polarization along the central axis which is set by the net polarization of the neighboring *a*-domains, see Fig. 6.2. Each vortex has a lateral extension of about 5 nm.

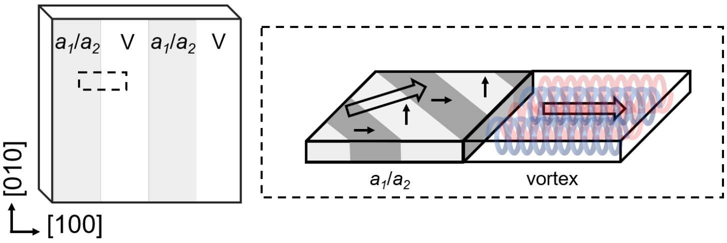

Figure 6.2: A schematic of the phase coexistence of the a_1/a_2 phase and the vortex phase (V) in our PTO|STO heterostructures. An enlarged schematic of the area within the dashed rectangle is given on the right. Filled black arrows represent the polarization direction in the a_1/a_2 phase and the blue and red spirals represent the direction of dipole moments in the vortex phase. Empty black arrows indicate the direction of net polarization.

6.2 Optical response of phase coexistence

Detecting the emergence of phase coexistence in $\text{PTO}_{12}|\text{STO}_{12}$ heterostructures requires extensive characterization because the ordering of dipole moments occurs along multiple axes and at multiple length scales. Let us discuss the advantages and drawbacks of detecting phase coexistence in $\text{PTO}_{12}|\text{STO}_{12}$ heterostructures with the techniques that are employed so far.

STEM is the only characterization tool that allows local mapping of dipole moments [37, 38, 40–45, 126–128]. However, the use of STEM is arduous and destructive to the sample. It is therefore unsuited for routine sample checks and operando studies.

XRD can detect nanoscale periodicity of orientations of dipole moments [183, 210–212, 219–222], but cannot access their local order arrangement. Using XRD to detect complex phases further requires the use of synchrotron facilities or the superlattice architecture.

PFM can detect microscale separation of phases, but not the sub-resolution ordering of individual *a*-domains or vortices. The PFM technique is also limited in probing polarization in ultrathin layers of thickness below 10 nm because of the leakage current. Detecting polarization in such ultrathin layers therefore also requires the use of the superlattice architecture.

We explore the use of the table-top non-invasive SHG to characterize phase coexistence in our PTO|STO superlattice. We measure the SHG polarimetry in normal-incidence geometry that is sensitive only to in-plane polarization, see Section 3.2 and Fig. 6.3(a). We first model the SHG contributions by considering only the a_1/a_2 phase, i. e. equal χ_{ijk} tensor components for local spontaneous polarization along [100] and [010] directions, see Fig. 6.3(b,c). This model cannot reproduce the measured response. We therefore consider an additional contribution of the net axial polarization of the vortex phase with spectrally different χ'_{ijk}

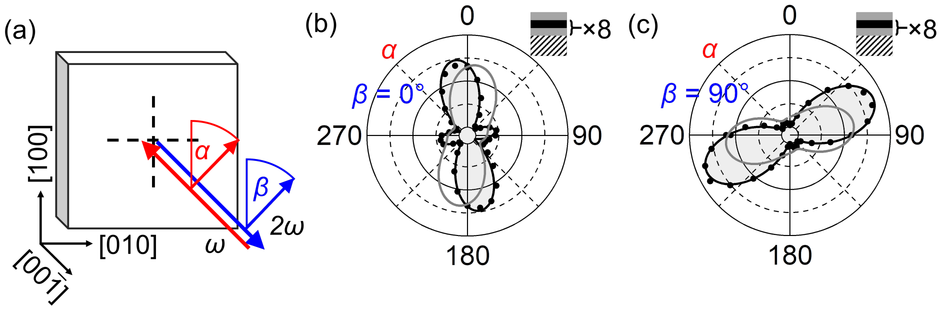

Figure 6.3: (a) (a) Schematic of the SHG setup in the employed normal-incidence geometry. Crystallographic directions refer to the pseudocubic axes of the $DyScO_3$ substrate. The incoming light propagates along [001] at 1200 nm with a linear polarization set to the angle α. The generated non-linear signal at 600 nm is analyzed in its polarization state using an analyzer fixed to the angle $\beta = 0°$. (b,c) Polar plots of SHG intensity (points) versus incident-light polarization angle α for a PTO|STO superlattice with (b) $\beta = 0°$ and (c) $\beta = 90°$. Grey and black lines are theoretical fits of the one-phase model and the two-phase model, see details in Appendix C. Schematic of the multilayer is given in the inset top right. Grey denotes PTO, black denotes STO, and hatching denotes the $SrRuO_3$-buffered $DyScO_3$ substrate. The intensity scale is equal in (b) and (c).

tensor components. We find that modelling the SHG polarimetry is only possible if both the SHG contribution of the a_1/a_2 phase and the SHG contribution of the vortex phase are taken into consideration, see details in Appendix C.

6.3 Discussion and outlook

We detect the phase coexistence of the a_1/a_2 phase and the vortex phase in $PTO_{12}|STO_{12}$ presence on SRO-buffered DSO substrate using SHG. We then compare the SHG response of a series of PTO|STO heterostructures that consist of a different number of repetitons of the PTO and the STO layers. All heterostructures are deposited on SRO-buffered DSO substrate, and the thickness of an individual PTO or STO layer is 12 u. c.

The SHG response of a PTO|STO bilayer is equivalent to the SHG response of the PTO|STO superlattice in terms of the relations of the tensor components. Our optical approach can thus detect the phase coexistence even in heterostructures with a single ferroelectric layer of 12 u. c. thickness, unlike the XRD and PFM.

Surprisingly, the overall SHG yield of a PTO|STO bilayer is even stronger than the SHG yield of a superlattice, while the SHG yield of a sample with two PTO layers (PTO|STO|PTO trilayer) completely vanishes. This points to destructive interference of the SHG waves from individual layers in PTO|STO multilayers. We conclude that the destructive interference of SHG waves is linked to interlayer coupling. Specifically, the phases extend and the domain walls align vertically throughout the heterostructure. However, the direction of local polarization in neigboring layers is found to be antiparallel.

Future studies should investigate the generality of the relations of the tensor components observed in the vortex phase of the $\mathrm{PTO}_{12}|\mathrm{STO}_{12}$ heterostructures to other complex phases or other systems [39, 127, 130, 131, 223–230]. Furthermore, because of its non-invasive nature, SHG could be employed to monitor the manipulation of complex phases in ferroelectric thin films [40, 42, 132, 231–233]. Such operando access could be crucial for the development of applications that rely on complex phases [122, 123, 133–136].

We will explore manipulation of an ordered multi-domain structures with in-plane polarization using electric trailing field of a scanning-probe tip in Chapter 7.

Manipulation of in-plane polarization using electric trailing field

7

In-plane polarization offers several advantages for applications, such as the inherent robustness of the in-plane polarization because of the absence of depolarizing field effects. It is, however, not only challenging to determine the nanoscale domain structure of in-plane polarized films, but also to manipulate it deterministically because of the presence of polarization along multiple axes and directions [234]. In this chapter, we present the stabilization of an in-plane polarized domain structure in the PTO|STO superlattice with ultrathin layers. We use the electric trailing field of the scanning-probe tip to manipulate the as-grown multi-domain configuration. Starting from the as-grown domain configuration with four polarization directions, we locally manipulate domains to either stabilize two polarization directions or a single polarization direction. This deterministic control over the domain population within an extended area constitutes a step forward in the design of devices based on in-plane polarization.

The results presented in this chapter are published as [235]:
N. Strkalj, M. Bernet, M. F. Sarott, J. Schaab, M. Fiebig, and M. Trassin. "Stabilization and Manipulation of In-plane Polarization in a Ferroelectric|Dielectric Superlattice", *J. Appl. Phys.* **129**, 174104 (2020) The manuscript can be found in its entirety in Appendix D.

7.1 Stabilization of in-plane polarization

Ordered multi-domain structures with in-plane polarization typically arise in ferroelectric layers under the influence of tensile epitaxial strain. In our $\mathrm{PTO}_{12}|\mathrm{STO}_{12}$ superlattice on a metallic SRO buffer under the tensile strain of a (110)-oriented GSO substrate [210, 236], we stabilize the so-called aa_1/aa_2 phase, see Fig. 7.1. In the aa_1/aa_2 phase, domains arrange in stripes alternating between aa_1-domains and aa_2-domains, as introduced in Subsection 2.1.2. Domain walls in the aa_1/aa_2 phase lie along [100] and [010] directions. This domain structure was theoretically proposed in tensile-strained films [217, 237, 238]. It was previously stabilized only using chemical tensile strain [239].

We employ the superlattice architecture to provide sufficient volume of the ferroelectric material for the investigation of the domain configuration [183, 211, 212, 221, 236, 240, 241]. In the case of a superlattice with ultrathin layers, electrostriction at interfaces triggers domain wall propagation throughout the PTO|STO interfaces [39, 211, 227, 230, 242]. All ferroelectric layers thus host an equivalent domain configuration with respect to the positions of domain walls.

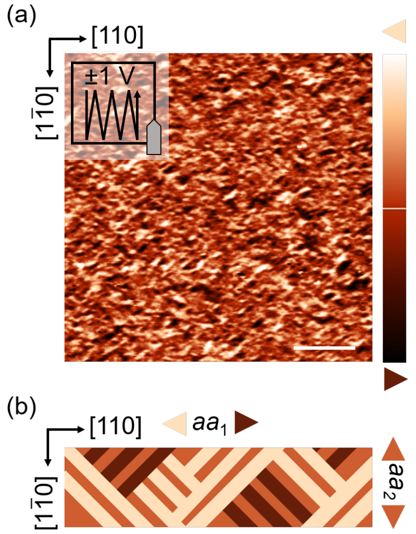

Figure 7.1: (a) LPFM of a PTO|STO superlattice on an SRO-buffered (110)-oriented GSO substrate. Crystallographic directions refer to the PTO tetragonal lattice. The scale bar is 2 µm. Sketches represent the tip and scanning orientation with respect to the crystallographic axes. (b) Schematic of the domain configuration with polarization directions in the aa_1/aa_2 domain structure indicated on top and left sides.

7.2 Manipulating nanoscale domains with in-plane polarization by the electric trailing field

In-plane polarization can be manipulated with electric fields applied either with planar interdigitated electrodes [243–245] or by the scanning-probe tip [175–180, 246–248]. Here we use the electric trailing field of the scanning-probe tip as schematized in Fig. 7.2(a).

For a stationary tip at a positive voltage with respect to the sample, an in-plane electric field is applied radially away from the tip apex. During scanning, the tip moves across the sample in a zigzag pattern. The resulting electric trailing field results along the slow scanning axis in the direction opposite to the slow scanning direction for the positive voltage of a scanning-probe tip (Fig. 7.2(b)). No net electric field results along the fast scanning axis.

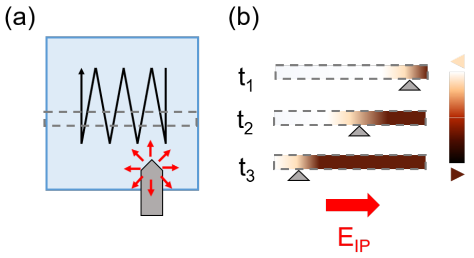

Figure 7.2: (a) Schematic of the application of a electric trailing field with a scanning-probe tip at a positive voltage with respect to the sample. Sketches represent tip (gray), scanning trace (black zigzag line) and the in-plane electric field (red arrows). An area elongated along the slow scanning axis is outlined in dashed grey. (b) The sketch of the polarization direction after the application of an in-plane electric field of a scanning-probe tip (gray) within the outlined area is depicted at three time points $t_1<t_2<t_3$. The resulting electric trailing field E_{IP} is directed opposite to the slow scanning axis (thick red arrow).

We manipulate the polarization of the nanoscale multi-domain configuration by applying the electric trailing field at either 45° to the polarization directions of two *aa*-domain variants or in the polarization direction of an *aa*-domain variant. After poling with an electric trailing field applied at 45° to the polarization directions of two *aa*-domain variants, only regions of these two domain variants are present within the poled area, see Fig. 7.3(b). After poling with an electric trailing field applied in the polarization direction of an *aa*-domain variant, that single variant of the *aa*-phase is stabilized within the poled area, see Fig. 7.3(c).

7.3 Discussion and outlook

We stabilize the aa_1/aa_2 phase in a PTO|STO superlattice with an average as-grown domain size of 30 nm. Such a large domain size for ultrathin ferroelectric layers of 12 u. c. thickness presents a deviation from the square-root law, as discussed in Subsection 2.1.2 and as previously observed in single ferroelectric layers [246, 249–251].

Furthermore, we show a high degree of control over the domain configuration via application of in-plane electric trailing fields. By poling the as-grown domain configuration in the polarization direction of one domain variant of the aa_1/aa_2 phase, we deterministically create single-domain regions of that domain variant with a lateral extension of up to hundreds of μm^2. Strikingly, no change to the poled single-domain regions is observed over a 90-day time period at ambient conditions.

Future studies should also focus on domain walls in the aa_1/aa_2 domain structure. Using the electric-trailing field of the scanning probe tip, we could write

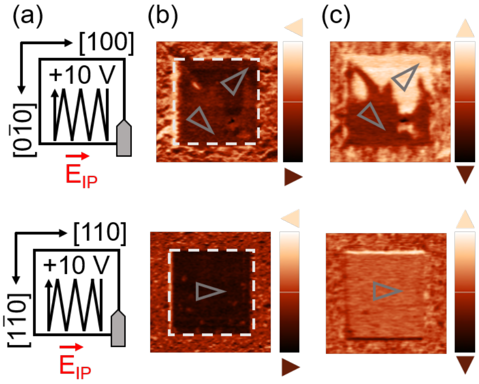

Figure 7.3: (a) Sketches representing tip (gray), scanning trace (zigzag line) with respect to the crystallographic axes and the resulting in-plane electric trailing field E_{IP}. (b) LPFM and (c) VPFM images resulting after the application of the in-plane electric trailing field to the 2.5×2.5 μm^2 (top) and 5×5 μm^2 (bottom) areas highlighted by the white dashed outline.

domain walls between domains that have a controlled polarization direction and investigate the conduction properties of these domain walls [171, 246, 252–257].

Ultimately, our results on manipulating in-plane polarization help establish applications where avoiding depolarizing field effects is necessary.

Conclusion and outlook

8

The work presented in this thesis covers the emergence and evolution of ferroelectricity in films of model perovskite oxides. During this thesis, a highly sensitive, yet non-invasive, tool – ISHG – is developed to access polarization during the growth of ferroelectric thin films. The use of ISHG reveals previously elusive transient phenomena occurring during the growth of ferroelectric thin films. Because these transient phenomena have lasting consequences on the polarization in a ferroelectric layer, ISHG is indispensable in understanding the ferroelectric response. The information obtained by ISHG further allows to engineer robust net polarization in ferroelectric-based heterostructures which is desired in application.

Furthermore, we investigate complex ordering of dipole moments in multilayers using SHG and their electric-field manipulation. The achieved identification of such complex ordering using a non-invasive approach and the controlled manipulation of an ordered multi-domain structure present steps towards operando studies of ferroelectric-based heterostructures.

In particular, in Chapters 4 and 5, we have seen that employing a nonlinear optical approach right where the film functionality — polarization — is set, i. e. during growth, gives insight into the emergence of polarization, its dynamics during halted growth and its evolution in a multilayer architecture. We began by showing in Chapter 4 the transient effects of the depolarizing-field enhancement on the polarization in a SRO|BTO|SRO capacitor. We found the origin of the resulting domain formation in the thickness-dependent conduction properties of the top SRO electrode. This insight enabled us to stabilize a single-domain configuration in a ferroelectric capacitor that could not be achieved from standard post-deposition characterization. After establishing the importance of interface contributions in the setting of the polarization state in Chapter 4, we next investigated the dynamics of polarization during the deposition process of a PTO film in Chapter 5. We monitored the influence of a single interface during growth in contrast to the joint influence of both interfaces at the growth interruption. The independent access to the contribution of each interface in setting of the polarization state allowed us to develop the concept of configurations of competitive and cooperative interfaces. In the case of cooperative interfaces, we stabilized a robust polarization state in terms of polarization magnitude, retention of a polarization reversal and resilience to an unfavorable electrostatic environment.

In Chapers 6 and 7, we moved on to multilayers of PTO|STO to explore more complex ordering of dipole moments. As a first step, in Chapter 6 we discuss the measured and modelled optical SHG response of the PTO|STO heterostructures hosting phase coexistence of a_1/a_2 domains and complex arrays of dipole moments. We evidenced the high sensitivity of SHG in probing such domain structure even in single ultrathin layers, suggesting opportunities for non-invasive identification of other complex arrays of dipole moments. Finally, we presented the stabilization and manipulation of the aa_1/aa_2 domain structure in Chapter 7. We achieved large single-domain regions in this ordered multi-domain structure using in-plane electric trailing field of a scanning-probe tip. This deterministic control over the domain population is essential for the design of devices based on in-plane polarization.

In the past 100 years, ferroelectric materials have made the journey from their first discovery to being "mainstream" components in electronics. Ferroelectric applications are more and more based on their intrinsic properties of a switchable polarization and bound charge at interfaces, then on the concomitant properties occurring in ferroelectric materials. The results obtained during this thesis showcase the value of non-invasive access to polarization in overcoming the challenges of integrating ultrathin ferroelectrics into applications. The information obtained from SHG lead, on the one hand, to the understanding of the ferroelectric response in oxide heterostructures, and on the other hand, to a playground for tuning the ferroelectric response for targeted functionalities.

Contributions to this thesis

This work presented in thesis is a result of scientific collaborations. Here I specify the contributions of myself and others in each chapter. Sample preparation and characterization was performed at ETH Zurich, except for the STEM characterization which was performed at Empa. The work was initiated and supervised by Manfred Fiebig and Morgan Trassin.

Chapter 3 PLD, RHEED and ISHG characterization were performed by me and Gabriele De Luca. PFM and XRD characterization were performed by me. STEM analysis was performed by Marco Campanini and Marta D. Rossell. THz-TDS measurements were performed by Shovon Pal. XPS analysis was performed by Antonella Rossi.

Chapter 4 PLD and ISHG characterization were performed by me and Gabriele De Luca. PFM characterization was performed by me, Jakob Schaab and Morgan Trassin. The density functional theory (DFT) calculations were performed by Chiara Gattinoni and Nicola A. Spaldin. THz-TDS was performed by Shovon Pal. STEM was performed by Marco Campanini and Marta D. Rossell.

Chapter 5 I performed the thin-film growth, PFM measurements, ISHG characterization and XRD analysis. Chiara Gattinoni, Rea Haerdi and Nicola A. Spaldin performed the DFT calculations. Alexander Vogel, Marco Campanini and Marta D. Rossell carried out the STEM investigations. Antonella Rossi performed the XPS characterization.

Chapter 6 The thin-film growth, SHG characterization and PFM measurements were performed by me. The SHG model was developed by me and Amadé Bortis. Amadé Bortis performed the Monte Carlo simulations. STEM was performed by Marco Campanini and Marta D. Rossell.

Chapter 7 I performed the thin-film growth. The structural XRD analysis was performed by me, Martin Sarott and Thomas Weber. PFM measurements were performed by Marco Bernet and Jakob Schaab.

Appendices

Depolarizing-field effects in epitaxial heterostructures

A

Reprint: N. Strkalj, G. De Luca, M. Campanini, S. Pal, J. Schaab, C. Gattinoni, N. A. Spaldin, M. D. Rossell, M. Fiebig, and M. Trassin. “Depolarizing-Field Effects in Epitaxial Capacitor Heterostructures”, *Phys. Rev. Lett.* **123**, 147601 (2019). Copyright American Physical Society (2020). Supplementary information is available online.

Depolarizing-Field Effects in Epitaxial Capacitor Heterostructures

N. Strkalj,[1,*,†] G. De Luca,[1,*] M. Campanini,[2] S. Pal,[1] J. Schaab,[1] C. Gattinoni,[1] N. A. Spaldin,[1]
M. D. Rossell,[2] M. Fiebig,[1] and M. Trassin[1,‡]
[1]*Department of Materials, ETH Zurich, CH-8093 Zürich, Switzerland*
[2]*Electron Microscopy Center, Empa, Swiss Federal Laboratories for Materials Science and Technology, CH-8600 Dübendorf, Switzerland*

(Received 30 November 2018; revised manuscript received 8 April 2019; published 4 October 2019)

We identify a transient enhancement of the depolarizing field, leading to an unexpected quench of net polarization, during the growth of a prototypical metal-ferroelectric-metal epitaxial system made of $BaTiO_3$ and $SrRuO_3$. Reduced conductivity and, hence, charge screening efficiency in the early growth stage of the $SrRuO_3$ top electrode promotes a breakdown of ferroelectric $BaTiO_3$ into domains. We demonstrate how a thermal annealing procedure can recover the single-domain state. By tracking the polarization state *in situ*, using optical second harmonic generation, we bring new understanding to interface-related electrostatic effects in ferroelectric capacitors.

DOI: 10.1103/PhysRevLett.123.147601

The demand for ever-smaller and energy-efficient devices drives the development of ultrathin ferroelectrics with a robust polarization state and reliable switching properties [1–5]. However, the macroscopic polarization can be lost when the ferroelectric is implemented into the required metal-ferroelectric-metal thin-film capacitor heterostructure [6,7] since interface-related effects can drastically alter the polarization behavior [8–12]. For example, uncompensated bound surface charges at epitaxial ferroelectric interfaces result in a depolarizing field, which can trigger a drop of the ferroelectric Curie temperature (T_c) or nanoscale domain splitting [13–17]. Furthermore, ferroelectric layers are usually grown below T_c [18–21], so that their polarization state is set during the heterostructure growth [22–24]. Here the deposition process and the accompanying transient electrostatic effects at the metal-ferroelectric interface govern the resulting polarization state. Hence, understanding the growth dynamics and promoting the involved depolarization fields towards a robust remnant polarization and a controlled domain distribution in the ultrathin regime poses a key challenge on the way to ultrathin functional ferroelectric heterostructures and devices [25].

In this Letter, we identify microscopic physical mechanisms determining the depolarizing field and domain formation in a prototypical metal-ferroelectric-metal epitaxial heterostructure, $SrRuO_3|BaTiO_3|SrRuO_3$ (SRO|BTO|SRO). We track the evolution of the ferroelectric order during the deposition by laser-optical *in situ* second harmonic generation (ISHG) [24]. We find that the first unit cells of the top electrode exhibit reduced conductivity and, hence, insufficient charge screening. This triggers a ferroelectric multidomain breakdown manifesting as net-polarization quench. The unprecedented insight into the growth process allows us to develop a procedure controlling the influence of the depolarizing field by thermal annealing. While previous thin-film studies on the depolarizing field in ferroelectrics are restricted to uncapped specimens or periodic domain patterns [14,21], we reveal explicit mechanisms controlling the net polarization of ultrathin ferroelectrics in capacitor heterostructures. This is all the more important since any metallic layer in a heterostructure begins its existence as ultrathin film, becoming "thick" only upon ongoing deposition. Our findings support the development of oxide electronics because they shed light on a hitherto inaccessible yet crucial aspect: the evolution of the oxide multilayer heterostructure, right where its functionalities are coined with the deposition of the first monolayers.

We study the polarization state in a model ferroelectric capacitor system composed of a ferroelectric BTO thin film between two metallic SRO electrodes. Uniaxial ferroelectric BTO (001) films with a thickness of 30 unit cells (u.c.) were grown by pulsed laser deposition (PLD) on (001)-oriented $SrTiO_3$ (STO) buffered by 10 u.c. of SRO. The substrate exerts ≈2.2% compressive strain, increasing the ferroelectric Curie temperature (T_c) above the growth temperature ($T_{growth} = 650\,°C$) [19]; further details on growth conditions are available in Ref. [26]. Room-temperature ferroelectric properties were confirmed using piezoresponse force microscopy (PFM). The high-quality single-domain as-grown state of the BTO and its local switching behavior are depicted in Figs. 1(a) and 1(b).

We monitor the ferroelectric response during the thin-film deposition using ISHG as a noninvasive detection technique. SHG denotes frequency doubling of a light wave in a material. This process is sensitive to the loss of inversion symmetry and therefore occurs with the emergence of ferroelectric order [46–48]. The ISHG signal is measured in 45° reflection geometry and its polarization is chosen such that it detects the out-of-plane component of

© 2019 American Physical Society

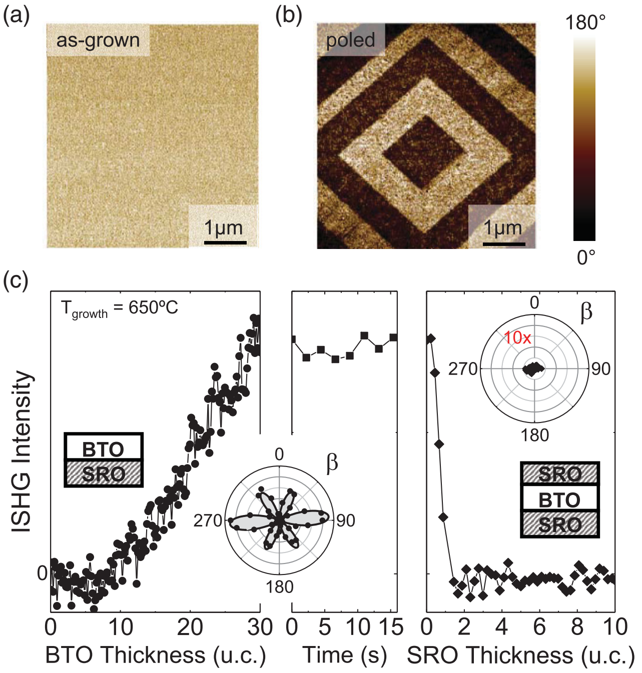

FIG. 1. Evolution of polarization during SRO|BTO|SRO capacitor design. (a)–(b) PFM phase images showing out-of-plane contrast of compressively strained BTO grown on SRO-buffered STO, with ±10 V applied to the scanning tip. (c) ISHG signal during the growth of BTO on SRO-buffered STO (left panel) at $T_{\mathrm{growth}} = 650\,^{\circ}\mathrm{C}$, during hold time after the completion of the BTO layer (middle panel) and during subsequent deposition of the top SRO layer (right panel). The insets show the ISHG anisotropy obtained by simultaneously varying the polarization angle (β) of the incident fundamental (1200 nm) and the detected SHG (600 nm) light. The simulations are plotted as continuous lines. Note that in the right panel no signal is recovered after cooling to room temperature.

the ferroelectric polarization emerging in the BTO during the deposition process [49]. Reflection high energy electron diffraction (RHEED) is performed simultaneously with ISHG to ensure the growth quality and to calibrate the ISHG yield to the thickness with u.c. accuracy [26].

Figure 1(c) presents the ISHG signal during the deposition of the BTO and the SRO cap layer of the SRO|BTO|SRO||STO heterostructure. The left panel confirms an onset of the ferroelectric BTO polarization at a critical thickness of 5 u.c. on SRO||STO [24,50]. The ISHG anisotropy measurement in the inset is characteristic of the tetragonal point-group symmetry 4*mm* of the BTO with an out-of-plane orientation of the spontaneous polarization. The ISHG data combined with *ex situ* PFM-phase measurements [Fig. 1(a)] show the single-domain nature of our BTO films. This indicates that the depolarizing field in BTO is suppressed by sufficient charge screening exerted by the 10 u.c. bottom SRO and the oxygen-rich growth atmosphere [51–54].

We now follow the BTO polarization state during the subsequent deposition of the SRO cap layer. Most strikingly, the ISHG intensity drops to zero with the growth of only 2 u.c. of SRO, see right panel of Fig. 1(c) (with an error of ±0.5 u.c. [26,55]). This net-polarization quench is startling as it suggests the emergence of a strong depolarizing field, which is in contradiction to the expected metallic nature of the SRO. The ISHG drop cannot be attributed to probe-laser damage because sustained irradiation of the completed BTO film does not yield an ISHG decrease (middle panel). Linear absorption of the ISHG light passing an SRO cap layer of 2 u.c. results in an intensity decrease of less than 10% [24] and cannot explain its complete quench either.

The ISHG signal breakdown could result from strain relaxation and/or chemical disorder at the interface, which might lower T_c and push the BTO into the paraelectric phase. Therefore, we investigated the strain state, the local atomic structure, and the chemical composition of the SRO|BTO|SRO||STO trilayer. For this, a spherical-aberration-corrected FEI Titan Themis microscope operated at 300 kV and equipped with ChemiSTEM technology was used; see Ref. [26] for more details. The post-deposition scanning-transmission-electron-microscopy (STEM) analysis in Fig. 2 reveals that the BTO layer sustains the in-plane strain state from the substrate. Hence, we rule out a strain-relaxation-induced drop of T_c as a cause of the ISHG quench. Alternatively, pinned dipoles at $\mathrm{RuO_2}$|BaO-terminated interfaces were reported to suppress the polarization of BTO [56]. For verifying this, the atomic species at the interfaces were resolved using atomic-resolution energy-dispersive x-ray (EDX) spectroscopy. The sharp SRO|BTO interface shows very little interdiffusion. In addition, we found that both interface terminations are SrO|$\mathrm{TiO_2}$, ultimately excluding the role of interface chemistry in the ISHG loss.

Exclusion of the aforementioned mechanisms leaves electrostatic effects [57,58] as likely explanation of the ISHG quench. Insufficient charge screening by the top SRO electrode could result in an enhanced depolarizing field and concomitant multidomain or paraelectric-state formation and thus, net-polarization breakdown. However, as the bottom electrode shows, 10 u.c. of SRO screen the BTO charges sufficiently, according to the single domain state of the BTO layer in Fig. 1(a).

We therefore need to consider the charge screening efficiency of an SRO top electrode below 10 u.c. thickness, a stage that our heterostructure inevitably undergoes during the deposition of the final 10 u.c. electrode. We used density functional theory (DFT) to explore the SRO metallicity in the ultrathin regime. We calculated the density of states (DOS) at the Fermi energy (E_F) as a function of the SRO thickness. Calculations were performed with the PBEsol functional [59] using the VASP code [60] with the PAW approach [61]. Plane waves were cut off at an energy of 500 eV and a $6 \times 6 \times 6$ Monkhorst-Pack grid was used for a single perovskite unit cell. A Hubbard-U term [62] with $U_{\mathrm{eff}} = 2.0$ eV was applied to the d orbitals of Ru. Our top

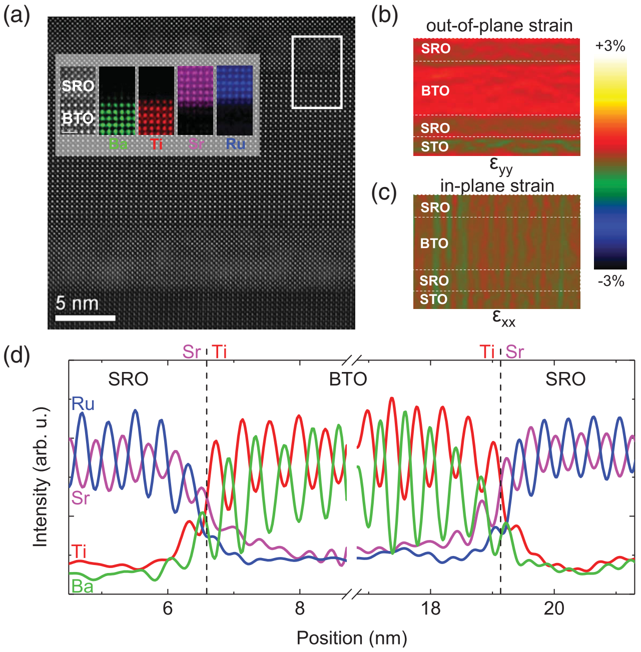

FIG. 2. Analysis of strain state and atomic species at the interfaces of SRO|BTO|SRO capacitor. (a) Atomically resolved structure using high-angle annular dark-field STEM. The inset shows the EDX analysis indicating an atomically sharp BTO|SRO interface with very limited interdiffusion. (b)–(c) Strain maps showing the out-of-plane (b) and in-plane (c) lattice parameter variation relative to the STO substrate lattice constant. The SRO|BTO|SRO capacitor is coherently strained in-plane to the SRO substrate excluding strain relaxation as the polarization suppression mechanism. (d) Interface termination by EDX spectroscopy. Both SRO|BTO|SRO interfaces have SrO|TiO_2 termination which is not detrimental to the polarization state [56]. Hence, the preservation of strain, minimal degree of interdiffusion, and interface chemistry suggest electrostatic effects as an explanation for the net-polarization quench in Fig. 1.

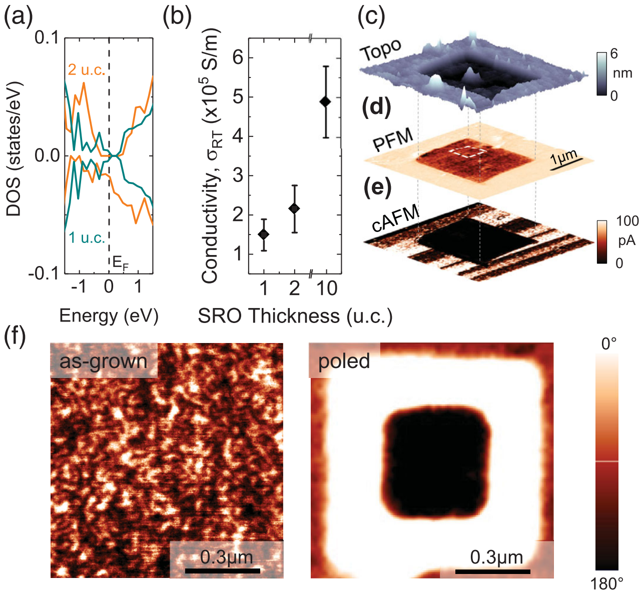

FIG. 3. Origin of the BTO net-polarization quench. (a) DFT calculations compare the DOS at E_F for different thicknesses of SRO. The antiferromagnetic 1 u.c. thick SRO film is insulating, as shown by the zero DOS at E_F. The ferromagnetic 2 u.c. thick SRO and thicker films are metallic according to the finite DOS at E_F. (b) Terahertz time-domain spectroscopy measurements show a continuous decrease in top SRO conductivity σ_{RT} with layer thickness. (c)–(e) Topography and corresponding out-of-plane PFM and conductive atomic force microscopy (cAFM) data after nanomachining away the SRO top electrode to expose the BTO. The removal is visible as a step in the topography image (c), as an enhancement of PFM signal (d), and as suppressed conduction (e) in the exposed BTO area. (f) Resonant PFM of the as-grown exposed BTO surface reveals a multidomain pattern in the PFM phase. Voltage tip poling in the area on the right recovers a single-domain state, confirming the preservation of ferroelectricity in the BTO. The bright area is down-polarized with a positive tip voltage and the dark area is up-polarized with a negative tip voltage.

SRO|BTO electrode is coherently strained to the STO substrate; see Figs. 2(b) and 2(c). Furthermore, the interface termination at the top SRO|BTO is SrO|TiO_2; see Fig. 2(d). In the calculations, we therefore considered an SRO|BTO heterostructure with the experimentally relevant in-plane STO substrate lattice parameter, SrO|TiO_2 interface termination, and upwards ferroelectric polarization of the BTO layer. A heterostructure of 5 u.c. BTO and n u.c. SRO was relaxed. The SRO is in the $P4/mbm$ space group while the BTO has neither octahedral rotations nor tilts [63]. Forces were converged to 5×10^{-3} eV/Å^2. We found that an insulating antiferromagnetic configuration is preferred below a thickness of 2 u.c., while the metallic ferromagnetic configuration is preferred at 2 u.c. and higher thicknesses; see Fig. 3(a). In line with this, previous reports on SRO showed a thickness-related metal-insulator transition in similar systems [64–66]. Experimentally, we extracted the optical conductivity of the 1, 2, and 10 u.c. SRO cap layers in the SRO|BTO|SRO||STO system from reflectance spectra measured by terahertz time-domain spectroscopy [26–29]. Our results in Fig. 3(b) are in agreement with the previous measurements on SRO films [30,31] and show a pronounced reduction of conductivity towards thinner SRO layers. The reduction in conductivity together with the diminishing thickness leads to a continuous decrease in screening efficiency from bulklike to a monolayer. The poorly conducting 1–2 u.c. thick SRO abruptly isolates the BTO from the charge-screening oxygen-rich growth atmosphere [53,54] and enhances the depolarizing field.

For a direct verification of the depolarizing-field-induced multidomain breakdown, we image the domain state of our heterostructures by PFM. Using the ISHG real-time feedback, we deposited the amount of SRO required for a net-polarization quench, subsequently removing the SRO by nanomachining with a diamond-coated PFM tip. There is a risk that the mechanical forces in this procedure might affect the domain state. However, in earlier tomographic PFM characterization, this was not observed [32]. The absence of BTO surface degradation or mechanical switching induced by this process [67] was verified by AFM in the nanomachined area [26]. By exposing the BTO, we can probe its domain state by high-resolution resonant PFM and confirm that the cap SRO deposition has led to the formation of a 180° domain maze pattern with an average domain width of 30 ± 10 nm [68]. Preservation of the ferroelectric nature of this state is evidenced by reversible tip poling of the polarization with ±10 V in the exposed area; see PFM phase images in Fig. 3(f).

How can we bypass the transient depolarizing field enhancement and thus recover the single-domain ferroelectric state of the BTO in the final capacitor heterostructure? Wide-area electric-field poling via the SRO electrodes shows limited efficiency because of pinned and randomly oriented domains at local defects or interfaces [69–71]. As an alternative, we should be able to delete the ferroelectric state entirely by a heating cycle through T_c and recover the single-domain ferroelectric state of the BTO on cooling, provided that the thermal treatment is performed once the SRO cap layer reaches the thickness at which it is sufficiently metallic. When cooling the sample from above T_c, the buildup of the transient depolarizing field is now avoided, and a single-domain state should result.

For verifying this approach, we use strain engineering to reduce T_c to reach an experimentally accessible value and to avoid sample deterioration by the annealing cycle. We consider three different substrates: STO (lattice mismatch $\eta = -2.2\%$), (110)-oriented $DyScO_3$ (DSO) ($\eta = -1.2\%$) and (110)-oriented $GdScO_3$ (GSO) ($\eta = -0.6\%$). The ISHG signal during the BTO growth in Fig. 4(a) confirms the single-domain ferroelectric state of the BTO for all three substrates with lower polarization for lower epitaxial compressive stress. In Fig. 4(b), temperature-dependent SHG shows the reduction of T_c with the reduction of compressive stress, finally leading to an accessible $T_c = 720\,°\mathrm{C}$ on GSO.

We therefore apply the annealing cycle to the SRO|BTO|SRO||GSO. The ISHG anisotropy in Fig. 4(c) reveals that the single-domain state is quenched, as with the STO substrate, by the deposition of the first layers of SRO cap electrode. After completing the heating cycle through T_c, the ISHG yield and its light polarization dependence are completely restored [26]. The annealing process is schematized in Fig. 4(d). The result of the annealing experiment is another strong confirmation that the transient enhancement of the depolarizing field, caused by imperfect charge screening in the early stage of the top electrode deposition, explains the multidomain breakdown, rather than chemical intermixing or termination effects, that would not be eliminated by the annealing. More importantly, we see that annealing is an attractive alternative to the notoriously difficult electric-field poling in establishing an as-grown single-domain ferroelectric heterostructure in the ultrathin regime.

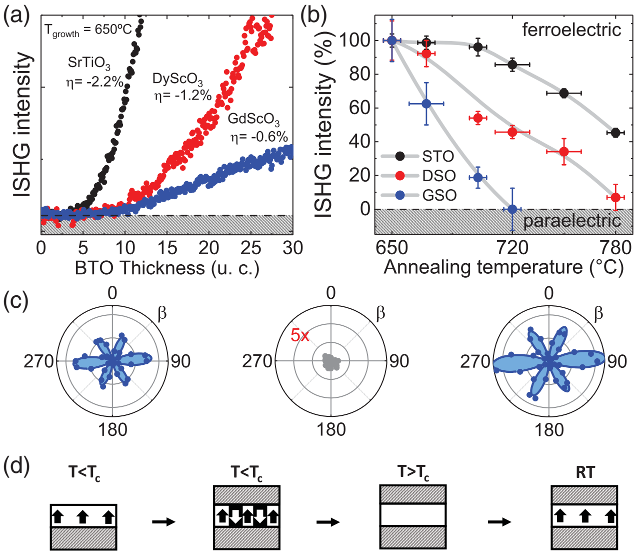

FIG. 4. Domain engineering in SRO|BTO|SRO by thermal annealing. (a) ISHG signal during BTO growth on SRO buffered (001)-STO ($\eta = -2.2\%$), (110)-DSO ($\eta = -1.2\%$), and (110)-GSO ($\eta = -0.6\%$) substrates. (b) ISHG intensity as a function of temperature for different substrates, relative to the value at the end of growth ($T_{\mathrm{growth}} = 650\,°\mathrm{C}$). The decrease of T_c with decreasing lattice mismatch is used to suppress T_c for SRO|BTO|SRO on GSO sufficiently to heat it above T_c and reset the polarization state of the completed heterostructure. (c) ISHG anisotropy measurements at different stages of the annealing process. Single-domain polarization after the BTO|SRO||GSO growth (left). After the SRO capping, the signal yield is zero because of destructive multidomain SHG interference (middle). Thermal annealing recovers the initial ISHG signal and, hence, a single-domain state (right). Absolute ISHG intensities from BTO change with temperature and with the thickness of the SRO capping layer which absorbs the fundamental light. (d) Sketch of the annealing process. Data points in (b)–(c) were taken after realignment for temperature-induced mechanical drifts.

In summary, we have tracked the polarization state of a prototypical ferroelectric, $BaTiO_3$, throughout deposition of a metallic $SrRuO_3$ top electrode. Laser-optical *in situ* second harmonic generation, supported by density functional theory and terahertz time-domain spectroscopy, reveals a transient enhancement of the depolarization field because of the "bad" metallic nature of ultrathin $SrRuO_3$. We thus pinpoint insufficient charge screening as the origin of the resulting multidomain breakdown of the ferroelectric net polarization.

Because most of the commonly used metal-oxide electrodes exhibit a thickness-dependent conductivity [64–66,72–74], our conclusions are independent of the choice of the oxide material and the epitaxial growth technique. The ability to tune the depolarizing field during the deposition goes beyond the capacity to engineer the domain formation during growth. For instance, interfacial charge screening is a key ingredient in enhanced ferroelectric behavior [17] and the recently reported negative-capacitance heterostructures [75]. Therefore, our work, bringing awareness of the electrostatics dynamics during the heterostructure design, will stimulate not only the investigation of complex electrostatics in ultrathin ferroelectric heterostructures and superlattices but also at polar surfaces and interfaces in general.

The authors thank E. Gradauskaite for experimental assistance with scanning probe microscopy. This research was supported by the EU European Research Council (Advanced Grant No. 694955—INSEETO). M. F. thanks ETH Zurich and Center for Emergent Matter Science (CEMS) at RIKEN for support of his research sabbatical. M. C. and M. D. R. acknowledge support by the Swiss National Science Foundation under Project No. 200021_175926. S. P. acknowledges support by ETH Career Seed Grant No. SEED-17 18-1. C. G. acknowledges support by the European Union's Horizon 2020 research and innovation program under the Marie Skłodowska-Curie Grant Agreement No. 744027. The DFT calculations were supported by a grant from the Swiss National Supercomputing Centre (CSCS) under Project ID s798.

All authors discussed the results and contributed to the completion of the manuscript. N. S. and G. D. L. performed the thin film growth, SHG measurements, and developed the SHG fitting model. M. C. and M. D. R. carried out the STEM analysis. J. S., M. T., and N. S. performed the PFM investigation. S. P. performed the terahertz time-domain spectroscopy. C. G. and N. A. S. provided the DFT calculations. M. T. designed the experiment and supervised the work with M. F.

---

[*] These authors contributed equally to this work.

[†] nives.strkalj@mat.ethz.ch

[‡] morgan.trassin@mat.ethz.ch

[1] L. W. Martin and A. M. Rappe, Nat. Rev. Mater. **2**, 16087 (2016).

[2] K. M. Rabe, M. Dawber, C. Lichtensteiger, C. H. Ahn, and J.-M. Triscone, in *Physics of Ferroelectrics: A Modern Perspective* (Springer, Berlin, 2007), pp. 1–30.

[3] A. Chanthbouala, A. Crassous, V. Garcia, K. Bouzehouane, S. Fusil, X. Moya, J. Allibe, B. Dlubak, J. Grollier, S. Xavier, C. Deranlot, A. Moshar, R. Proksch, N. D. Mathur, M. Bibes, and A. Barthélémy, Nat. Nanotechnol. **7**, 101 (2012).

[4] A. Q. Jiang, X. J. Meng, D. W. Zhang, M. H. Park, S. Yoo, Y. J. Kim, J. F. Scott, and C. S. Hwang, Sci. Rep. **5**, 14618 (2015).

[5] M. Dawber, K. M. Rabe, and J. F. Scott, Rev. Mod. Phys. **77**, 1083 (2005).

[6] J. Junquera and P. Ghosez, Nature (London) **422**, 506 (2003).

[7] D. J. Kim, J. Y. Jo, Y. S. Kim, Y. J. Chang, J. S. Lee, J.-G. Yoon, T. K. Song, and T. W. Noh, Phys. Rev. Lett. **95**, 237602 (2005).

[8] A. K. Tagantsev and G. Gerra, J. Appl. Phys. **100**, 051607 (2006).

[9] C.-L. Jia, V. Nagarajan, J.-Q. He, L. Houben, T. Zhao, R. Ramesh, K. Urban, and R. Waser, Nat. Mater. **6**, 64 (2007).

[10] A. Cano and A. P. Levanyuk, arXiv:1408.2373.

[11] Y. J. Shin, Y. Kim, S.-J. Kang, H.-H. Nahm, P. Murugavel, J. R. Kim, M. R. Cho, L. Wang, S. M. Yang, J.-G. Yoon, J.-S. Chung, M. Kim, H. Zhou, S. H. Chang, and T. W. Noh, Adv. Mater. **29**, 1602795 (2017).

[12] S. K. Streiffer, J. A. Eastman, D. D. Fong, C. Thompson, A. Munkholm, M. V. Ramana Murty, O. Auciello, G. R. Bai, and G. B. Stephenson, Phys. Rev. Lett. **89**, 067601 (2002).

[13] A. M. Bratkovsky and A. P. Levanyuk, Phys. Rev. Lett. **84**, 3177 (2000).

[14] C. Lichtensteiger, S. Fernandez-Pena, C. Weymann, P. Zubko, and J.-M. Triscone, Nano Lett. **14**, 4205 (2014).

[15] C. Lichtensteiger, M. Dawber, N. Stucki, J.-M. Triscone, J. Hoffman, J.-B. Yau, C. H. Ahn, L. Despont, and P. Aebi, Appl. Phys. Lett. **90**, 052907 (2007).

[16] C.-G. Duan, R. F. Sabirianov, W.-N. Mei, S. S. Jaswal, and E. Y. Tsymbal, Nano Lett. **6**, 483 (2006).

[17] G. Liu, J. Chen, C. Lichtensteiger, J.-M. Triscone, P. Aguado-Puente, J. Junquera, and N. Valanoor, Adv. Electron. Mater. **2**, 1500288 (2016).

[18] D. G. Schlom, L.-Q. Chen, C.-B. Eom, K. M. Rabe, S. K. Streiffer, and J.-M. Triscone, Annu. Rev. Mater. Res. **37**, 589 (2007).

[19] K. J. Choi, M. Biegalski, Y. L. Li, A. Sharan, J. Schubert, R. Uecker, P. Reiche, Y. B. Chen, X. Q. Pan, V. Gopalan, L.-Q. Chen, D. G. Schlom, and C. B. Eom, Science **306**, 1005 (2004).

[20] A. R. Damodaran, E. Breckenfeld, Z. Chen, S. Lee, and L. W. Martin, Adv. Mater. **26**, 6341 (2014).

[21] D. D. Fong, G. B. Stephenson, S. K. Streiffer, J. A. Eastman, O. Auciello, P. H. Fuoss, and C. Thompson, Science **304**, 1650 (2004).

[22] J. Sinsheimer, S. J. Callori, B. Ziegler, B. Bein, P. V. Chinta, A. Ashrafi, R. L. Headrick, and M. Dawber, Appl. Phys. Lett. **103**, 242904 (2013).

[23] B. Bein, H.-C. Hsing, S. J. Callori, J. Sinsheimer, P. V. Chinta, R. L. Headrick, and M. Dawber, Nat. Commun. **6**, 10136 (2015).

[24] G. De Luca, N. Strkalj, S. Manz, C. Bouillet, M. Fiebig, and M. Trassin, Nat. Commun. **8**, 1419 (2017).

[25] N. A. Spaldin and R. Ramesh, Nat. Mater. **18**, 203 (2019).

[26] See Supplemental Material at http://link.aps.org/supplemental/10.1103/PhysRevLett.123.147601 for growth conditions, RHEED patterns, and time-dependent intensity during the growth of SRO|BTO|SRO confirming the two-dimensional growth in Figs. S1 and S2; AFM topography scans of 1, 2, and 10 u.c. thick top SRO layers in Fig. S3; STEM polarization analysis in Fig. S4; details of the terahertz time-domain spectroscopy method and spectroscopy results (Figs. S5–S7); details on the absence of correlation between topography and high-resolution resonant PFM in the nanomachined area (Fig. S8); and time-dependent ISHG intensity at different steps of the annealing process in Fig. S9. All this includes Refs. [27–32] and [33–45].

[27] D. M. A. Mackenzie, P. R. Whelan, P. Bøggild, P. U. Jepsen, A. Redo-Sanchez, D. Etayo, N. Fabricius, and D. H. Petersen, Opt. Express **26**, 9220 (2018).

[28] S. Nashima, O. Morikawa, K. Takata, and M. Hangyo, Appl. Phys. Lett. **79**, 3923 (2001).

[29] G. Grüner, *Millimeter and Submillimeter Wave Spectroscopy of Solids* (Springer, Berlin Heidelberg, 1998).

[30] D. Geiger, U. S. Pracht, M. Dressel, J. Mravlje, M. Schneider, P. Gegenwart, and M. Scheffler, Phys. Rev. B **93**, 165131 (2016).

[31] P. Kostic, Y. Okada, N. C. Kollins, Z. Schlesinger, J. W. Reiner, L. Klein, A. Kapitulnik, T. H. Geballe, and M. R. Beasley, Phys. Rev. Lett. **81**, 2498 (1998).

[32] J. J. Steffes, R. A. Ristau, R. Ramesh, and B. Huey, Proc. Natl. Acad. Sci. U.S.A. **116**, 2413 (2019).

[33] S. Kobayashi, K. Inoue, T. Kato, Y. Ikuhara, and T. Yamamoto, J. Appl. Phys. **123**, 064102 (2018).

[34] V. Lucarini, J. J. Saarinen, K.-E. Peoponen, and E. M. Vartiainen, *Kramers-Kronig Relations in Optical Materials Research* (Springer, Berlin Heidelberg, 2005).

[35] C.-W. Chen, Y.-C. Lin, C.-H. Chang, P. Yu, J.-M. Shieh, and C.-L. Pan, IEEE J. Quantum Electron. **46**, 1746 (2010).

[36] N. Matsumoto, T. Hosokura, T. Nagashima, and M. Hangyo, Opt. Lett. **36**, 265 (2011).

[37] F. D. J. Brunner, A. Schneider, and P. Günther, Opt. Express **17**, 20684 (2009).

[38] M. Bass, *Handbook of Optics* (McGraw-Hill, New York, 1995), Vol. I.

[39] B. G. Alberding, R. Thurber, and E. J. Heilweil, J. Opt. Soc. Am. B **34**, 1392 (2017).

[40] P. Kužel and F. Kadlec, C.R. Phys. **9**, 197 (2008).

[41] P. Kužel, F. Kadlec, H. Němec, R. Ott, E. Hollmann, and N. Klein, Appl. Phys. Lett. **88**, 102901 (2006).

[42] J. Han, F. Wan, Z. Zhu, and W. Zhang, Appl. Phys. Lett. **90**, 031104 (2007).

[43] G. Koster, L. Klein, W. Siemons, G. Rijnders, J. S. Dodge, C.-B. Eom, D. H. A. Blank, and M. R. Beasley, Rev. Mod. Phys. **84**, 253 (2012).

[44] R. Kinjo, X. Weiming, I. Kawayama, H. Murakami, and M. Tonouchi, in *Proceedings of the 2011 International Conference in Infrared, Millimeter, and Terahertz Waves, Houston* (2011), https://doi.org/10.1109/irmmw-THz.2011.6104855.

[45] V. Garcia, M. Bibes, L. Bocher, S. Valencia, F. Kronast, A. Crassous, X. Moya, S. Enouz-Vedrenne, A. Gloter, D. Imhoff, C. Deranlot, N. D. Mathur, S. Fusil, K. Bouzehouane, and A. Barthélémy, Science **327**, 1106 (2010).

[46] M. Fiebig, V. V. Pavlov, and R. V. Pisarev, J. Opt. Soc. Am. B **22**, 96 (2005).

[47] S. A. Denev, T. T. A. Lummen, E. Barnes, A. Kumar, and V. Gopalan, J. Am. Ceram. Soc. **94**, 2699 (2011).

[48] J.-Y. Chauleau, E. Haltz, C. Carrétéro, S. Fusil, and M. Viret, Nat. Mater. **16**, 803 (2017).

[49] J. Nordlander, G. De Luca, N. Strkalj, M. Fiebig, and M. Trassin, Appl. Sci. **8**, 570 (2018).

[50] G. Gerra, A. K. Tagantsev, N. Setter, and K. Parlinski, Phys. Rev. Lett. **96**, 107603 (2006).

[51] R. V. Wang, D. D. Fong, F. Jiang, M. J. Highland, P. H. Fuoss, C. Thompson, A. M. Kolpak, J. A. Eastman, S. K. Streiffer, A. M. Rappe, and G. B. Stephenson, Phys. Rev. Lett. **102**, 047601 (2009).

[52] D. D. Fong, A. M. Kolpak, J. A. Eastman, S. K. Streiffer, P. H. Fuoss, G. B. Stephenson, C. Thompson, D. M. Kim, K. J. Choi, C. B. Eom, I. Grinberg, and A. M. Rappe, Phys. Rev. Lett. **96**, 127601 (2006).

[53] M. J. Highland, T. T. Fister, D. D. Fong, P. H. Fuoss, C. Thompson, J. A. Eastman, S. K. Streiffer, and G. B. Stephenson, Phys. Rev. Lett. **107**, 187602 (2011).

[54] G. B. Stephenson and M. J. Highland, Phys. Rev. B **84**, 064107 (2011).

[55] G. Rijnders and D. H. A. Blank, Appl. Phys. Lett. **84**, 505 (2004).

[56] H. Lu, X. Liu, J. D. Burton, C.-W. Bark, Y. Wang, Y. Zhang, D. J. Kim, A. Stamm, P. Lukashev, D. A. Felker, C. M. Folkman, P. Gao, M. S. Rzchowski, X. Q. Pan, C. B. Eom, E. Y. Tsymbal, and A. Gruverman, Adv. Mater. **24**, 1209 (2012).

[57] C. T. Black and J. J. Welser, IEEE Trans. Electron Devices **46**, 776 (1999).

[58] M. F. Chisholm, W. Luo, M. P. Oxley, S. T. Pantelides, and H. N. Lee, Phys. Rev. Lett. **105**, 197602 (2010).

[59] J. P. Perdew, A. Ruzsinszky, G. I. Csonka, O. A. Vydrov, G. E. Scuseria, L. A. Constantin, X. Zhou, and K. Burke, Phys. Rev. Lett. **100**, 136406 (2008).

[60] G. Kresse and J. Hafner, Phys. Rev. B **47**, 558 (1993).

[61] G. Kresse and D. Joubert, Phys. Rev. B **59**, 1758 (1999).

[62] S. L. Dudarev, G. A. Botton, S. Y. Savrasov, C. J. Humphreys, and A. P. Sutton, Phys. Rev. B **57**, 1505 (1998).

[63] M. Verissimo-Alves, P. García-Fernández, D. I. Bilc, P. Ghosez, and J. Junquera, Phys. Rev. Lett. **108**, 107003 (2012).

[64] D. Toyota, I. Ohkubo, H. Kumigashira, M. Oshima, T. Ohnishi, M. Lippmaa, M. Takizawa, A. Fujimori, K. Ono, M. Kawasaki, and H. Koinuma, Appl. Phys. Lett. **87**, 162508 (2005).

[65] J. Xia, W. Siemons, G. Koster, M. R. Beasley, and A. Kapitulnik, Phys. Rev. B **79**, 140407 (2009).

[66] X. Shen, X. Qiu, D. Su, S. Zhou, A. Li, and D. Wu, J. Appl. Phys. **117**, 015307 (2015).

[67] H. Lu, C.-W. Bark, D. Esque de los Ojos, J. Alcala, C. B. Eom, G. Catalan, and A. Gruverman, Science **336**, 59 (2012).

[68] A. Schilling, T. B. Adams, R. M. Bowman, J. M. Gregg, G. Catalan, and J. F. Scott, Phys. Rev. B **74**, 024115 (2006).

[69] A. M. Bratkovsky and A. P. Levanyuk, Phys. Rev. B **63**, 132103 (2001).

[70] P. Zubko, H. Lu, C.-W. Bark, X. Martí, J. Santiso, C.-B. Eom, G. Catalan, and A. Gruverman, J. Phys. Condens. Matter **29**, 284001 (2017).

[71] X.-K. Wei, Y. Yang, L. J. McGilly, L. Feigl, R. E. Dunin-Borkowski, C.-L. Jia, L. Bellaiche, and N. Setter, Phys. Rev. B **98**, 020102(R) (2018).

[72] G. Shibata, K. Yoshimatsu, E. Sakai, V. R. Singh, V. K. Verma, K. Ishigami, T. Harano, T. Kadono, Y. Takeda, T. Okane, Y. Saitoh, H. Yamagami, A. Sawa, H. Kumigashira, M. Oshima, T. Koide, and A. Fujimori, Phys. Rev. B **89**, 235123 (2014).

[73] Z. Liao, F. Li, P. Gao, L. Li, J. Guo, X. Pan, R. Jin, E. W. Plummer, and J. Zhang, Phys. Rev. B **92**, 125123 (2015).

[74] M. Golalikhani, Q. Lei, R. U. Chandrasena, L. Kasaei, H. Park, J. Bai, P. Orgiani, J. Ciston, G. E. Sterbinsky, D. A. Arena, P. Shafer, E. Arenholz, B. A. Davidson, A. J. Millis, A. X. Gray, and X. X. Xi, Nat. Commun. **9**, 2206 (2018).

[75] A. K. Yadav, K. X. Nguyen, Z. Hong, P. G. Fernández, P. Aguado-Puente, C. T. Nelson, S. Das, B. Prasad, D. Kwon, S. Cheema, A. I. Khan, C. Hu, J. Íñiguez, J. Junquera, L-Q. Chen, D. A. Muller, R. Ramesh, and S. Salahuddin, Nature (London) **565**, 468 (2019).

In-situ monitoring of interface proximity effects on polarization in ultrathin ferroelectrics

B

Reprint: N. Strkalj, C. Gattinoni, A. Vogel, M. Campanini, R. Haerdi, A. Rossi, M. D. Rossell, N. A. Spaldin, M. Fiebig, and M. Trassin. “In-situ Monitoring of Interface Proximity Effects on Polarization in Ultrathin Ferroelectrics”, *Nat. Commun.* **11**, 5815 (2020). Copyright Nature Springer (2020). Supplementary information is available online.

nature COMMUNICATIONS

ARTICLE

https://doi.org/10.1038/s41467-020-19635-7 OPEN

In-situ monitoring of interface proximity effects in ultrathin ferroelectrics

Nives Strkalj [1,4]✉, Chiara Gattinoni[1], Alexander Vogel [2,4], Marco Campanini [2], Rea Haerdi[1], Antonella Rossi[1,3], Marta D. Rossell [2], Nicola A. Spaldin [1], Manfred Fiebig [1] & Morgan Trassin [1]✉

The development of energy-efficient nanoelectronics based on ferroelectrics is hampered by a notorious polarization loss in the ultrathin regime caused by the unscreened polar discontinuity at the interfaces. So far, engineering charge screening at either the bottom or the top interface has been used to optimize the polarization state. Yet, it is expected that the combined effect of both interfaces determines the final polarization state; in fact the more so the thinner a film is. The competition and cooperation between interfaces have, however, remained unexplored so far. Taking $PbTiO_3$ as a model system, we observe drastic differences between the influence of a single interface and the competition and cooperation of two interfaces. We investigate the impact of these configurations on the $PbTiO_3$ polarization when the interfaces are in close proximity, during thin-film synthesis in the ultrathin limit. By tailoring the interface chemistry towards a cooperative configuration, we stabilize a robust polarization state with giant polarization enhancement. Interface cooperation hence constitutes a powerful route for engineering the polarization in thin-film ferroelectrics towards improved integrability for oxide electronics in reduced dimension.

---

[1] Department of Materials, ETH Zurich, 8093 Zurich, Switzerland. [2] Electron Microscopy Center, Swiss Federal Laboratories for Materials Science and Technology, Empa, 8600 Dübendorf, Switzerland. [3] Department of Chemical and Geological Sciences, University of Cagliari, 09124 Cagliari, Italy. [4] These authors contributed equally: Nives Strkalj, Alexander Vogel. ✉email: nives.strkalj@mat.ethz.ch; morgan.trassin@mat.ethz.ch

The two interfaces of a thin film are instrumental in setting its properties. Tight control over the interface configuration is therefore vital for applications. For example, in ferroelectric materials, a major obstacle to stabilizing the electric polarization in ultrathin layers is uncompensated bound charge at the interfaces[1–4]. Approaches to combat the resulting depolarizing field focus on acting on the bound charge at either the bottom interface by introducing metallic buffer electrodes[2,4] and atomic-scale interface engineering[5], or at the top interface by introducing charge-screening environments such as gases[6,7] or liquids[8–10]. Acting on both interfaces in the same experiment is hampered by the lack of separate, yet simultaneous experimental access for observing how these interfaces set the resulting polarization state of the film. Understanding such correlation becomes especially significant when the interfaces are separated by only a few nanometers.

Combined interface effects in ferroelectric thin films are most directly accessed by observing the spontaneous polarization right when it is formed—during assembly of the film in the growth chamber[11,12]. Using a laser-optical detection technique, in situ second harmonic generation (ISHG)[13], we achieve this in ferroelectric $PbTiO_3$ (PTO). We use PTO as a model system to explore the joint effects of two nanometer-spaced interfaces. We design and identify the influence of the bottom layer for itself and compare it to the influence exerted jointly by the PTO bottom and top interfaces, which we then relate to the resulting net polarization. Microscopic understanding is gained through scanning transmission electron microscopy (STEM), angle-resolved X-ray photoelectron spectroscopy (XPS), and first-principles calculations. Competitive and cooperative interface configurations are achieved by engineering the termination of the bottom interface to cause the film to exhibit either upwards or downwards polarization, while the top interface always promotes downwards polarization. In the cooperative case, giant polarization enhancement occurs when the influence of the top interface complements that of the bottom layer. Such fundamental understanding of proximity effects of thin-film interfaces should help to promote the integration of ultrathin ferroelectrics beyond previous limitations.

Results

We begin our investigation by monitoring the emergence of polarization in a PTO film using ISHG[13]. SHG denotes frequency doubling of a light wave in a material, a process sensitive to the absence of inversion symmetry. It therefore occurs with the onset of ferroelectric order, and with an amplitude that is proportional to the dipole moment and thickness in thin films[14,15]. All ISHG measurements were conducted under identical experimental conditions, see “Methods,” and the resulting intensities in arbitrary units can thus be quantitatively compared. Simultaneously, reflection high energy electron diffraction (RHEED) is performed to ensure the growth quality and to calibrate the ISHG yield to the film thickness with unit-cell (u. c.) accuracy.

The PTO film grown on $SrTiO_3$ (STO) substrate is buffered by a $La_{0.7}Sr_{0.3}O$-terminated (001)-oriented metallic $La_{0.7}Sr_{0.3}MnO_3$ (LSMO) layer which sets the macroscopic single-domain polarization upwards, away from the bottom interface[5]. Details of the growth of the ferroelectric films are reported in Supplementary Note 1. During PTO deposition, we observe a rather striking ISHG evolution (Fig. 1a). (i) Polarization emerges from the very first u. c., with subsequent increase of ISHG intensity with thickness. (ii) Upon interrupting the deposition, the ISHG evolution abruptly changes and the ISHG intensity gradually decreases to a new stable value, see Fig. 1b. (iii) Upon resuming the deposition, the ISHG intensity abruptly recovers to its pre-interruption value and continues to increase with thickness as in (i).

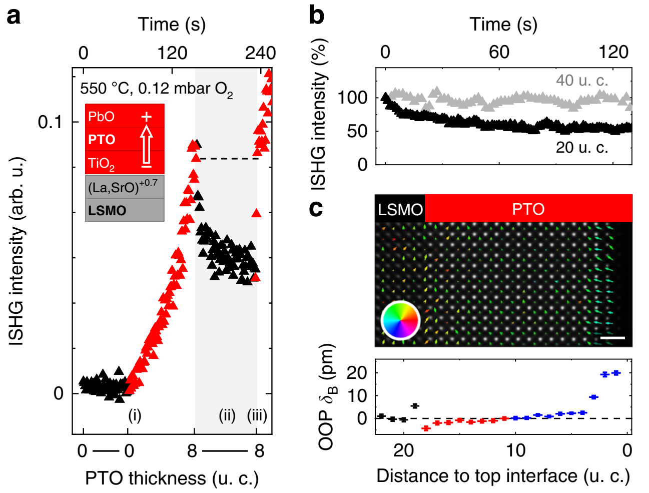

Fig. 1 Polarization suppression from competitive interfaces. a ISHG signal tracking the PTO thin-film polarization during ongoing (filled red symbols, 0–8 u. c.) and halted (filled black symbols) growth. The time axis for this growth protocol reveals relaxation of the polarization on the order of 10^2 s. The inset shows the chemistries of interfacial planes at the PTO|LSMO interface and the polarization direction set by the bottom interface. The dashed line indicates recovery of the ISHG intensity upon resuming the deposition. **b** Time-dependent ISHG signal after interrupting deposition, normalized to the maximum value = 100. **c** Post-deposition STEM map of the dipole moments. The arrows show the direction (color wheel) and amplitude (arrow length) of the associated dipole moments (top). Scale bar is 1 nm. The OOP B-site displacement (δ_B) of the persistent state is mapped throughout the PTO|LSMO bilayer (bottom). Black symbols refer to LSMO, red and blue symbols refer to upwards and downwards polarization, respectively, in PTO. The error bars are the standard error of the mean. The electrostatic boundary conditions at the $La_{0.7}Sr_{0.3}O|TiO_2$-terminated LSMO|PTO interface result in the observed displacement discontinuity, see main text and ref. [16].

The observed absence of a critical thickness (i) has been previously reported for Pb-based ferroelectrics[16–19], and is further highlighted in Supplementary Note 2. The ISHG drop at the growth interruption (ii) is only observed for PTO films thinner than 40 u. c. (see Fig. 1b). The origin of the ISHG drop could be sample degradation, polarization suppression, or domain formation[4,20]. We therefore conduct a post-deposition STEM analysis by mapping the atomic displacements throughout the PTO film. The local manifestation of the polarization drop (ii) in the high-quality films is twofold, see Fig. 1c. First, dipole moments next to the top interface are reversed with respect to the direction set by the bottom interface, pointing downwards across 3–4 u. c. Second, beneath this region, the dipole moments retain the orientation set by the bottom interface, but their magnitude is suppressed, with PTO out-of-plane (OOP) B-site displacements of <5 pm compared to 16 pm in the bulk[21]. This points to the top interface favoring downwards polarization and therefore to a competition between bottom and top interfaces in setting the net polarization direction. This strikingly results in a substantial suppression of the polarization throughout the film.

We observe in Fig. 1b that the process responsible for the influence of the top interface on the polarization state occurs on a much longer time scale with respect to the growth process. As long as the growth continues, the polarization state is therefore essentially determined by a single interface, the bottom interface. An upwards polarization is established throughout the film during growth, resulting in the initially large ISHG signal. Once the growth is stopped, the top interface consolidates, and the combined influence of both interfaces determines the resulting polarization. Specifically, the top interface promotes downwards polarization. The strong suppression of the net polarization as described above is a response that neither interface alone would generate; it is a remarkable manifestation of a combined interface effect. The immediate restoration of the initial ISHG signal upon resuming growth indicates a return to the state dictated by the bottom interface only. Accordingly, we identify the transient regime during growth as the "single-interface-contribution" regime and the persistent regime once the growth is stopped as the "combined-interface-contribution" regime.

Having revealed that competitive interfaces lead to a pronounced decrease of polarization, we now scrutinize the possibility of a polarization enhancement by cooperative interfaces. We choose MnO_2-terminated LSMO as the buffer, thus promoting downwards polarization at the bottom interface[5], while keeping the same strain and growth conditions as in the competitive case. During PTO deposition, the ISHG signal now evolves as follows. (i) Following a delayed onset of polarization, further detailed in Supplementary Note 2, the ISHG yield increases steadily with thickness. (Note that the bump in the SHG net intensity is caused by interference with surface-induced background SHG.) (ii) A giant tenfold enhancement of ISHG intensity is observed upon growth interruption. (iii) As before, the transient ISHG intensity is restored with the continuation of the growth.

The tenfold enhancement is an impressive manifestation of the difference between the action of a single (bottom) interface and the joint action of both (top and bottom) interfaces in the transient and persistent regime, respectively. It only appears in PTO films thinner than 40 u. c., see Fig. 2b, which emphasizes the role of interface proximity. Furthermore, whereas in the case of a single effective interface, upwards polarization exhibits the larger SHG yield and, thus, dipole moment (Fig. 1), the cooperative action of two interfaces promoting downwards polarization overrules this preference (Fig. 2). We verified the giant cooperative polarization enhancement (ii) by STEM, finding a pervasive bulk-like OOP B-site displacement of about 16 pm (see Fig. 2c). The observed ISHG evolution (ii–iii) was verified on more than 40 samples, see Supplementary Note 3.

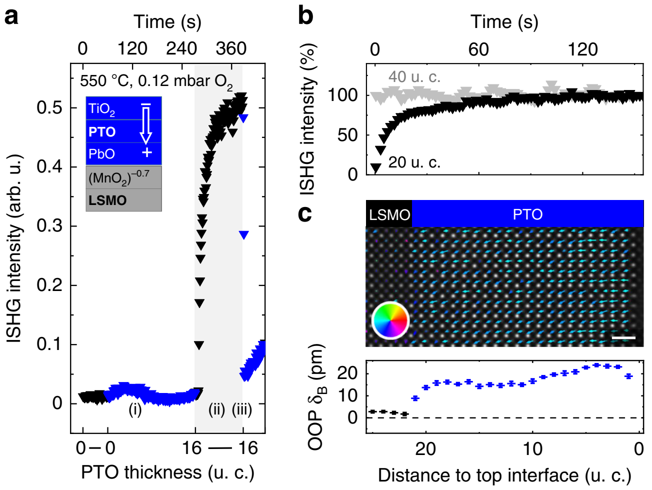

Fig. 2 Polarization enhancement from cooperative interfaces. a ISHG signal during ongoing (filled blue symbols, 0–16 u. c.) and halted (filled black symbols) growth. The inset shows the chemistries of interfacial planes at the PTO|LSMO interface and the polarization direction set by the bottom interface. **b** Time-dependent ISHG signal after interrupting deposition, normalized to the maximum value = 100. **c** Post-deposition STEM map of the dipole moments. The arrows show the direction (color wheel) and amplitude (arrow length) of the dipole moments (top). Scale bar is 1 nm. The OOP B-site displacement (δ_B) of the persistent state is mapped throughout the PTO|LSMO bilayer (bottom). Black symbols refer to LSMO, and blue symbols refer to downwards polarization in PTO. The error bars are the standard error of the mean.

We next pinpoint the mechanism promoting pervasive downwards polarization at the top interface. We rule out the intrinsic chemistry of the PTO termination as a possible explanation because, according to ab initio calculations[22], both the PbO and the TiO_2 top termination favor an upwards polarization. Our tests with other ferroelectric perovskites rather point to non-stoichiometry as the likely origin because the striking polarization evolution (ii–iii) was only observed for materials with A-site volatility, i.e., PTO, $Pb[Zr_xTi_{1-x}]O_3$ (PZT), and $BiFeO_3$ (BFO), in contrast to $BaTiO_3$ (BTO)[4] (see Supplementary Note 3). A-site volatility is usually compensated by A-site-excess targets in pulsed laser deposition (PLD) to recover the stoichiometry in the bulk of the films. It can, however, induce non-stoichiometry at the film surface. In line with this, a non-stoichiometric phase of Bi_2O_{3-x} at the surface has been shown to cause a local polarization change in BFO films[23,24]. Similarly, cationic vacancies were reported to affect the PTO polarization orientation[25]. Furthermore, the observed time for the reconstruction of polarization (ii) of about 10^2 s matches the theoretically derived value in response to ion migration[26]. Most importantly, the post-growth surface-sensitive angle-resolved XPS data shown in Fig. 3a and energy dispersive X-ray analysis reveal increasing Pb content toward the surface of our PTO films for both the competitive and the cooperative interfaces (see details in Supplementary Note 4). The non-stoichiometry of PTO toward the surface is likely in the form of Pb adatoms. We note that other sources of non-stoichiometry such as Pb substitution of Ti atoms were not detected. In summary, we conclude that the Pb-rich top layer results in a positively charged top interface where it promotes a downwards polarization.

We use density functional theory (DFT) to verify that non-stoichiometry at the top interface determines the net polarization of the film in the persistent regime. We simulate the non-stoichiometry by introducing a Pb adatom at the top interface of a stoichiometric lattice of PTO[27–29]. We fix the direction of the dipole moment in the film at the bottom interface to either up or down to match with our experiments and allow the ions in the rest of the film to relax. Our calculations reveal that for an up-polarized bottom interface the resulting positive bound charge at the top interface is disfavored by the Pb adatom. In response, see Fig. 3b, the dipole moment is suppressed throughout the layer and reversed in the topmost u. c. to reduce the total energy of the film. In contrast, for a down-polarized bottom interface, the associated negative bound charge at the top interface is compensated by the positive charge of the bound Pb adatom (Fig. 3c). This results in a stabilization of the ferroelectric polarization, which remains bulk-like throughout the film.

We thus arrive at the following scenario for the growth dynamics of our PTO films. During growth (transient regime in Fig. 3d, e), epitaxial stabilization[30] promotes stoichiometry in the PTO films. The film polarization follows the state set at the bottom interface by the respective LSMO termination. Once the growth is stopped, the excess Pb from the Pb-rich target material (see "Methods") diffuses toward the film surface, which results in accumulation of positive charges at the top interface. In response, the polarization of the film is suppressed or enhanced (persistent regime in Fig. 3d, e).

We then investigate how the interface-induced polarization suppression and enhancement affect the electric-field poling of the PTO films. The results of the time-dependent switching behavior are shown in Fig. 4. In both interface configurations, the polarization can be locally reversed by the voltage applied to a

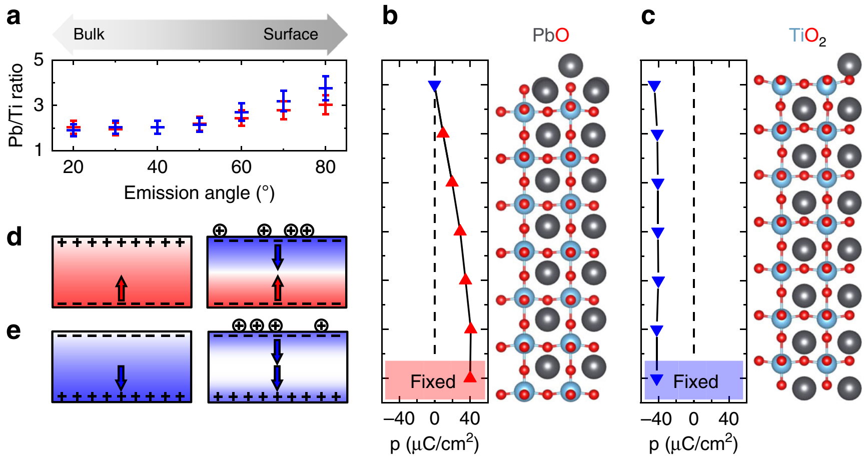

Fig. 3 Competitive and cooperative configurations explored by XPS and DFT. a Pb/Ti atomic ratio at XPS emission angles (20–80)°, higher angles displaying a higher sensitivity to the sample surface lower angles. Red and blue symbols correspond to the samples with suppressed and enhanced polarization, respectively. The error bar is based on the estimated experimental accuracy (see "Methods"). **b**, **c** Density-functional calculations of dipole moments (p) perpendicular to the bottom interface in PTO heterostructures with a Pb adatom on the surface. The polarization direction is imposed at the bottom interface to match with our experiments by fixing the dipole moment of the first u. c. in the calculation (marked as "fixed"). The atomic positions in heterostructures with (**b**) PbO and (**c**) TiO_2 top-interface termination and their ionic positions are depicted on the right-hand side of the graph. **d**, **e** Sketch of the competitive and cooperative interfaces for the transient (left) "single-interface" and the persistent (right) "combined-interface" regime. The favored polarization direction at each interface is indicated with arrows and the resulting bound charges are represented with "+" and "–" signs. The additional positive charges at the top interface introduced to emulate the non-stoichiometry are shown as "⊕".

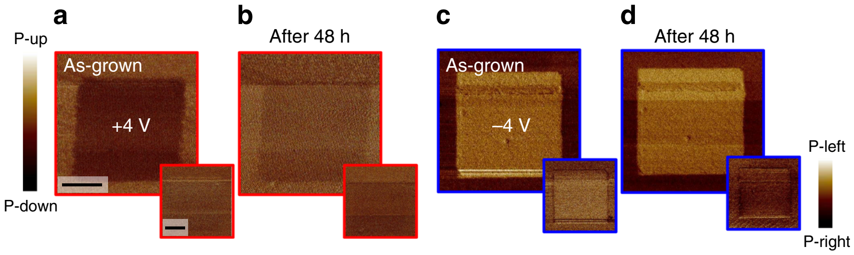

Fig. 4 Stability of the electric-field-induced polarization switch over time. a–**d** PFM out-of-plane (in-phase, main panel) and in-plane (quadrature, inset) data immediately after the poling (±4 V) and 48 h later for **a**, **b** competitive and **c**, **d** cooperative interface configurations. PTO films are 20 u. c. thick and scale bars are 1 μm.

piezoresponse-force-microscopy (PFM) tip. In the PTO films with competitive interfaces, the electric-field-induced downwards polarization vanishes after 48 h (see Fig. 4a, b). In contrast, in the PTO films with cooperative interfaces, a stable upwards polarization is sustained over the same time period (see Fig. 4c, d). This correlates with our ISHG and STEM data, indicating a robust ferroelectric response when cooperative interfaces are at work.

Finally, we test the robustness of the competitive and the cooperative polarization state by capping the PTO films with 18 u. c. of STO. STO isolates PTO from the charge-screening oxygen-rich growth atmosphere and thus enhances the depolarizing field, promoting a multidomain breakdown[4,31]. For the suppressed polarization state, this breakdown is indeed observed, as confirmed macroscopically and microscopically by the SHG and STEM measurements in Fig. 5a, c. For the enhanced polarization state, however, the single-domain state is retained, as seen in Fig. 5b, d, e. Although one might assume the state with the higher net polarization to be more prone to energy minimization through multidomain breakdown, it is, in fact, more robust against STO capping.

A possible explanation for this striking behavior is provided by the STEM data in Fig. 5d. We find a sharp dipole-moment discontinuity across the epitaxial PTO|STO interface, which is revealed by the absence of B-site displacements in the STO layer despite the bulk-like B-site displacements in the PTO layer. We conclude that the remnant positive charges from non-stoichiometry at the PTO top-interface efficiently screen the negative bound charges of the enhanced polarization state at the PTO|STO interface, hence preventing multidomain breakdown. In the case of the suppressed polarization state, on the other hand, the positive charges induced by the non-stoichiometry cannot screen the positive bound charges associated with the oppositely oriented polarization, and multidomain breakdown occurs (see Supplementary Note 4).

Discussion

Hence we have shown how, in the ultrathin regime, the proximity and combined influence of both interfaces in a thin epitaxial oxide film determine its properties. We demonstrate drastic differences between competitive and cooperative interface configurations and to the action of a single interface. Specifically, in ferroelectric PTO, cooperative interfaces stabilize a bulk polarization state down to the ultrathin regime of about 10 u. c. and protect it against depolarizing-field-induced multidomain breakdown. Selective access to the interfaces and their correlation is enabled by a unique combination of ISHG, STEM, and XPS measurements. We expect our findings to be relevant for nanoscale oxide thin films in which interfacial chemistry and charge imbalance at large are important, beyond the

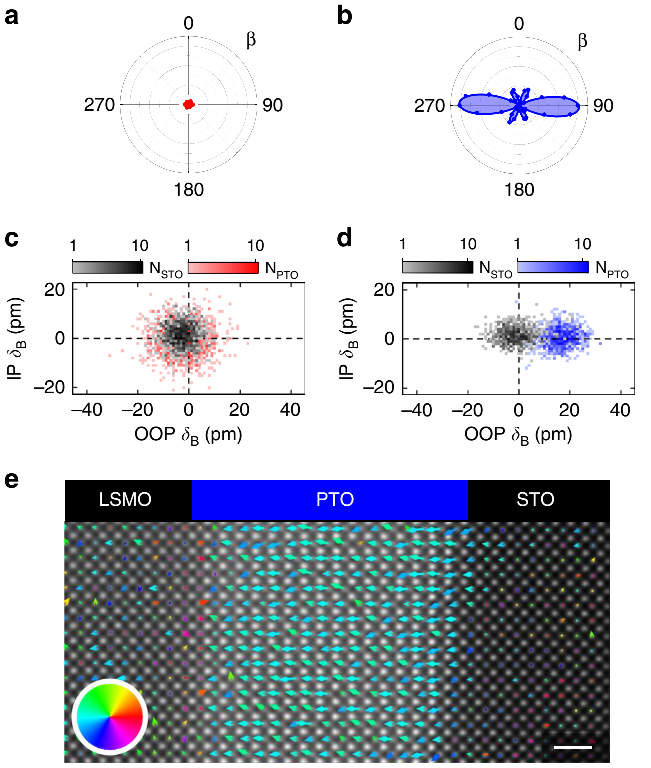

Fig. 5 Stability of net polarization in a STO|PTO heterostructure. **a**, **b** SHG anisotropy plots of STO|PTO bilayers after cooling to room temperature, shown on the same intensity scale. Data were obtained by simultaneously varying the angle β of the polarization of the incident fundamental and of the detected SHG light at 1200 and 600 nm, respectively. The simulations, see "Methods," are plotted as continuous lines. Note that for the competitive interfaces (**a**), a measurable signal is not detected. **c**, **d** Logarithmic histogram plots showing the number of occurrences N_{STO} (black) and N_{PTO} of OOP and in-plane (IP) B-site displacement (δ_B) measured in post-deposition STEM images for the (**c**) competitive (red) and the (**d**) cooperative (blue) interface configuration. The zero net value of B-site displacement in the OOP direction of the competitive case in the multidomain state is the result of polarization averaging across the thickness of the lamella. **e** Post-deposition STEM map of PTO dipole moments after STO capping in the cooperative configuration. The arrows show the direction (color wheel) and amplitude (arrow length) of the dipole moments. Scale bar is 1 nm.

specific A-site volatile proper ferroelectrics investigated here. Bi-interfacial control of ultrathin films can thus become a key factor in bypassing present limitations of oxide-electronic functionalities and devices[32,33].

Methods

Thin-film deposition. The thin films and heterostructures were grown on TiO_2-terminated STO (001) substrates by PLD using a KrF excimer laser at 248 nm. The fluence of the laser, its repetition rate, substrate temperature, and growth pressure for individual layers were as follows: $SrRuO_3$ (SRO): 0.9 Jcm^{-2}, 2 Hz, 700 °C, 0.1 mbar O_2; LSMO: 0.9 Jcm^{-2}, 1 Hz, 700 °C, 0.15 mbar O_2; PTO: 1.15 Jcm^{-2}, 4 Hz, 550 °C, 0.12 mbar O_2; and STO: 1.15 Jcm^{-2}, 2 Hz, 550 °C, 0.12 mbar O_2. The PTO target was Pb-enriched ($Pb_{1.2}TiO_3$) and the other targets were stoichiometric. The thickness of the thin films was monitored using RHEED during growth. The thin-film topography and PFM were performed using a Bruker Multimode 8 atomic force microscope.

In situ second harmonic generation (ISHG). The incident light was generated from a Ti:Sapphire laser light with a pulse duration of 45 fs, a repetition rate of 1 kHz, and a wavelength of 800 nm, which was converted using an optical parametric amplifier to light with a wavelength of 1200 nm. This incident beam was focused onto the sample in the thin-film growth environment in reflection at 45° with a pulse energy of 30 µJ and a spot size 250 µm in diameter. The optical SHG signal was generated at 600 nm and detected using a monochromator and a photomultiplier system.

Analysis of SHG signal. The SHG process is expressed by the equation $P_i(2\omega) = \epsilon_0\chi^{(2)}_{ijk}E_j(\omega)E_k(\omega)$, where $E_{j,k}(\omega)$ and $P_i(2\omega)$ are the electric-field components of the incident light and of the frequency-doubled polarization, respectively. The point-group symmetry of a compound determines the set of its tensor components $\chi^{(2)}_{ijk} \neq 0$. The anisotropy simulations of the tetragonal $4mm$ group were consistent with the SHG data when the components $\chi^{(2)}_{xzx}$, $\chi^{(2)}_{zxx}$, and $\chi^{(2)}_{zzz}$ were fitted as nonzero.

Scanning transmission electron microscopy (STEM). Cross-sectional specimens for the STEM analysis were prepared by mechanical polishing using a tripod polisher followed by argon ion milling using a Fishione ion miller model 1050 operated at 3 kV until electron transparency. A FEI Titan Themis equipped with a probe CEOS DCOR spherical aberration corrector and ChemiSTEM technology operated at 300 kV was used for HAADF-STEM imaging and EDX spectroscopy. The atomic-resolution HAADF-STEM images were acquired setting a probe semi-convergence angle of 25 mrad in combination with an annular semi-detection range of the annular dark-field detector of 66–200 mrad. To correct for the scan distortions, time series consisting of 10 frames (2048 × 2048 pixels) were acquired and averaged by rigid and nonrigid registration by means of the Smart Align software[34]. A Gaussian filter was applied, followed by a custom-developed Python code for blind probe deconvolution assuming a Gaussian distribution as the initial probe to reduce the spread of the atomic columns. Subsequently, fitting of the atomic columns was performed using the Python library Atomap[35] and the local dipole moment was calculated by measuring the polar displacement of the B position in the image plane from the center of mass of its four nearest A neighbors. The dipole moment is plotted in the HAADF-STEM images opposite to the B-site displacement (δ_B).

X-ray photoelectron spectroscopy (XPS). X-ray photoelectron spectra were acquired using a PHI Quantera^{SXM} (ULVAC-PHI, Chanhassen, MN, U.S.A.) spectrometer. The films were mounted on standard PHI platen and analyzed using a monochromatic Al K_α source ($h\nu = 1486.6$ eV at 24.5 W); the beam diameter was of 100 µm. The analyzer was operated in the fixed analyzer transmission mode. A pass energy of 69 eV and a step size of 0.125 eV were used to obtain the high-resolution spectra of C 1*s*, O 1*s*, Ti 2*p*, and Pb 4*f*. The linearity of the energy scale was checked according to ISO15472: 2010 (confirmed in 2015) and the accuracy of the binding-energy value for each element was found to be 0.1 eV. The binding energies were referred to adventitious aliphatic carbon signal taken at 285.0 eV. The angle-resolved spectra were acquired using the special sample holder designed by ULVAC-PHI for these measurements, and the calibration for the eucentric tilt was carried out before each spectral acquisition so that the spectra were collected on the samples by maintaining the analysis area always on the focal point of the x-ray source and of the analyzer at all emission angles. The estimated experimental accuracy of 10% is primarily a result of: signal-to-noise ratio, peak intensity, accuracy of relative sensitivity factors, and correction for electron transmission function. During the analysis, the residual pressure in the main chamber was measured to be around 10^{-7} Pa. The spectra were processed using CASAXPS software (version 2.3.15, Casa Software Ltd.).

Ab initio calculations. DFT calculations of PTO thin films, both without buffer and on LSMO were carried out with VASP[36] using the PBEsol[37] functional, which gives a good metal/insulator band alignment at the interface, with the Fermi level of the metal falling within the PTO gap[38]. The alloying in LSMO was simulated using the virtual crystal approximation[39,40]. Core electrons were replaced by projector augmented wave potentials[41], and the valence states were expanded in plane waves with a cutoff energy of 500 eV. A Monkhorst-Pack grid of 3 × 3 × 1 *k*-points was used for all thin films with a surface area of 2 × 2 u. c. A 14-layer-thick (1 × 1) PTO (001) slab, consisting of 7 u. c. was found to be sufficient to converge the surface energy. The in-plane and out-of-plane lattice parameters were set to those of the STO substrate ($a = 3.905$ Å) and the PTO bulk value ($c = 4.11$ Å), respectively. In all cases, the atoms of the four bottom layers of the PTO were fixed to the calculated bulk values, while the rest of the system was allowed to relax.

Data availability

The data that support the findings of this study are available from the corresponding authors upon request.

Received: 18 June 2020; Accepted: 25 October 2020;
Published online: 16 November 2020

References

1. Zubko, P. et al. Electrostatic coupling and local structural distortions at interfaces in ferroelectric/paraelectric superlattices. *Nano Lett.* **12**, 2846–2851 (2012).
2. Lichtensteiger, C., Fernandez-Pena, S., Weymann, C., Zubko, P. & Triscone, J. M. Tuning of the depolarization field and nanodomain structure in ferroelectric thin films. *Nano Lett.* **14**, 4205–4211 (2014).
3. Liu, G. et al. Positive effect of an internal depolarization field in ultrathin epitaxial ferroelectric films. *Adv. Electron. Mater.* **2**, 1500288 (2016).
4. Strkalj, N. et al. Depolarizing field effects in epitaxial capacitor heterostructures. *Phys. Rev. Lett.* **123**, 147601 (2019).
5. Yu, P. et al. Interface control of bulk ferroelectric polarization. *PNAS* **109**, 9710–9715 (2012).
6. Wang, R. V. et al. Reversible chemical switching of a ferroelectric film. *Phys. Rev. Lett.* **102**, 047601 (2009).
7. Highland, M. J. et al. Equilibrium polarization of ultrathin $PbTiO_3$ with surface compensation controlled by oxygen partial pressure. *Phys. Rev. Lett.* **107**, 187602 (2011).
8. Shin, J. et al. Atomistic screening mechanism of ferroelectric surfaces: an in situ study of the polar phase in ultrathin $BaTiO_3$ films exposed to H_2O. *Nano Lett.* **9**, 3720–3725 (2009).
9. Tian, Y. et al. Water printing of ferroelectric polarization. *Nat. Commun.* **9**, 3809 (2018).
10. Domingo, N. et al. Surface charged species and electrochemistry of ferroelectric thin films. *Nanoscale* **11**, 17920–17930 (2019).
11. Bein, B. et al. In situ X-ray diffraction and the evolution of polarization during the growth of ferroelectric superlattices. *Nat. Commun.* **6**, 10136 (2015).
12. Strkalj, N., Gradauskaite, E., Nordlander, J. & Trassin, M. Design and manipulation of ferroic domains in complex oxide heterostructures. *Materials* **12**, 3108 (2019).
13. De Luca, G. et al. Nanoscale design of polarization in ultrathin ferroelectric heterostructures. *Nat. Commun.* **8**, 1419 (2017).
14. Nordlander, J., De Luca, G., Strkalj, N., Fiebig, M. & Trassin, M. Probing ferroic states in oxide thin films using optical second harmonic generation. *Appl. Sci.* **8**, 570 (2018).
15. Denev, S. A., Lummen, T. T. A., Barnes, E., Kumar, A. & Gopalan, V. Probing ferroelectrics using optical second harmonic generation. *J. Am. Ceram. Soc.* **94**, 2699–2727 (2011).
16. Stengel, M., Vanderbilt, D. & Spaldin, N. A. Enhancement of ferroelectricity at metal-oxide interfaces. *Nat. Mater.* **8**, 392–397 (2009).
17. Sai, N., Kolpak, A. M. & Rappe, A. M. Ferroelectricity in ultrathin perovskite films. *Phys. Rev. B* **72**, 020101 (2005).
18. Fong, D. D. et al. Stabilization of monodomain polarization in ultrathin $PbTiO_3$ films. *Phys. Rev. Lett.* **96**, 127601 (2006).
19. Gao, P. et al. Possible absence of critical thickness and size effect in ultrathin perovskite ferroelectric films. *Nat. Commun.* **8**, 15549 (2017).
20. Duan, C.-G., Sabirianov, R. F., Mei, W.-N., Jaswal, S. S. & Tsymbal, E. Y. Interface effect on ferroelectricity at the nanoscale. *Nano Lett.* **6**, 483–487 (2006).
21. Glazer, A. M. & Mabud, S. A. Powder profile refinement of lead zirconate titanate at several temperatures. II. Pure $PbTiO_3$. *Acta Cryst.* **B34**, 1065–1070 (1978).
22. Gattinoni, C. et al. Interface and surface stabilization of the polarization in ferroelectric thin films. *PNAS* 202007736 https://doi.org/10.1073/pnas.2007736117 (2020).
23. Xie, L. et al. Giant ferroelectric polarization in ultrathin ferroelectrics via boundary-condition engineering. *Adv. Mater.* **29**, 1701475 (2017).
24. Béa, H. et al. Influence of parasitic phases on the properties of $BiFeO_3$ epitaxial thin films. *Appl. Phys. Lett.* **87**, 072508 (2005).
25. Weymann, C. et al. Full control of polarization in ferroelectric thin films using growth temperature to modulate defects. *Adv. Electron. Mater.* 2000852 https://doi.org/10.1002/aelm.202000852 (2020).
26. Vorotiahin, I. S., Morozovska, A. N. & Genenko, Y. A. Hierarchy of domain reconstruction processes due to charged defect migration in acceptor doped ferroelectrics. *Acta Materialia* **184**, 267–283 (2020).
27. Stephenson, G. B. & Highland, M. J. Equilibrium and stability of polarization in ultrathin ferroelectric films with ionic surface compensation. *Phys. Rev. B* **84**, 064107 (2011).
28. Fechner, M., Ostanin, S. & Mertig, I. Effect of the surface polarization in polar perovskites studied from first principles. *Phys. Rev. B* **77**, 094112 (2008).
29. Garrity, K., Kakekhani, A., Kolpak, A. & Ismail-Beigi, S. Ferroelectric surface chemistry: first-principles study of the $PbTiO_3$ surface. *Phys. Rev. B* **88**, 045401 (2013).
30. Gorbenko, O. Y., Samoilenkov, S. V., Graboy, I. E. & Kaul, A. R. Epitaxial stabilization of oxides in thin films. *Chem. Mater.* **14**, 4026–4043 (2002).
31. Das, S. et al. Observation of room-temperature polar skyrmions. *Nature* **568**, 368–372 (2019).
32. Martin, L. W. & Rappe, A. M. Thin-film ferroelectric materials and their applications. *Nat. Rev. Mater.* **2**, 16087 (2016).
33. Li, L. et al. Observation of strong polarization enhancement in ferroelectric tunnel junctions. *Nano Lett.* **19**, 6812–6818 (2019).
34. Jones, L. et al. Smart align—a new tool for robust non-rigid registration of scanning microscope data. *Adv. Struct. Chem. Imaging* **1**, 8 (2015).
35. Nord, M., Vullum, P. E., MacLaren, I., Tybell, T. & Holmestad, R. Atomap: a new software tool for the automated analysis of atomic resolution images using two-dimensional Gaussian fitting. *Adv. Struct. Chem. Imaging* **3**, 9 (2017).
36. Kresse, G. & Hafner, J. *Ab initio* molecular dynamics for liquid metals. *Phys. Rev. B* **47**, 558–561 (1993).
37. Perdew, J. P. et al. Restoring the density-gradient expansion for exchange in solids and surfaces. *Phys. Rev. Lett.* **100**, 136406 (2008).
38. Stengel, M., Aguado-Puente, P., Spaldin, N. A. & Junquera, J. Band alignment at metal/ferroelectric interfaces: Insights and artifacts from first principles. *Phys. Rev. B* **83**, 235112 (2011).
39. Nordheim, L. Zur elektronentheorie der metalle. I. *Ann. Phys.* **401**, 607–640 (1931).
40. Muto, T. On the electronic structure of alloys. *Sci. Pap. Inst. Phys. Chem. Res.* **34**, 377 (1938).
41. Kresse, G. & Joubert, D. From ultrasoft pseudopotentials to the projector augmented-wave method. *Phys. Rev. B* **59**, 1758–1775 (1999).

Acknowledgements

M.T. acknowledges the Swiss National Science Foundation under Project No. 200021-188414. N.S., M.T. and M.F. acknowledge support by the EU European Research Council under Advanced Grant Program No. 694955-INSEETO. M.F. acknowledges support by the Swiss National Science Foundation under Project No. 200021-178825. N.S. and M.T. thank Gabriele De Luca for fruitful discussions and Elzbieta Gradauskaite and Martin Sarott for experimental assistance. C.G. is supported by the European Union's Horizon 2020 research and innovation programme under the Marie Skłodowska-Curie Grant Agreement No. 744027. C.G.'s computational work was supported by a grant from the Swiss National Supercomputing Centre (CSCS) under project ID s870. N.S., C.G., A.R., N.A.S., M.F., and M.T. acknowledge support from ETH Zurich. A.V., M.C., and M.D.R. acknowledge support by the Swiss National Science Foundation under Project No. 200021-175926. A.R. thanks technical support from Giovanni Cossu.

Author contributions

All authors discussed the results. N.S., M.T., and M.F. wrote the manuscript. N.S. performed the thin-film growth, PFM, ISHG measurements and structural analysis. C.G., R.H., and N.A.S. performed the DFT calculations. A.V., M.C. and M.D.R. carried out the STEM investigations. A.R. supervised, processed, and interpreted the XPS data. M.T. designed the experiment and supervised the work jointly with M.F.

Competing interests

The authors declare no competing interests.

Additional information

Supplementary information is available for this paper at https://doi.org/10.1038/s41467-020-19635-7.

Correspondence and requests for materials should be addressed to N.S. or M.T.

Peer review information *Nature Communications* thanks the anonymous reviewer(s) for their contribution to the peer review of this work. Peer reviewer reports are available.

Reprints and permission information is available at http://www.nature.com/reprints

Publisher's note Springer Nature remains neutral with regard to jurisdictional claims in published maps and institutional affiliations.

Open Access This article is licensed under a Creative Commons Attribution 4.0 International License, which permits use, sharing, adaptation, distribution and reproduction in any medium or format, as long as you give appropriate credit to the original author(s) and the source, provide a link to the Creative Commons license, and indicate if changes were made. The images or other third party material in this article are included in the article's Creative Commons license, unless indicated otherwise in a credit line to the material. If material is not included in the article's Creative Commons license and your intended use is not permitted by statutory regulation or exceeds the permitted use, you will need to obtain permission directly from the copyright holder. To view a copy of this license, visit http://creativecommons.org/licenses/by/4.0/.

© The Author(s) 2020

Optical second harmonic signature of phase coexistence in ferroelectric|dielectric heterostructures

C

Preprint: N. Strkalj, A. Bortis, M. Campanini, M. D. Rossell, M. Fiebig, and M. Trassin. “Optical second harmonic signature of phase coexistence in ferroelectric|dielectric heterostructures’, *in preparation* (2021).

Optical second harmonic signature of phase coexistence in ferroelectric|dielectric heterostructures

Nives Strkalj[1],* Amadé Bortis[1], Marco Campanini[2],
Marta D. Rossell[2], Manfred Fiebig[1], and Morgan Trassin[1]
[1] *Department of Materials, ETH Zurich, 8093 Zurich, Switzerland*
[2] *Electron Microscopy Center, Swiss Federal Laboratories for Materials Science and Technology, Empa, Dübendorf, 8600, Switzerland*

(Dated: August 12, 2021)

An exotic coexistence of polar states is known to occur in ferroelectric|dielectric $PbTiO_3|SrTiO_3$ (PTO|STO) heterostructures. In the PTO layers with a thickness of 10–20 unit cells, in-plane-polarized regions order alongside the so-called vortex phase with a whirl-like arrangement of electric dipoles. We investigate the optical signature of these polar phases non-invasively using optical second harmonic generation (SHG) in PTO|STO-based heterostructures. We identify the phase coexistence down to a single PTO|STO bilayer. By comparing the SHG yield in dependence of the number of PTO|STO bilayers, we further find that interlayer coupling plays an important role in setting the final polarization state. Our non-linear optical experiments demonstrate the potential of this non-invasive approach for the identification and understanding of complex non-collinear ordering of dipole moments in oxide heterostructures and set the ground for their operando investigation.

I. INTRODUCTION

Complex polar phases consisting of nanoscale arrays of electric dipole moments that exhibit continuous spatial change of orientation were recently observed in ferroelectric|dielectric PTO|STO heterostructures [1–15]. In these complex polar phases, local negative capacitance was measured, which is considered to be a powerful ingredient in new transistor technology. Ferroelectric|dielectric heterostructures are thus becoming a promising platform for new oxide-electronic applications [16–20]. Current investigations on the PTO|STO system involve scanning transmission electron microscopy (STEM) in combination with x-ray diffraction (XRD) or piezoresponse force microscopy (PFM), which both require a superlattice architecture in order to increase the sample volume so that signals become measurable. However, the difficulty to identify non-collinear ordering of dipole moments non-invasively and in technologically relevant single layers prevents a deeper understanding of the formation of complex phases in these and also their integration into devices.

Here we show that SHG is an ideal tool for non-invasive access to the complex arrangement of dipole moments in PTO|STO heterostructures. Our symmetry analysis of the SHG polarimetry in a PTO|STO superlattice and a PTO|STO bilayer reveals the presence of distinct SHG contributions from two polar phases. We specifically identify the phase coexistence of a ferroelectric in-plane polarized multi-domain phase and a polar vortex-like phase. Furthermore,

---

* nives.strkalj@mat.ethz.ch

an oscillatory evolution of the SHG yield with the number of deposited PTO and STO constituent layers points to a previously overlooked extended phase- and inverted domain-coupling effect between the PTO layers that attenuates the net in-plane polarization. Ultimately, our non-invasive approach expedites the search for complex polar phases and the study of their time-dependent operando response to electric fields.

II. RESULTS

A. Characterization of ordering of dipole moments in the PTO|STO superlattice

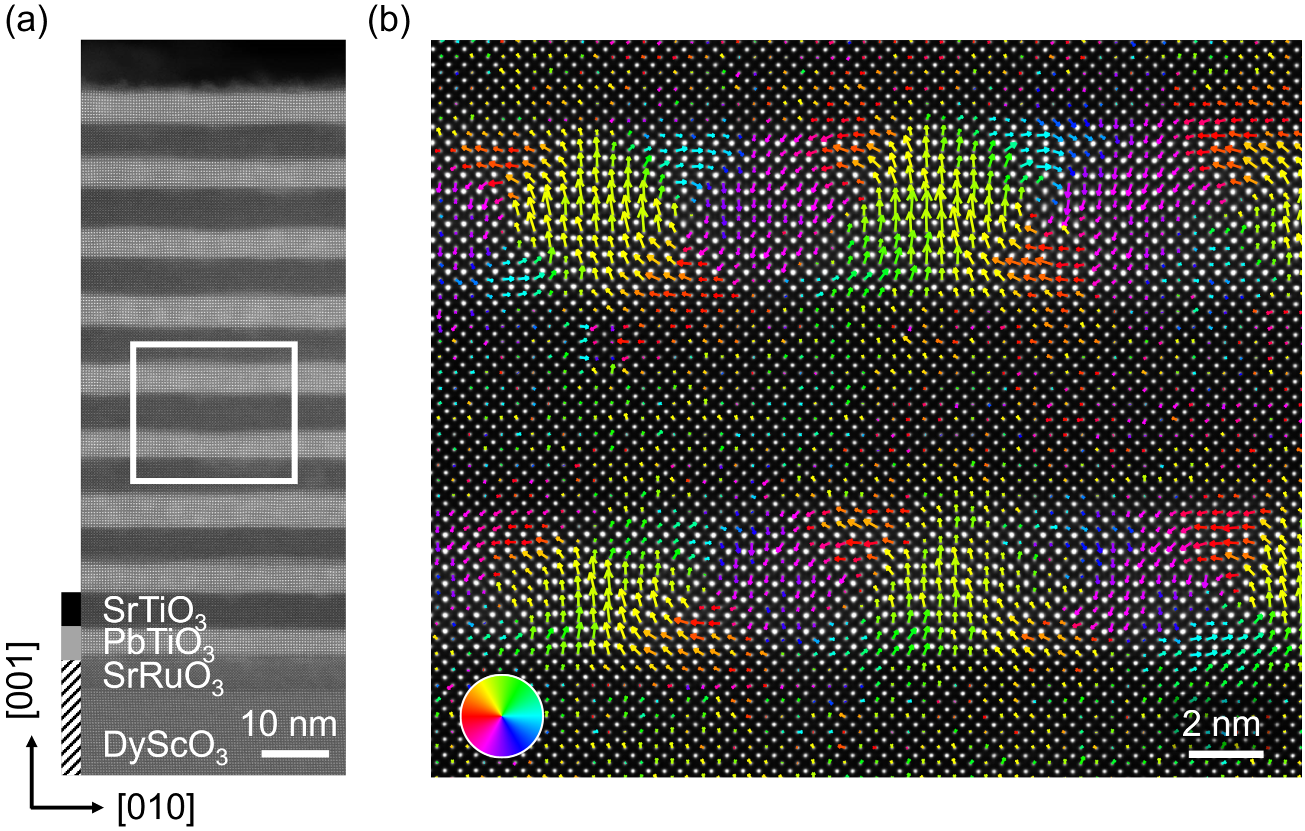

FIG. 1. (a) STEM map of atomic positions in a PTO|STO (grey|black) superlattice on the $SrRuO_3$-buffered (110)-oriented $DyScO_3$ substrate (hatching). (b) Post-deposition STEM map of the dipole moments in the area outlined in white in (a), respectively. The arrows show the direction (color wheel) and amplitude (arrow length) of the dipole moment.

We grew our $(PTO_{12}|STO_{12})_8PTO_{12}$ superlattice on a $SrRuO_3$-buffered (110)-oriented orthorhombic $DyScO_3$ substrate using pulsed laser deposition. Details of the growth are reported in Supplementary Section 1, and crystallographic directions henceforth refer to the pseudocubic axes of the $DyScO_3$ substrate. This particular type of PTO|STO superlattice has been shown to host a phase coexistence of (i) a so-called a_1/a_2-phase and (ii) a vortex phase [5, 9]. (i) In the a_1/a_2-phase, domains with a polarization along [100] or [010], termed a_1- and a_2-domains, respectively, arrange in alternating stripes. (ii) In the vortex phase, long-range ordered arrays of electric-dipole vortex structures [21] extend in a tubular way along [100]. In addition to the vortex-like arrangement of dipole moments around the vortex core, the resulting tubuli exhibit a net polarization along their central axis, in the [100] direction.

We first confirm the phase coexistence of the a_1/a_2-phase and the vortex phase in our superlattice using a combination of PFM (see Supplementary Fig. 2) and STEM. We specifically verify the presence of the vortex phase by cross-sectional STEM imaging, see Fig. 1(a,b). We map the spatial distribution of the electric dipole moments within the superlattice in the plane perpendicular to the tubular axes of the vortices. We find the expected signature of the vortex phase, that is, a non-collinear arrangement of dipole moments into a circle around the vortex core with alternating vorticity in neighboring whirls [3].

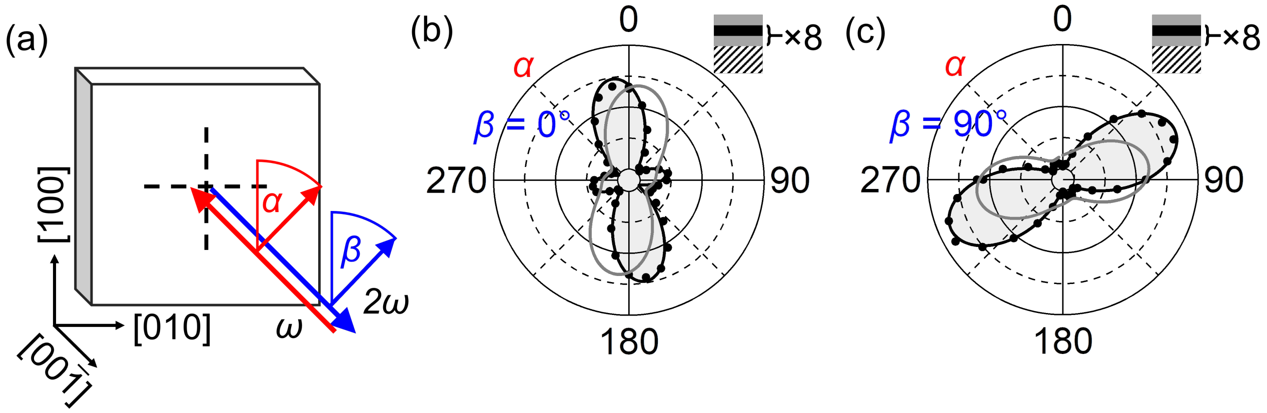

FIG. 2. (a) Schematic of the SHG setup in the employed normal-incidence geometry. Crystallographic directions refer to the pseudocubic axes of the DyScO$_3$ substrate. The incoming light propagates along [001] at 1.033 eV with a linear polarization set to the angle α. The generated non-linear signal at 2.066 eV is analyzed in its polarization state using an analyzer fixed to the angle $\beta = 0°$. (b,c) Polar plots of SHG intensity (points) versus incident-light polarization angle α for a PTO|STO superlattice with (b) $\beta = 0°$ and (c) $\beta = 90°$. Grey lines are theoretical fits of the one-phase model based on Eq. 3, and black lines are theoretical fits of the two-phase model based on Eq. 6. Schematic of the multilayer is given in the inset top right. Grey denotes PTO, black denotes STO, and hatching denotes the SrRuO$_3$-buffered DyScO$_3$ substrate. The intensity scale is equal in (b) and (c).

Let us now move on to the optical characterization of the polar phases in this PTO|STO superlattice by SHG. SHG denotes frequency doubling of a light wave in a material, a process that in its leading order is permitted in the absence of inversion symmetry. This makes SHG an efficient tool for the investigation of ferroelectricity, at sample thicknesses down to a single unit cell [22–35]. SHG can only access the inversion-symmetry breaking in the plane perpendicular to the wave vector of the propagating light. We can therefore selectively access the in-plane polarization of our heterostructures by choosing a normal-incidence geometry [35, 36] as depicted in Fig. 2(a). We use a spot size of 250 µm so that it averages across about a hundred regions in either the a_1/a_2-phase or the vortex phase, see Supplementary Fig. 2, and represents an appropriate statistical mix of coexisting phases. The polarization of the incoming light is rotated by an angle α ranging from 0° to 360°, and the outgoing light is detected at a fixed polarization, that is, $\beta = 0°$ and $\beta = 90°$ with respect to [100] in the SHG polarimetry in Fig. 2(b) and Fig. 2(c), respectively.

We observe a pronounced SHG signal indicating a non-zero in-plane net polarization. Extracting the details of the polar order in our superlattice from the SHG polarimetry data is difficult because of the coexistence of two different polar phases. These phases are expected to have a different spectral dependence of the SHG-light. Furthermore, the SHG responses of the a_1/a_2-phase and the vortex phase interfere in an undetermined way. This complexity manifests itself, for example, in the polarization angle of the incoming light at which we observe maximum SHG yield, see Fig. 2(b,c). In contrast to simpler one-phase systems [29, 30, 36, 37], this direction does not coincide with the direction of the spontaneous net polarization. To evaluate the polar configuration of our system from the SHG polarimetry, it is therefore necessary to model the SHG response in greater detail than before.

B. Modelling of the SHG response of PTO|STO heterostructures

To model our polarimetry results, we consider the general expression for the leading-order SHG contribution

$$P_i^{(2)}(2\omega) = \epsilon_0 \chi_{ijk}^{(2)} E_j(\omega) E_k(\omega), \tag{1}$$

where $E(\omega)$ is the incoming light field, $P^{(2)}(2\omega)$ is the nonlinear polarization induced in the material, and the tensor $\hat{\chi}^{(2)}$ is linked to the point-group symmetry of the crystal. The indices i, j, and k refer to the crystallographic axes of the local coordinate system of a unit cell.

The $4mm$ point-group symmetry describes both the a_1/a_2-phase and the net axial polarization of the vortex phase in tetragonal PTO. The unit cell is set by the local coordinate system x, y, and z, where z is the fourfold axis and also the local direction of the spontaneous polarization. In the $4mm$ point-group symmetry, only the tensor components $\chi_{zxx} = \chi_{zyy}$, χ_{zzz} and $\chi_{xzx} = \chi_{yzy}$ can be non-zero [38]. We measure the angular dependence of the SHG intensity in a global coordinate system of the substrate, as defined by the axes [100], [010] and [001] introduced in Fig. 2(a). We relate the SHG contributions described in the local coordinate system of the unit cell to the global coordinate system of the sample by projecting them along the directions given by the angles α and β.

Previously, modelling of the SHG response was conducted only for heterostructures with a single ferroelectric phase [29, 30, 36, 37]. In addition to the standard a_1/a_2-phase, our sample hosts a vortex phase. We consider two models to describe our SHG polarimetry results: (1) a *one-phase model* that considers only the SHG response of the a_1/a_2-phase and (2) a *two-phase model* that considers the independent and interfering SHG responses of the a_1/a_2-phase and the vortex phase. We compare the fits of these two models in Fig. 2 and Fig. 3 to answer to what extent: (a) the one-phase model can emulate the SHG response of phase coexistence, and (b) the two-phase model can appropriately describe the SHG polarimetry measurements.

In our models, we consider only the SHG response of in-plane projections of local polarization because of the normal-incidence geometry of our measurements. We further assume destructive interference of SHG responses of oppositely oriented polarization within either phase because of the phase difference of 180°[39]. Because of the large number of parameters the models were fitted to the SHG polarimetry results with a Monte-Carlo-based approach. Specifically, we used a dual-annealing algorithm as implemented in SciPy's optimization library [40].

1. *One-phase model*

In the one-phase model of the SHG response of the a_1/a_2-phase, the SHG contributions for a local spontaneous polarization along [100] and [010] have equal spectral dependence of the $\hat{\chi}^{(2)}$ tensor components. We describe the fractions of the regions with local polarization pointing towards [100], [$\bar{1}$00], [010] and [0$\bar{1}$0] with parameters A_1^+, A_1^-, A_2^+ and A_2^-, respectively. We express the relative fractions of SHG signals originating from the a_1-domains as A_1, and from the a_2-domains as A_2:

$$A_1 = \frac{A_1^+ - A_1^-}{(A_1^+ - A_1^-) + (A_2^+ - A_2^-)}, \quad A_2 = \frac{A_2^+ - A_2^-}{(A_1^+ - A_1^-) + (A_2^+ - A_2^-)}, \tag{2}$$

where $A_1 + A_2 = 1$. The SHG intensity as a function of α and β angles can then be expressed as:

$$\begin{aligned} I^{2\omega}(\alpha,\beta) = |A_1&[-(\chi_{zxx}\cos^2\alpha + \chi_{zzz}\sin^2\alpha)\sin\beta + 2\chi_{xzx}\cos\alpha\sin\alpha\cos\beta] \\ +A_2&[-2\chi_{xzx}\cos\alpha\sin\alpha\sin\beta + (\chi_{zxx}\sin^2\alpha + \chi_{zzz}\cos^2\alpha)\cos\beta]|^2. \end{aligned} \tag{3}$$

Fits of Eq. 3 to data in Fig. 2(b,c) show that the one-phase model cannot satisfactorily describe the observed SHG polarimetry data of our PTO|STO superlattice even when considering a tensor $\hat{\chi}^{(2)}$ with real and imaginary components. We move onto the two-phase model to test whether it can appropriately model the SHG polarimetry measurements.

2. *Two-phase model*

We next consider the two-phase model in which the SHG contributions of the two phases have different spectral dependence denoted with components χ_{ijk} for the a_1/a_2-phase and χ'_{ijk} for the vortex phase. For the a_1/a_2-phase, we again describe the fractions of the regions with local polarization pointing towards [100], [$\bar{1}$00], [010] and [0$\bar{1}$0] with parameters A_1^+, A_1^-, A_2^+ and A_2^-, respectively. For the axial net polarization of the vortex phase, we describe the respective fractions of the regions with local polarization pointing towards [100] and [$\bar{1}$00] with parameters V^+ and V^-, respectively. We express the relative fractions of SHG signals originating from the a_1-domains as A_1, from the a_2-domains as A_2, and from the vortex phase as V:

$$A_1 = \frac{A_1^+ - A_1^-}{(A_1^+ - A_1^-) + (A_2^+ - A_2^-) + (V^+ - V^-)}, A_2 = \frac{A_2^+ - A_2^-}{(A_1^+ - A_1^-) + (A_2^+ - A_2^-) + (V^+ - V^-)}, V = \frac{V^+ - V^-}{(A_1^+ - A_1^-) + (A_2^+ - A_2^-) + (V^+ - V^-)}, \tag{4}$$

where $A_1 + A_2 + V = 1$. This leads to the following expression for the SHG intensity in our polarimetry measurements:

$$\begin{aligned} I^{2\omega}(\alpha,\beta) = |A_1&[-(\chi_{zxx}\cos^2\alpha + \chi_{zzz}\sin^2\alpha)\sin\beta + 2\chi_{xzx}\cos\alpha\sin\alpha\cos\beta] \\ +V&[-(\chi'_{zxx}\cos^2\alpha + \chi'_{zzz}\sin^2\alpha)\sin\beta + 2\chi'_{xzx}\cos\alpha\sin\alpha\cos\beta] \\ +A_2&[-2\chi_{xzx}\cos\alpha\sin\alpha\sin\beta + (\chi_{zxx}\sin^2\alpha + \chi_{zzz}\cos^2\alpha)\cos\beta]|^2. \end{aligned} \tag{5}$$

Because the SHG contributions of the a_1-domains and the net axial polarization of the vortex phase have an equivalent angular dependence on α and β (Eq. 5), we need to consider these SHG contributions with a single set of parameters. We therefore define the X parameters as $X_{ijk} = A_1\chi_{ijk} + V\chi'_{ijk}$. Equivalently for the a_2-domains, we define Y parameters as $Y_{ijk} = A_2\chi_{ijk}$, see Fig. 3(a,b). The final expression for the SHG intensity in our polarimetry measurements (black lines in Fig. 2(b,c)) is then:

$$I^{2\omega}(\alpha,\beta) = |-(X_{zxx}\cos^2\alpha + X_{zzz}\sin^2\alpha)\sin\beta + 2X_{xzx}\cos\alpha\sin\alpha\cos\beta \\ -2Y_{xzx}\cos\alpha\sin\alpha\sin\beta + (Y_{zxx}\sin^2\alpha + Y_{zzz}\cos^2\alpha)\cos\beta)|^2. \tag{6}$$

We see in Fig. 2 that the two-phase model indeed fully describes the results of our SHG polarimetry. The X and Y values used in the fitting are listed in Fig. 3(c). We next test the spectral dependence of the SHG responses of the a_1/a_2-phase and the vortex phase by scrutinizing the ratios of X and Y parameters:

$$X_{ijk}/Y_{ijk} = (A_1\chi_{ijk} + V\chi'_{ijk})/A_2\chi_{ijk}. \tag{7}$$

If the two phases were associated with the same SHG spectral dependence, the ratio would be equal for any set of i, j, k: $X_{ijk}/Y_{ijk} = (A_1 + V)/A_2$. However, we observe drastic differences in ratios X_{ijk}/Y_{ijk} in Fig. 3(c), showing that the SHG reponses of the a_1/a_2-phase and the vortex phase have different spectral dependences. This points to the very different microscopy of the electronic transitions and interactions establishing the two phases.

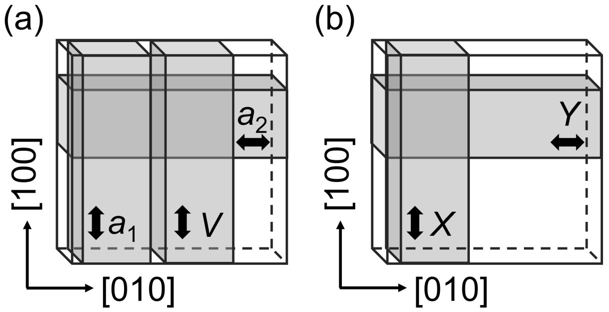

(c) ×8

ijk	X_{ijk}	Y_{ijk}	X_{ijk}/Y_{ijk}
zxx	0.004	0.442	0.009
zzz	0.802	-0.863	-0.929
xzx	0.221	0.435	0.508

FIG. 3. (a) Schematic of the orientation of the net polarization for the a_1-domains, the a_2-domains and the vortex phase (V). (b) Schematic of the relation of orientation of the local spontaneous polarization with respect to the crystallographic axes to the parameters X and Y which are used to model the SHG response. A value of 1 is set for the maximum SHG yield of the sample with respect to the choice of α and β. (c) Values of X_{ijk} and Y_{ijk} parameters obtained from the fitting of Eq. 6 for the PTO|STO superlattice and their ratio X_{ijk}/Y_{ijk}.

C. Observation of interlayer coupling in PTO|STO heterostructures

The PTO|STO superlattice architecture is commonly selected to increase the ferroelectric volume so that signals become measurable, while assuming that the characteristic features of a single PTO|STO bilayer remain preserved. Using the extreme sensitivity of the SHG polarimetry, we will verify to what extent the phase coexistence of the a_1/a_2-phase and the vortex phase in a single PTO$_{12}$|STO$_{12}$ bilayer is equivalent to that in the PTO|STO superlattice. In contrast to previous works where detecting this phase coexistence in samples with a single PTO layer was restricted to destructive methods [4, 9, 13], here we rely on a non-destructive method which allows operando investigation. The results of SHG polarimetry on a PTO|STO bilayer are shown in Fig. 4(a,b) and are qualitatively similar to the results of the SHG polarimetry of the superlattice. By modelling the SHG polarimetry for the bilayer following the procedure described for Fig. 3, we again find that only the two-phase model appropriately describes the measured SHG data,

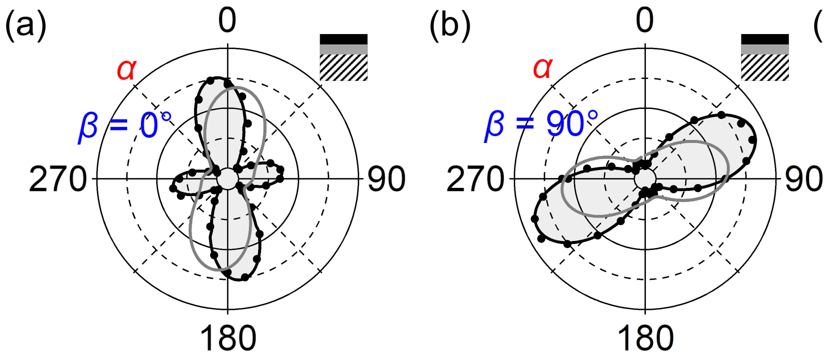

(c)

ijk	X_{ijk}	Y_{ijk}	X_{ijk}/Y_{ijk}
zxx	0.141	0.612	0.230
zzz	0.477	-0.892	-0.535
xzx	0.179	0.569	0.315

FIG. 4. (a,b) Polar plots of SHG intensity (points) versus incident-light polarization angle α for a PTO|STO bilayer for (a) $\beta = 0°$ and (b) $\beta = 90°$. Grey lines are theoretical fits of the one-phase model based on Eq. 3, and black lines are theoretical fits of the two-phase model based on Eq. 6. Schematic of the multilayer is given in the inset top right. Grey denotes PTO, black denotes STO, and hatching denotes the $SrRuO_3$-buffered $DyScO_3$ substrate. The intensity scale is equal in (a) and (b). (c) Values of X_{ijk} and Y_{ijk} parameters obtained from the fitting of Eq. 6 for the PTO|STO bilayer and their ratio X_{ijk}/Y_{ijk}.

see Fig. 4(c). This confirms the presence of the vortex phase in coexistence with the a_1/a_2-phase even in a single PTO|STO bilayer. Although it seems that, as expected, the supperlattice simply behaves as “many bilayers”, there is one interesting detail where this multiplicative effect does not hold.

Surprisingly, see Fig. 5, despite identical laser-excitation parameters, the SHG yield of a PTO|STO bilayer is twice the SHG yield of a $(PTO|STO)_8|PTO$ superlattice though the amount of ferroelectric material in the superlattice exceeds that of the bilayer by a factor of nine. Such a striking dependence of the SHG yield with the volume of ferroelectric material is in contradiction with the understanding that a superlattice architecture would increase the measured signals. This is clearly not the case for SHG which is sensitive to the phases of the waves determined by the polarization direction. The small SHG yield of the superlattice thus points to some form of quenching or compensation between SHG waves originating in different PTO layers of the superlattice [39]. In order to verify this assumption, we compare the SHG yield of $PTO_{12}|STO_{12}$ heterostructures with a different number of periods. Specifically, we integrate the signal of the SHG polarimetry data for $\beta = 0°$ for a single PTO layer, a PTO|STO bilayer, a PTO|STO|PTO trilayer and a $(PTO|STO)_8|PTO$ superlattice, see Fig. 5(a).

The SHG yield of a reference single PTO layer with a predominant out-of-plane polarization and a small admixture of in-plane domains [41, 42] is small in this in-plane-polarization-sensitive measurement configuration [35]. For a PTO|STO bilayer, we find that the formation of the a_1/a_2-phase and the vortex phase results in a 10 times higher SHG yield than in the case of a single layer. Surprisingly, when adding another PTO layer, the heterostructure yields a 20 times lower SHG intensity than in the case of the bilayer. This points to extended phase- and inverted domain configuration in neighboring PTO layers as sketched in Fig. 5(b). The spatial extension of the a_1/a_2-phase and the vortex phase in the neighboring layers is the same. The domain configuration in the respective phases in neighboring layers is also the same, that is, domain-walls align vertically throughout layers [4, 13, 43–48]. However, the sign of the local polarization is reversed from layer to layer. The destructive interference of SHG waves from the neighboring PTO layers was verified in more than 10 samples to exclude a random domain configuration in neighboring layers which would not consistently result in lower SHG yield of a trilayer than the bilayer.

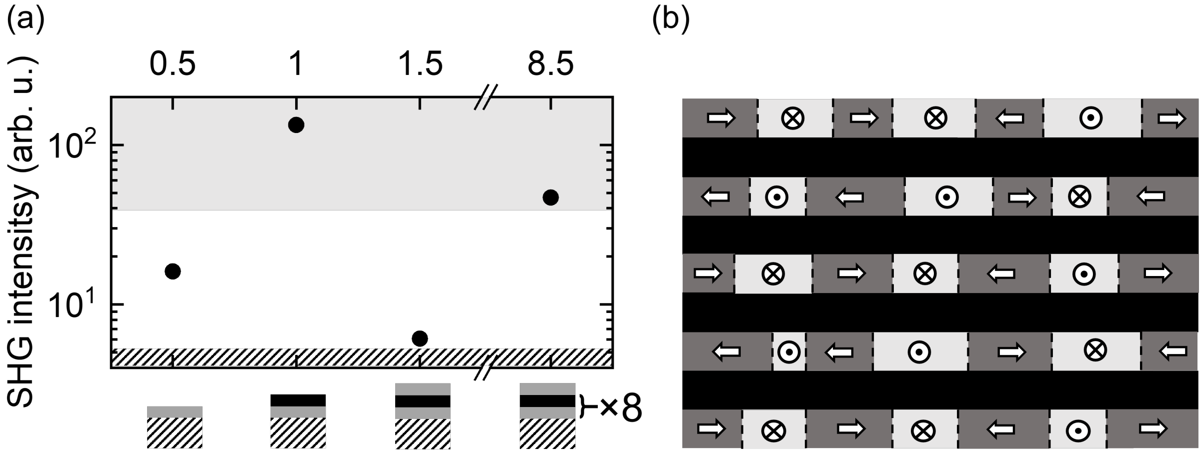

FIG. 5. (a) SHG intensity integrated with α for SHG polarimetry at $\beta = 0°$ as in Fig. 2(b) and in Fig. 4(a) for a single PTO layer, a PTO|STO bilayer, a PTO|STO|PTO trilayer and a (PTO|STO)$_8$|PTO superlattice, see schematics. Grey denotes PTO, black denotes STO, and hatching denotes the SrRuO$_3$-buffered DyScO$_3$ substrate. The hatched area corresponds to the background SHG intensity measured from the DyScO$_3$ substrate which is not SHG active in this measurement geometry. The grey shaded area corresponds to the SHG level which exceeds the background level an order of magnitude. To ensure quantitative comparability of the SHG yield of different samples, the SHG signal is normalized to a reference SHG signal in each case. (b) Idealized sketch of opposite polarization direction in neighboring PTO layers.

To verify that the extended phase- and inverted domain-coupling effect is not a mere thickness effect, we reinvoke that the SHG yield of the (PTO|STO)$_8$|PTO superlattice is two times smaller than the SHG yield of a bilayer, despite the ninefold amount of the ferroelectric material in the superlattice. We thus consolidate the model of extended phase- and inverted domain-coupling effect also for (PTO|STO)$_n$ heterostructures with a higher number of periods, independent of n. Specifically, for an odd number of bilayers, a finite SHG signal is observed, while for an even number of bilayers, a small SHG signal is observed. A superlattice is therefore a representative system for studying the polarization configuration in a single bilayer because it shows the same phase and domain configuration in each bilayer throughout the the heterostructure, except for the sign reversal in neighboring layers. Our non-invasive approach unambiguously identifies this previously-overlooked domain ordering within the volume of PTO|STO heterostructures.

III. CONCLUSION

To summarize, we have shown phase coexistence of the a_1/a_2-phase and the vortex phase in PTO|STO superlattices extending down to a single bilayer using a non-invasive optical approach. Drastic differences in the spectral dependence between the two phases are revealed by modelling the SHG polarimetry results which point to the different microscopy of these two phases in satisfying competing electrostatic and elastic energetics. Furthermore, we find an extended phase- and inverted domain-coupling effect between the neighboring PTO layers. Specifically, a compensating arrangement of local polarization directions occurs in neighboring PTO layers which results in an SHG yield which is about constant, rather than increasing, in thickness - it is either finite for an odd number of bilayers or small for an even number of bilayers. The superlattice not only hosts the same phase coexistence as a bilayer, but also the same phase and domain configuration in each bilayer, except for the locally opposite polarization direction in neighboring layers. We thus map an emergent arrangement of local polarization in three dimensions of ferroelectric-based multilayers by probing the net polarization of the heterostructures. We expect that our approach could be used as a complementary tool in identifying complex phases and their host systems, and operando monitoring of evolution of complex ordering under electric fields for the investigation of the switching dynamics of technology-relevant complex phases [16–20].

ACKNOWLEDGMENTS

M. T. acknowledges the Swiss National Science Foundation under Project No. 200021-188414. N. S., M. T. and M. F. acknowledge financial support by the EU European Research Council under Advanced Grant Program No. 694955-INSEETO and the Swiss National Science Foundation under Project No. 200021-I178825.

All authors discussed the results. N. S., M. T. and M. F. wrote the manuscript. N. S. performed the thin-film growth and the SHG measurements. A. B. performed the Monte Carlo simulations. M. C. and M. D. R. carried out the STEM investigation. M. T. and N. S. designed the experiment. M. T. supervised the work jointly with M. F.

[1] Y. L. Tang, Y. L. Zhu, X. L. Ma, A. Y. Borisevich, A. N. Morozovska, E. A. Eliseev, W. Y. Wang, Y. J. Wang, Y. B. Xu, Z. D. Zhang, and S. J. Pennycook, Observation of a periodic array of flux-closure quadrants in strained ferroelectric PbTiO films, Science **348**, 547 (2015).

[2] S. Li, Y. L. Zhu, Y. J. Wang, Y. L. Tang, Y. Liu, S. R. Zhang, J. Y. Ma, and X. L. Ma, Periodic arrays of flux-closure domains in ferroelectric thin films with oxide electrodes, Appl. Phys. Lett. **111**, 52901 (2017).

[3] A. K. Yadav, C. T. Nelson, S. L. Hsu, Z. Hong, J. D. Clarkson, C. M. Schlepüetz, A. R. Damodaran, P. Shafer, E. Arenholz, L. R. Dedon, D. Chen, A. Vishwanath, A. M. Minor, L. Q. Chen, J. F. Scott, L. W. Martin, and R. Ramesh, Observation of polar vortices in oxide superlattices, Nature **530**, 198 (2016).

[4] Z. Hong, A. R. Damodaran, F. Xue, S.-L. Hsu, J. Britson, A. K. Yadav, C. T. Nelson, J.-J. Wang, J. F. Scott, L. W. Martin, R. Ramesh, and L.-Q. Chen, Stability of Polar Vortex Lattice in Ferroelectric Superlattices, Nano Lett. **17**, 2246 (2017).

[5] A. R. Damodaran, J. D. Clarkson, Z. Hong, H. Liu, A. K. Yadav, C. T. Nelson, S.-L. Hsu, M. R. McCarter, K.-D. Park, V. Kravtsov, A. Farhan, Y. Dong, Z. Cai, H. Zhou, P. Aguado-Puente, P. Garcia-Fernandez, J. Iñiguez, J. Junquera, A. Scholl, M. B. Raschke, L.-Q. Chen, D. D. Fong, R. Ramesh, L. W. Martin, A. R. Damodaran, J. D. Clarkson, Z. Hong, H. Liu, A. K. Yadav, C. T. Nelson, S.-L. Hsu, M. R. McCarter, K.-D. Park, V. Kravtsov, A. Farhan, Y. Dong, Z. Cai, H. Zhou, P. Aguado-Puente, P. Garcia-Fernandez, J. Iniguez, J. Junquera, A. Scholl, M. B. Raschke, L.-Q. Chen, D. D. Fong, R. Ramesh, and L. W. Martin, Phase coexistence and electric-field control of toroidal order in oxide superlattices, Nat. Mater. **16**, 1003 (2017).

[6] S. Das, Y. L. Tang, Z. Hong, M. A. P. Gonçalves, M. R. McCarter, C. Klewe, K. X. Nguyen, F. Gómez-Ortiz, P. Shafer, E. Arenholz, V. A. Stoica, S.-L. Hsu, B. Wang, C. Ophus, J. F. Liu, C. T. Nelson, S. Saremi, B. Prasad, A. B. Mei, D. G. Schlom, J. Íñiguez, P. García-Fernández, D. A. Muller, L. Q. Chen, J. Junquera, L. W. Martin, and R. Ramesh, Observation of room-temperature polar skyrmions, Nature **568**, 368 (2019).

[7] V. A. Stoica, N. Laanait, C. Dai, Z. Hong, Y. Yuan, Z. Zhang, S. Lei, M. R. McCarter, A. Yadav, A. R. Damodaran, S. Das, G. A. Stone, J. Karapetrova, D. A. Walko, X. Zhang, L. W. Martin, R. Ramesh, L.-Q. Chen, H. Wen, V. Gopalan, and J. W. Freeland, Optical creation of a supercrystal with three-dimensional nanoscale periodicity, Nat. Mater. **18**, 377 (2019).

[8] Y. Sun, A. Y. Abid, C. Tan, C. Ren, M. Li, N. Li, P. Chen, Y. Li, J. Zhang, X. Zhong, J. Wang, M. Liao, K. Liu, X. Bai, Y. Zhou, D. Yu, and P. Gao, Subunit cell–level measurement of polarization in an individual polar vortex, Sci. Adv. **5**, 10.1126/sciadv.aav4355 (2019).

[9] S.-L. Hsu, M. R. McCarter, C. Dai, Z. Hong, L.-Q. Chen, C. T. Nelson, L. W. Martin, and R. Ramesh, Emergence of the vortex state in confined ferroelectric heterostructures, Advanced Materials **31**, 1901014 (2019).

[10] Y. J. Wang, Y. P. Feng, Y. L. Zhu, Y. L. Tang, L. X. Yang, M. J. Zou, W. R. Geng, M. J. Han, X. W. Guo, B. Wu, and X. L. Ma, Polar meron lattice in strained oxide ferroelectrics, Nat. Mater. **19** (2020).

[11] S. Das, Z. Hong, M. McCarter, P. Shafer, Y.-T. Shao, D. A. Muller, L. W. Martin, and R. Ramesh, A new era in ferroelectrics, APL Mater. **8**, 120902 (2020).

[12] S. Chen, S. Yuan, Z. Hou, Y. Tang, J. Zhang, T. Wang, K. Li, W. Zhao, X. Liu, L. Chen, L. W. Martin, and Z. Chen, Recent Progress on Topological Structures in Ferroic Thin Films and Heterostructures, Adv. Mater. **33**, 2000857 (2020).

[13] Y. Liu, Y.-J. Wang, Y.-L. Zhu, C.-H. Lei, Y.-L. Tang, S. Li, S.-R. Zhang, J. Li, and X.-L. Ma, Large scale two-dimensional flux-closure domain arrays in oxide multilayers and their controlled growth, Nano Lett. **17**, 7258 (2017).

[14] N. Strkalj, E. Gradauskaite, J. Nordlander, and M. Trassin, Design and Manipulation of Ferroic Domains in Complex Oxide Heterostructures, Materials **12**, 3108 (2019).

[15] Y. L. Tang, Y. L. Zhu, and X. L. Ma, Topological polar structures in ferroelectric oxide films, Journal of Applied Physics **129**, 200904 (2021).

[16] S. Salahuddin and S. Datta, Use of negative capacitance to provide voltage amplification for low power nanoscale devices, Nano Lett. **8**, 405 (2008).

[17] A. I. Khan, K. Chatterjee, B. Wang, S. Drapcho, L. You, C. Serrao, S. R. Bakaul, R. Ramesh, and S. Salahuddin, Negative capacitance in a ferroelectric capacitor, Nat. Mater. **14**, 182 (2015).

[18] P. Zubko, J. C. Wojdeł, M. Hadjimichael, S. Fernandez-Peña, A. Sené, I. Luk'yanchuk, J.-M. Triscone, and J. Íñiguez, Negative capacitance in multidomain ferroelectric superlattices, Nature **534**, 524 (2016).

[19] A. K. Yadav, K. X. Nguyen, Z. Hong, P. García-Fernández, P. Aguado-Puente, C. T. Nelson, S. Das, B. Prasad, D. Kwon, S. Cheema, A. I. Khan, C. Hu, J. Íñiguez, J. Junquera, L.-Q. Chen, D. A. Muller, R. Ramesh, and S. Salahuddin, Spatially resolved steady-state negative capacitance, Nature **565**, 468 (2019).

[20] J. Iñiguez, P. Zubko, I. Luk'yanchuk, and A. Cano, Ferroelectric negative capacitance, Nat. Rev. Mater. **4**, 243 (2019).

[21] S. Prosandeev, I. I. Naumov, H. Fu, L. Bellaiche, M. P. D. Campbell, R. G. P. McQuaid, L.-W. Chang, A. Schilling, L. J. McGilly, A. Kumar, and J. Marty Gregg, *Nanoscale Ferroelectr. Multiferroics*, Wiley Online Books (2016) pp. 700–728.

[22] S. A. Denev, T. T. A. Lummen, E. Barnes, A. Kumar, and V. Gopalan, Probing ferroelectrics using optical second harmonic generation, Journal of the American Ceramic Society **94**, 2699 (2011).

[23] J. Nordlander, G. De Luca, N. Strkalj, M. Fiebig, and M. Trassin, Probing Ferroic States in Oxide Thin Films Using Optical Second Harmonic Generation, Appl. Sci. **8**, 570 (2018).

[24] A. Prylepa, C. Reitböck, M. Cobet, A. Jesacher, X. Jin, R. Adelung, M. Schatzl-Linder, G. Luckeneder, K.-H. Stellnberger, T. Steck, J. Faderl, T. Stehrer, and D. Stifter, Material characterisation with methods of nonlinear optics, Journal of Physics D: Applied Physics **51**, 043001 (2018).

[25] V. Gopalan and R. Raj, Domain Structure-Second Harmonic Generation Correlation in Potassium Niobate Thin Films Deposited on a Strontium Titanate Substrate, J. Am. Ceram. Soc. **79**, 3289 (1996).

[26] C. J. Roh, S. Y. Hamh, C.-S. Woo, K.-E. Kim, C.-H. Yang, and J. S. Lee, Ferroelectric domain states of a tetragonal BiFeO3 thin film investigated by second harmonic generation microscopy, Nanoscale Res. Lett. **12**, 353 (2017).

[27] M. Trassin, G. D. Luca, S. Manz, and M. Fiebig, Probing Ferroelectric Domain Engineering in $BiFeO_3$ Thin Films by Second Harmonic Generation, Advanced Materials **27**, 4871 (2015).

[28] Y. Zhang, Y. Zhang, Q. Guo, X. Zhong, Y. Chu, H. Lu, G. Zhong, J. Jiang, C. Tan, M. Liao, Z. Lu, D. Zhang, J. Wang, J. Yuan, and Y. Zhou, Characterization of domain distributions by second harmonic generation in ferroelectrics, npj Comput. Mater. **4**, 39 (2018).

[29] J.-s. Wang, K.-j. Jin, H.-z. Guo, J.-x. Gu, Q. Wan, X. He, X.-l. Li, X.-l. Xu, and G.-z. Yang, Evolution of structural distortion in $BiFeO_3$ thin films probed by second-harmonic generation, Sci. Rep. **6**, 38268 (2016).

[30] A. Kumar, S. Denev, R. J. Zeches, E. Vlahos, N. J. Podraza, A. Melville, D. G. Schlom, R. Ramesh, and V. Gopalan, Probing mixed tetragonal/rhombohedral-like monoclinic phases in strained bismuth ferrite films by optical second harmonic generation, Applied Physics Letters **97**, 112903 (2010).

[31] N. Strkalj, G. De Luca, M. Campanini, J. Pal, S., Schaab, C. Gattinoni, N. A. Spaldin, M. D. Rossell, M. Fiebig, and M. Trassin, Depolarizing Field Effects in Epitaxial Capacitor Heterostructures, Phys. Rev. Lett. **123**, 147601 (2019).

[32] N. Strkalj, C. Gattinoni, A. Vogel, M. Campanini, R. Haerdi, A. Rossi, M. D. Rossell, N. A. Spaldin, M. Fiebig, and M. Trassin, In-situ monitoring of interface proximity effects on polarization in ultrathin ferroelectrics, Nat. Commun. **11**, 5815 (2020).

[33] M. F. Sarott, M. Fiebig, and M. Trassin, Tracking ferroelectric domain formation during epitaxial growth of $PbTiO_3$ films, Appl. Phys. Lett. **117**, 132901 (2020).

[34] S. Cherifi-Hertel, H. Bulou, R. Hertel, G. Taupier, K. D. H. Dorkenoo, C. Andreas, J. Guyonnet, I. Gaponenko, K. Gallo, and P. Paruch, Non-Ising and chiral ferroelectric domain walls revealed by nonlinear optical microscopy, Nat. Commun. **8**, 15768 (2017).

[35] G. De Luca, M. D. Rossell, J. Schaab, N. Viart, M. Fiebig, and M. Trassin, Domain Wall Architecture in Tetragonal Ferroelectric Thin Films, Adv. Mater. **29**, 1605145 (2017).

[36] V. Gopalan and R. Raj, Domain structure and phase transitions in epitaxial $KNbO_3$ thin films studied by in situ second harmonic generation measurements, Applied Physics Letters **68**, 1323 (1996).

[37] J. Nordlander, F. Eltes, M. Reynaud, J. Nürnberg, G. De Luca, D. Caimi, A. A. Demkov, S. Abel, M. Fiebig, J. Fompeyrine, and M. Trassin, Ferroelectric domain architecture and poling of $batio_3$ on si, Phys. Rev. Materials **4**, 034406 (2020).

[38] R. R. Birss, *Symmetry and magnetism* (North-Holland Publishing Company, 1964).

[39] G. De Luca, N. Strkalj, S. Manz, C. Bouillet, M. Fiebig, and M. Trassin, Nanoscale design of polarization in ultrathin ferroelectric heterostructures, Nat. Commun. **8**, 1419 (2017).

[40] P. Virtanen, R. Gommers, T. E. Oliphant, M. Haberland, T. Reddy, D. Cournapeau, E. Burovski, P. Peterson, W. Weckesser, J. Bright, S. J. van der Walt, M. Brett, J. Wilson, K. J. Millman, N. Mayorov, A. R. J. Nelson, E. Jones, R. Kern, E. Larson, C. J. Carey, İ. Polat, Y. Feng, E. W. Moore, J. VanderPlas, D. Laxalde, J. Perktold, R. Cimrman, I. Henriksen, E. A. Quintero, C. R. Harris, A. M. Archibald, A. H. Ribeiro, F. Pedregosa, P. van Mulbregt, and SciPy 1.0 Contributors, SciPy 1.0: Fundamental Algorithms for Scientific Computing in Python, Nature Methods **17**, 261 (2020).

[41] N. A. Pertsev and V. G. Koukhar, Polarization Instability in Polydomain Ferroelectric Epitaxial Thin Films and the Formation of Heterophase Structures, Phys. Rev. Lett. **84**, 3722 (2000).

[42] N. A. Pertsev, A. G. Zembilgotov, and A. K. Tagantsev, Effect of Mechanical Boundary Conditions on Phase Diagrams of Epitaxial Ferroelectric Thin Films, Phys. Rev. Lett. **80**, 1988 (1998).

[43] V. A. Stephanovich, I. A. Luk'yanchuk, and M. G. Karkut, Domain-Enhanced Interlayer Coupling in Ferroelectric|Paraelectric Superlattices, Phys. Rev. Lett. **94**, 47601 (2005).

[44] M. Hadjimichael, Y. Li, E. Zatterin, G. A. Chahine, M. Conroy, K. Moore, E. N. O. Connell, P. Ondrejkovic, P. Marton, J. Hlinka, U. Bangert, S. Leake, and P. Zubko, Metal–ferroelectric supercrystals with periodically curved metallic layers, Nat. Mater. **20**, 495 (2021).

[45] P. Zubko, N. Jecklin, A. Torres-Pardo, P. Aguado-Puente, A. Gloter, C. Lichtensteiger, J. Junquera, O. Stéphan, and J.-M. Triscone, Electrostatic Coupling and Local Structural Distortions at Interfaces in Ferroelectric|Paraelectric Superlattices, Nano Lett. **12**, 2846 (2012).

[46] M. Hadjimichael, E. Zatterin, S. Fernandez-Peña, S. J. Leake, and P. Zubko, Domain wall orientations in ferroelectric superlattices probed with synchrotron x-ray diffraction, Phys. Rev. Lett. **120**, 037602 (2018).

[47] N. Strkalj, M. Bernet, M. F. Sarott, J. Schaab, T. Weber, M. Fiebig, and M. Trassin, Stabilization and manipulation of in-plane polarization in a ferroelectric|dielectric superlattice, Journal of Applied Physics **129**, 174104 (2021).

[48] Z. Hong, S. Das, C. Nelson, A. Yadav, Y. Wu, J. Junquera, L.-Q. Chen, L. W. Martin, and R. Ramesh, Vortex Domain Walls in Ferroelectrics, Nano Lett. **21**, 3533 (2021).

Supplemental Material: Optical second harmonic signature of phase coexistence in ferroelectric|dielectric heterostructures

Nives Strkalj[1],* Amadé Bortis[1], Marco Campanini[2],
Marta D. Rossell[2], Manfred Fiebig[1], and Morgan Trassin[1]
[1] *Department of Materials, ETH Zurich, 8093 Zurich, Switzerland*
[2] *Electron Microscopy Center, Swiss Federal Laboratories for Materials Science and Technology, Empa, Dübendorf, 8600, Switzerland*

(Dated: August 11, 2021)

I. DETAILS OF THE SAMPLE PREPARATION AND CHARACTERIZATION

Heterostructures were synthesized by pulsed-laser deposition on single-crystalline (110)-oriented $DyScO_3$ (DSO) substrate (Crystec GmbH) with a miscut of 0.1°, buffered by 4 nm-thick (001)-oriented $SrRuO_3$ using a KrF (248 nm) excimer laser. After optimizing the growth conditions, the SRO layer was deposited at 700°C in an O_2 pressure of 0.1 mbar at a laser fluence of 0.9 Jcm^{-2} and a repetition rate of 2 Hz. The PTO and STO layers were deposited at 550°C in an O_2 pressure of 0.12 mbar at a laser fluence of 1.14 Jcm^{-2} and a repetition rate of 4 and 2 Hz, respectively. Simultaneously, reflection high energy electron diffraction (RHEED) is performed to ensure the growth quality and calibrate the ISHG yield to the film thickness with unit-cell (u. c.) accuracy, see Supplementary Fig. 1a,b. We note that a Pb-enriched target ($Pb_{1.2}TiO_3$) was used to achieve the layer-by-layer growth mode for RHEED monitoring, see Supplementary Fig. 1(a,b). The sample was cooled at 10 K/min in the oxygen growth atmosphere. The surface topography is shown in Supplementary Fig. 1(c). As previously reported in the system [1], the phases are separated in stripes with a width of about 200 nm along [010], and a length of about 2 μm along [100], see Fig. 2(a,b).

[1] A. R. Damodaran, J. D. Clarkson, Z. Hong, H. Liu, A. K. Yadav, C. T. Nelson, S.-L. Hsu, M. R. McCarter, K.-D. Park, V. Kravtsov, A. Farhan, Y. Dong, Z. Cai, H. Zhou, P. Aguado-Puente, P. Garcia-Fernandez, J. Iñiguez, J. Junquera, A. Scholl, M. B. Raschke, L.-Q. Chen, D. D. Fong, R. Ramesh, L. W. Martin, A. R. Damodaran, J. D. Clarkson, Z. Hong, H. Liu, A. K. Yadav, C. T. Nelson, S.-L. Hsu, M. R. McCarter, K.-D. Park, V. Kravtsov, A. Farhan, Y. Dong, Z. Cai, H. Zhou, P. Aguado-Puente, P. Garcia-Fernandez, J. Iniguez, J. Junquera, A. Scholl, M. B. Raschke, L.-Q. Chen, D. D. Fong, R. Ramesh, and L. W. Martin, Phase coexistence and electric-field control of toroidal order in oxide superlattices, Nat. Mater. **16**, 1003 (2017).

---

* nives.strkalj@mat.ethz.ch

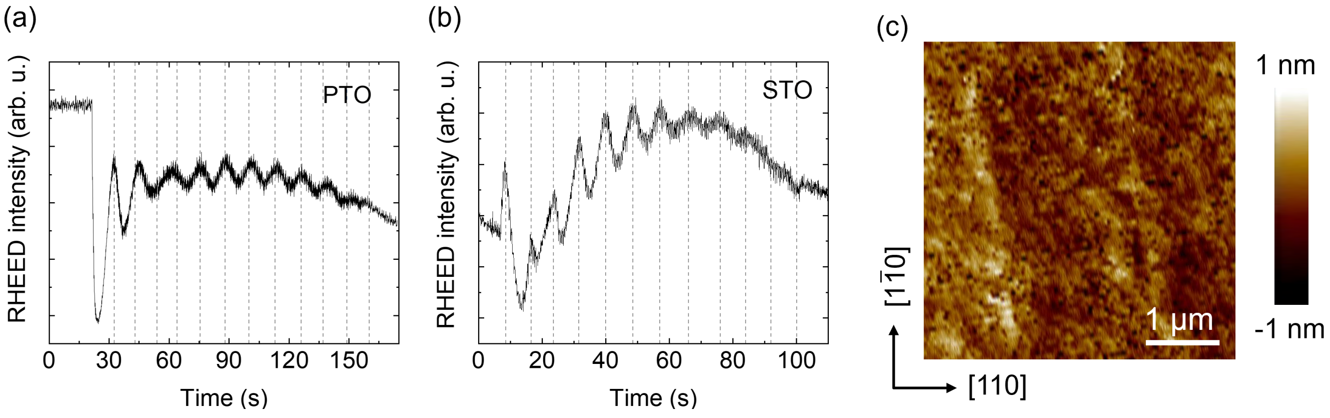

FIG. 1. (a,b) Time-dependent RHEED monitoring of the PTO and STO layers in the $PTO_{12}|STO_{12}$ superlattice. (c) Topography image.

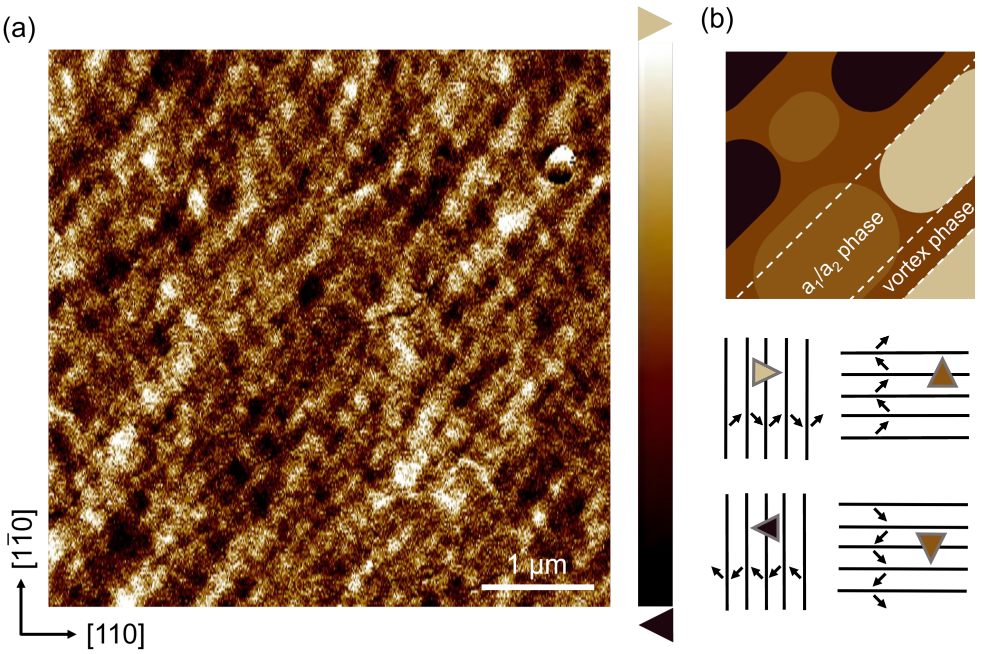

FIG. 2. (a) Image of the lateral PFM response. (b) Idealized sketch of the phase coexistence as oberved by PFM (top). In the a_1/a_2-phase, superdomains with a net polarization along [110] and [1$\bar{1}$0] are observed because the individual a_1- and a_2-domains have a lateral size below the resolution limit of the PFM method (bottom).

Stabilization and manipulation of in-plane polarization in a ferroelectric-dielectric superlattice

D

Preprint: N. Strkalj, M. Bernet, M. F. Sarott, J. Schaab, M. Fiebig, and M. Trassin. “Stabilization and Manipulation of In-plane Polarization in a Ferroelectric|Dielectric Superlattice”, *J. Appl. Phys.* **129**, 174104 (2020). Supplementary information is available online.

Stabilization and manipulation of in-plane polarization in a ferroelectric|dielectric superlattice

Nives Strkalj,[1, a)] Marco Bernet,[1] Martin F. Sarott,[1] Jakob Schaab,[1] Thomas Weber,[1] Manfred Fiebig,[1] and Morgan Trassin[1]
Department of Materials, ETH Zurich, 8093 Zurich, Switzerland

(Dated: 13 April 2021)

We investigate in-plane ferroelectricity in an epitaxial ferroelectric|dielectric $PbTiO_3|SrTiO_3$ (PTO|STO) superlattice under tensile strain. Using a combination of x-ray diffraction (XRD) and piezoresponse force microscopy (PFM), we identify a strain-induced periodic in-plane nanoscale domain architecture with polarization along the base diagonals of the PTO unit cell. We scrutinize its switching behavior using local in-plane trailing fields from the scanning-probe tip. For an electric field pointing in the polarization direction of a specific domain state, we create stable single domain areas of in-plane polarization at the scale of tens of micrometers. Our findings on controlling robust in-plane ferroelectricity in ultrathin ferroelectric layers can help to develop device concepts unaffected by the detrimental effects of the depolarizing field.

I. INTRODUCTION

The increasing energy demands drive the need for reducing the power consumption of electronic devices. Ferroelectric thin films are a potential platform for energy-efficient technologies because their functionality — polarization — is controlled simply by electric fields. In particular, ferroelectric thin films with in-plane-oriented polarization have been identified as promising candidates for electronic, photonic and photovoltaic applications[1–6] because of the absence of depolarizing-field effects in in-plane-polarized films. An in-plane polarization in oxide films and superlattices can be readily stabilized by chemical or epitaxial strain. However, by design, in-plane ferroelectricity generally exhibits one or more polarization axes and no preferential polarization direction along any axis which often leads to complex domain configurations at the nanoscale[7–15]. Such complex configurations are detrimental to the visualization and deterministic switching of in-plane polarization, a key requirement for reliable ferroelectric device performance.

So far, reports deal with the visualization and manipulation of in-plane polarization in the thickness range of above 30 nanometers[7,16–20]. Controlled manipulation of in-plane polarization in the technologically relevant ultrathin regime, i. e. below ten nanometers, has remained elusive because of the difficulty to probe polarization in such a small amount of material.

In this work, we stabilize in-plane polarization in the PTO|STO superlattice under tensile strain. Through periodic repetition of ultrathin layers, the PTO|STO superlattice provides sufficient volume of the ferroelectric material for investigation of the in-plane domain configuration using a combination of XRD and PFM[21,22], yet retains the characteristic features of an ultrathin film. We identify the nanoscale domain architecture and observe its anisotropic switching behavior under the application of in-plane electric fields. Finally, we demonstrate deterministic creation of single-domain regions at the scale of tens of micrometers. Our work thus suggests an efficient route towards controlling polarization in planar device geometries which is necessary for achieving robust oxide-electronic functionalities in the ultrathin regime.

II. SUPERLATTICE DESIGN AND STRUCTURAL CHARACTERIZATION

We grew our $PTO_{12}|STO_{12}$ superlattice by pulsed-laser deposition on a single-crystalline (110)-oriented $GdScO_3$ (GSO) substrate (Crystec GmbH) buffered by 10 unit cells (u. c.) of metallic (001)-oriented $SrRuO_3$ (SRO). The GSO substrate imposes tensile strain to the lattices of PTO and STO, thus favoring an in-plane polarization[21,22]. Details on the lattice mismatch of the superlattice layers with the substrate are given in Supplementary Table 1. The superlattice consists of four repetitions of PTO|STO and an additional PTO layer on top. The SRO buffer layer serves as the bottom electrode for the characterization by scanning probe microscopy.

Both PTO and STO were deposited at 550°C at an O_2 pressure of 0.12 mbar using a laser fluence of 1.14 Jcm^{-2} and a repetition rate of 4 and 2 Hz, respectively. The SRO was deposited at a substrate temperature of 700°C at an O_2 pressure of 0.1 mbar using a laser fluence of 0.9 Jcm^{-2} and a repetition rate of 2 Hz. Real-time in-situ reflection high energy electron diffraction (RHEED) was used to monitor the film thickness with u. c. accuracy during the entire superlattice deposition process. A Pb-enriched target ($Pb_{1.2}TiO_3$) was used to achieve the layer-by-layer growth mode for RHEED monitoring[23,24]. After deposition, the sample was cooled at 10 $Kmin^{-1}$ in the oxygen growth atmosphere.

In contrast to previous work on “thick" single layers or superlattices of PTO on GSO[11,25–28], we focus here on a superlattice architecture with ultrathin layers for two reasons. First, ultrathin films are less likely to release the tensile strain imposed by the substrate and are thus expected to exhibit large fully in-plane polarized domains[29]. Second, in the case of a superlattice with ultrathin layers, electrostriction at interfaces causes the domain walls to run perpendicular to the film throughout the sequence of PTO|STO layers[26,30–33]. All fer-

---

[a)] Electronic mail: nives.strkalj@mat.ethz.ch

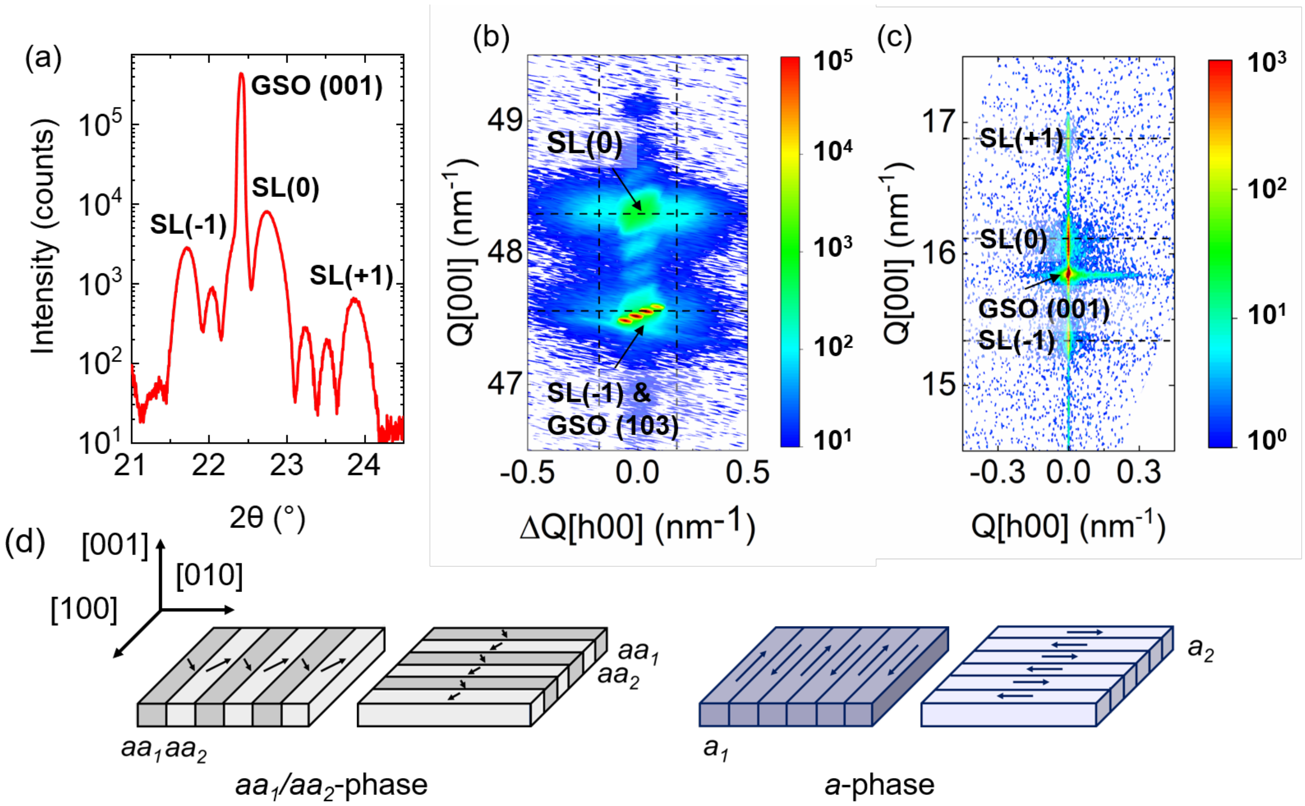

FIG. 1. (a) The x-ray intensity in a symmetric θ-2θ scan around GSO (001) reflection for the $PTO_{12}|STO_{12}$ superlattice (SL) on an SRO-buffered (110)-GSO substrate. (b,c) RSMs around (b) the GSO (103) reflection and (c) the GSO (001) reflection. Horizontal dashed black lines indicate the positions of the superlattice reflections and vertical dashed black lines indicate the positions of the diffuse scattering. (d) Schematic of the two possible domain configurations denoted as: aa_1/aa_2-phase (left) and a-phase (right).

roelectric layers of the superlattice thus host an identical domain configuration. The superlattice architecture yields an increased ferroelectric volume enabling structural and ferroelectric characterization, while keeping the characteristic features of an individual ultrathin layer.

We begin our investigation with the analysis of the crystalline structure of our PTO|STO superlattice by x-ray diffraction using a dedicated four-circle thin film diffractometer. All crystallographic directions used henceforth refer to the PTO tetragonal lattice. All GSO reflections in XRD measurements refer to the pseudocubic lattice. Thickness fringes in a symmetric θ-2θ scan around the superlattice (001) central Bragg reflection in Fig. 1(a) confirm the excellent crystallinity of our films, the uniform thickness of individual layers and the atomically-sharp interfaces within the superlattice.

Reciprocal space maps (RSMs) in Fig. 1(b,c) show that the overall structure is coherently tensile-strained to the GSO substrate because all layers have equal in-plane lattice parameters. Aside from the structural periodicity of the superlattice observed along the [00l] direction, the presence of diffuse scattering along the [h00] direction at $Q \approx 0.18\ \mathrm{nm}^{-1}$ for the (103) reflection in Fig.1(b) indicates an additional periodicity of about 35 nm within the superlattice plane. The appearance of such diffuse scattering is the result of a periodic stripe-like arrangement of ferroelectric domains and domain walls in the PTO layers[8,23,34]. We note that the appearance of the diffuse scattering at each superlattice peak is consistent with the suspected vertical ordering of domain configuration in each PTO layer of our superlattice[26,30–32].

According to previous work on PTO|STO superlattices, the domain walls can run along the principal tetragonal axes[8,34], $\langle 100 \rangle$, or diagonal to these[8,33], $\langle 110 \rangle$. In our superlattice, the former is the case, as indicated by diffuse scattering along the principal axis. We exclude any additional domain-wall orientations or other origins of the observed diffuse scattering, see Supplementary Fig. 1.

The direction of the spontaneous polarization is revealed by the absence of diffuse scattering for the (001) reflection in Fig. 1(c). Diffuse scattering for the 00l reflection would typically come along with the emergence of order with the spontaneous polarization out-of-plane[35]. We conclude that the polarization has to be oriented perpendicular to the [00l] direction i.e. must be fully in-plane.

In summary, we find that our PTO|STO superlattice is in-plane polarized and forms stripe-domain configurations with domains running along the principal axes.

Two possible domain configurations are consistent with the RSM data. (i) In the so-called aa_1/aa_2-phase, the polarization is along the base diagonals of the PTO u. c. Domains with a polarization along [110] are termed aa_1 domains and domains with a polarization along $[1\bar{1}0]$ are termed aa_2 domains. The domains arrange in stripes with alternating aa_1 and aa_2 domains, see Fig. 1(d) (left), which is denoted as aa_1/aa_2 domain configuration. (ii) In the a-phase, the polarization is along the base edges a of the PTO u. c. Domains with a polarization along [100] are termed a_1 domains and domains with a polarization along [010] are termed a_2 domains. The domains arrange in stripes of a_1 or a_2 domains with alternatingly reversed polarization, see Fig. 1(d) (right). To further elucidate the in-plane domain configuration, we now move on to the direct visualization of the in-plane polarization using PFM.

III. PIEZORESPONSE FORCE MICROSCOPY AND ELECTRICAL POLING

PFM enables non-destructive high-resolution visualization and localized control of ferroelectric nanoscale domains[36,37]. For fully in-plane polarized ferroelectric materials, lateral piezoresponse force microscopy (LPFM) detects torsion of the cantilever as a result of in-plane polarization orthogonal to the cantilever axis. Vertical piezoresponse force microscopy (VPFM) detects buckling of the cantilever as a result of in-plane polarization parallel to the cantilever axis. The PFM contrast is recorded in Cartesian coordinates, following subtraction of background contributions caused by the experimental setup as detailed in the Supplementary Section II.

Our measurements were performed on an NT-MDT Ntegra Prima microscope with Pt-coated NSC35 tips (MikroMasch). An alternating voltage of 1 V is applied between the tip and the SRO bottom electrode. We verified that the PFM response is not affected by the topography of the sample, see Supplementary Fig. 2.

A. As-grown domain configuration

In-plane domains are resolved in the LPFM response of the as-grown domain configuration, as shown in Fig. 2(a). The domain size is at the resolution limit of the PFM technique[37]. The orientation of the domain walls is along the $\langle 100\rangle$ directions, in agreement with the domain architecture extracted from the RSM in Fig. 1(b). The detailed analysis of the as-grown domain configuration is given in Supplementary Fig. 3.

When scanning along the [110] direction of the aa_1/aa_2-phase, the cantilever axis lies either orthogonal to the polarization (two LPFM contrast levels) or along the polarization (zero LPFM contrast level). In total, the aa_1/aa_2-phase hence yields three LPFM contrast levels for the [110] scanning direction, see Fig. 2b. In contrast, when scanning along the [110] direction of the a-phase, we expect only two LPFM contrast levels. One LPFM contrast level is obtained for the cantilever axis at either a 45° angle to the [100]-oriented polarization or a 135° angle to the $[0\bar{1}0]$-oriented polarization. Another LPFM contrast level is obtained for the opposite configuration of the cantilever axis with respect to the other [010]-oriented and $[\bar{1}00]$-oriented polarization states.

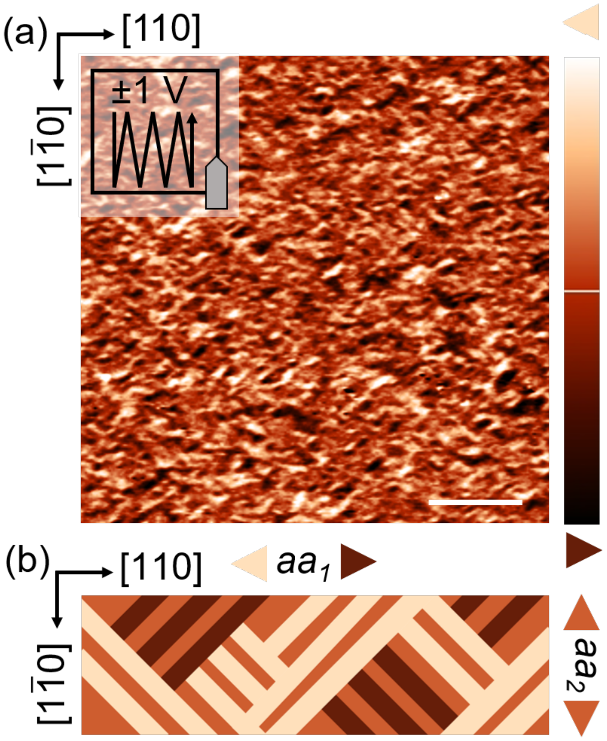

FIG. 2. (a) LPFM of a PTO$_{12}$|STO$_{12}$ superlattice on an SRO-buffered (110)-oriented GSO substrate. The scale bar is 2 µm. Sketches represent the tip and scanning orientation with respect to the crystallographic axes. (b) Idealized sketch of the domain configuration with polarization directions of the aa_1/aa_2-phase indicated on top and left sides.

From the presence of three contrast levels in Fig. 2a and Supplementary Fig. 3a, we conclude that the GSO tensile strain stabilizes the aa_1/aa_2 domain configuration in our superlattice. This domain configuration has been predicted by theory in tensile-strained films[12,13,38]. However, its experimental observation has so far been restricted to chemically strained Ba$_{1\text{-x}}$Sr$_\text{x}$TiO$_3$ films[6]. Here, the combination of the reduced PTO thickness in the superlattice architecture and of tensile strain imposed by the substrate leads to an unprecedented stabilization of the aa_1/aa_2 domain configuration in the PTO|STO system. Most importantly, the presence of the bottom electrode now provides the unprecedented opportunity to investigate the local switching behavior of this domain configuration.

B. Poling with in-plane electric fields along the $\langle 100\rangle$ axes

We directly manipulate the in-plane polarization of our superlattice by making use of the in-plane trailing field[7,17–20,39–42]. The slow scanning axis defines the trailing-

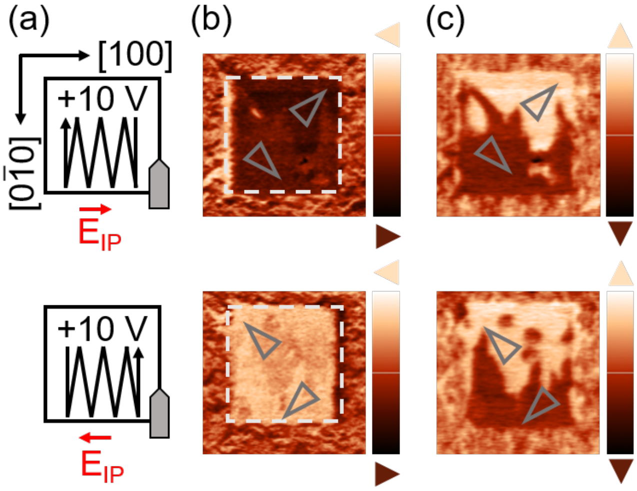

FIG. 3. (a) Sketches representing tip (gray), scanning trace (zigzag line) with respect to the crystallographic axes and the resulting in-plane electric trailing field E_{IP}. (b) LPFM and (c) VPFM images resulting after the application of the in-plane electric trailing field to the 2.5×2.5 μm^2 area highlighted by the white dashed outline. Grey triangles mark the polarization direction within the poled area.

field direction as sketched in Fig. 3(a). When poling an area, the alternating voltage is turned off and only a DC voltage of ±10 V is applied between the tip and the SRO bottom electrode.

We begin our investigation by applying the in-plane trailing field in the [100] direction and mapping the resulting polarization configuration. In the poled area, a uniform orientation of polarization in the [100] direction is observed in LPFM, see Fig. 3(b). However, a more complex polarization configuration is identified along the $[0\bar{1}0]$ direction in VPFM, see Fig. 3(c). This reveals that the trailing field in the [100] direction leads to an expansion of domains with polarization in the [110] direction (aa_1) as well as the $[1\bar{1}0]$ direction (aa_2). The direction of the trailing field can be reversed to $[\bar{1}00]$ by either reversing the voltage polarity or the scanning direction. In the case of a reversed direction of the trailing field, we observe an equivalent expansion of domains with polarization in the $[\bar{1}10]$ direction and domains with polarization in the $[\bar{1}\bar{1}0]$ direction, see Fig. 3 (lower panel). All VPFM signals are a result of cantilever buckling caused by the in-plane polarization, and is not a result of cantilever deflection caused by out-of-plane polarization. This is confirmed by rotating the sample by 45° after poling and measuring the LPFM and VPFM responses, see Supplementary Fig. 4.

Because all domain states of the aa_1/aa_2 domain configuration possess a polarization projection along the [100] direction, a trailing field along [100] always results in a multi-domain structure. Starting from the four domain states of the as-grown domain configuration, we show selective expansion of two domain states. Let us now investigate a way to break the degeneracy of the four in-plane polarization states in order to stabilize single domains with a lateral extension of several micrometers in our ultrathin PTO layers.

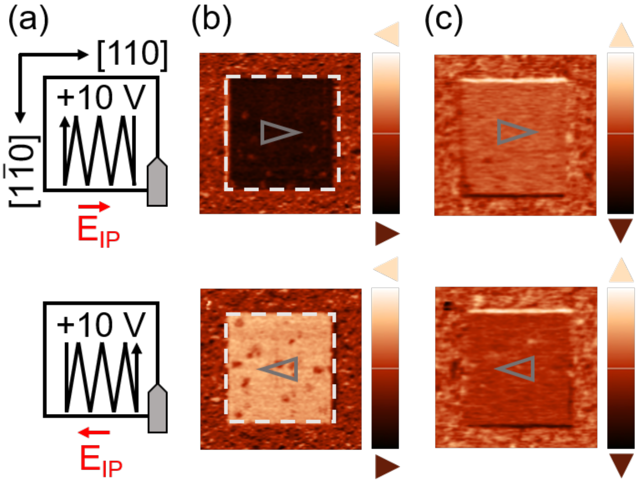

FIG. 4. (a) Sketches representing tip (gray), scanning trace (zigzag line) with respect to the crystallographic axes and the resulting in-plane electric trailing field E_{IP}. (b) LPFM and (c) VPFM images resulting after the application of the in-plane electric trailing field to the 5×5 μm^2 area highlighted by the white dashed outline. Grey triangles mark the polarization direction within the poled area.

C. Poling with in-plane electric fields along the ⟨110⟩ axes

We set the in-plane trailing field in the direction of polarization of one of the possible in-plane polarized states, here choosing the aa_1 variant with a polarization in the [110] direction. We pole and map the sample as described in the previous subsection. In the poled area, a uniform orientation of in-plane polarization in the [110] direction is observed, see Fig. 4(b). Here, no transversal response is detected, see Fig. 4(c). This points to the presence of a single in-plane domain comprising the entire poled area. The data shown in the bottom row of Fig. 4 for the case of a trailing field applied in the $[\bar{1}\bar{1}0]$ direction show a single in-plane domain with the polarization in the $[\bar{1}\bar{1}0]$ direction. This evidences a high degree of control over the spontaneous polarization. Strikingly, no changes to the poled single-domain region were observed over a 90-day time period at ambient conditions. Experiments on larger areas revealed that a single domain could be achieved up to regions of hundreds of μm^2, see Supplementary Fig. 5. Such stability of a single-domain state of tens of micrometers shows the robustness of an in-plane ferroelectric domain configuration against the influence of the depolarizing field[7,43,44]. To the best of our knowledge, such control of in-plane polarization towards robust and large single-domain regions was not achieved before. Our observation should therefore stimulate the discussion on the hitherto unrecognized parameters determining the equilibrium phase and domain size in ultrathin films[45,46].

IV. CONCLUSION

To conclude, we engineer an in-plane-polarized aa_1/aa_2 domain configuration in our PTO|STO superlattices. By reducing the layer thickness, while at the same time making use of the superlattice architecture, we increase the volume for XRD and PFM characterization, yet keep the characteristics of an ultrathin film. We further manipulate this domain configuration using in-plane electric trailing fields of the scanning-probe tip. By favoring the polarization direction of a specific domain state of the aa_1/aa_2 domain configuration, we deterministically create robust in-plane polarized domains with a lateral expansion at the scale of tens of micrometers. This level of control is a step forward in the design of devices based on in-plane polarized thin films where depolarizing fields have no effect[1–6].

V. SUPPLEMENTARY MATERIAL

See supplementary material for additional superlattice structural parameters and characterization by XRD. Supplementary material further includes topography and VPFM of the as-grown domain structure. Lastly, we append PFM results along the $\langle 110\rangle$ axes after electrical poling along the $\langle 100\rangle$ axes and the PFM results along the $\langle 110\rangle$ axes after electrical poling along the $\langle 110\rangle$ axes for lateral extensions of 10 μm and 20 μm.

ACKNOWLEDGMENTS

M. T. acknowledges the Swiss National Science Foundation under Project No. 200021-188414. N. S., M. T., and M. F. acknowledge financial support by the EU European Research Council under Advanced Grant Program No. 694955-INSEETO. The authors thank Elzbieta Gradauskaite for experimental support. The authors acknowledge the use of the D-MATL X-Ray Service Platform at ETH Zurich.

AUTHORS' CONTRIBUTION

All authors discussed the results. N. S., M. T. and M. F. wrote the manuscript. N. S. performed the thin film growth. N. S., M. F. S. and T. W. performed the structural XRD analysis. M. B. and J. S. performed the PFM measurements. M. T. and N. S. designed the experiment and supervised the work jointly with M.F.

DATA AVAILABILITY

The data that support the findings of this study are available from the corresponding author upon request.

REFERENCES

[1] S. Abel, F. Eltes, J. E. Ortmann, A. Messner, P. Castera, T. Wagner, D. Urbonas, A. Rosa, A. M. Gutierrez, D. Tulli, P. Ma, B. Baeuerle, A. Josten, W. Heni, D. Caimi, L. Czornomaz, A. A. Demkov, J. Leuthold, P. Sanchis, and J. Fompeyrine, "Large Pockels effect in micro- and nanostructured barium titanate integrated on silicon," Nat. Mater. **18**, 42–47 (2019).

[2] K. Yao, B. K. Gan, M. Chen, and S. Shannigrahi, "Large photo-induced voltage in a ferroelectric thin film with in-plane polarization," Appl. Phys. Lett. **87**, 212906 (2005).

[3] S. Y. Yang, J. Seidel, S. J. Byrnes, P. Shafer, C.-H. Yang, M. D. Rossell, P. Yu, Y.-H. Chu, J. F. Scott, J. W. Ager III, L. W. Martin, and R. Ramesh, "Above-bandgap voltages from ferroelectric photovoltaic devices," Nat. Nanotechnol. **5**, 143 (2010).

[4] J. A. Mundy, J. Schaab, Y. Kumagai, A. Cano, M. Stengel, I. P. Krug, D. M. Gottlob, H. Doğanay, M. E. Holtz, R. Held, Z. Yan, E. Bourret, C. M. Schneider, D. G. Schlom, D. A. Muller, R. Ramesh, N. A. Spaldin, and D. Meier, "Functional electronic inversion layers at ferroelectric domain walls," Nat. Mater. **16**, 622–627 (2017).

[5] H. Shen, J. Liu, K. Chang, and L. Fu, "In-plane ferroelectric tunnel junction," Phys. Rev. Applied **11**, 024048 (2019).

[6] Z. Gu, S. Pandya, A. Samanta, S. Liu, G. Xiao, C. J. G. Meyers, A. R. Damodaran, H. Barak, A. Dasgupta, S. Saremi, A. Polemi, L. Wu, A. A. Podpirka, A. Will-Cole, C. J. Hawley, P. K. Davies, R. A. York, I. Grinberg, L. W. Martin, and J. E. Spanier, "Resonant domain-wall-enhanced tunable microwave ferroelectrics," Nature **560**, 622–627 (2018).

[7] S. Matzen, O. Nesterov, G. Rispens, J. A. Heuver, M. Biegalski, H. M. Christen, and B. Noheda, "Super switching and control of in-plane ferroelectric nanodomains in strained thin films," Nat. Commun. **5**, 4415 (2014).

[8] A. R. Damodaran, J. D. Clarkson, Z. Hong, H. Liu, A. K. Yadav, C. T. Nelson, S.-L. Hsu, M. R. McCarter, K.-D. Park, V. Kravtsov, A. Farhan, Y. Dong, Z. Cai, H. Zhou, P. Aguado-Puente, P. Garcia-Fernandez, J. Iniguez, J. Junquera, A. Scholl, M. B. Raschke, L.-Q. Chen, D. D. Fong, R. Ramesh, and L. W. Martin, "Phase coexistence and electric-field control of toroidal order in oxide superlattices," Nat. Mater. **16**, 1003–1009 (2017).

[9] A. R. Damodaran, S. Pandya, J. C. Agar, Y. Cao, R. K. Vasudevan, R. Xu, S. Saremi, Q. Li, J. Kim, M. R. McCarter, *et al.*, "Three-state ferroelastic switching and large electromechanical responses in pbtio$_3$ thin films," Adv. Mater. **29**, 1702069 (2017).

[10] A. S. Everhardt, S. Damerio, J. A. Zorn, S. Zhou, N. Domingo, G. Catalan, E. K. H. Salje, L.-Q. Chen, and B. Noheda, "Periodicity-doubling cascades: Direct observation in ferroelastic materials," Phys. Rev. Lett. **123**, 087603 (2019).

[11] E. Langenberg, H. Paik, E. H. Smith, H. P. Nair, I. Hanke, S. Ganschow, G. Catalan, N. Domingo, and D. G. Schlom, "Strain-Engineered Ferroelastic Structures in PbTiO$_3$ Films and Their Control by Electric Fields," ACS Appl. Mater. Interfaces **12**, 20691–20703 (2020).

[12] V. G. Koukhar, N. A. Pertsev, and R. Waser, "Thermodynamic theory of epitaxial ferroelectric thin films with dense domain structures," Phys. Rev. B **64**, 214103 (2001).

[13] V. G. Kukhar, N. A. Pertsev, H. Kohlstedt, and R. Waser, "Polarization states of polydomain epitaxial Pb(Zr$_{1-x}$Ti$_x$)O$_3$ thin films and their dielectric properties," Phys. Rev. B **73**, 214103 (2006).

[14] N. Strkalj, E. Gradauskaite, J. Nordlander, and M. Trassin, "Design and Manipulation of Ferroic Domains in Complex Oxide Heterostructures," Materials **12**, 3108 (2019).

[15] Y. J. Wang, Y. P. Feng, Y. L. Zhu, Y. L. Tang, L. X. Yang, M. J. Zou, W. R. Geng, M. J. Han, X. W. Guo, B. Wu, and X. L. Ma, "Polar meron lattice in strained oxide ferroelectrics," Nat. Mater. , 881–886 (2020).

[16] Y. Ivry, D. P. Chu, J. F. Scott, and C. Durkan, "Flux closure vortexlike domain structures in ferroelectric thin films," Phys. Rev. Lett. **104**, 207602 (2010).

[17] R. K. Vasudevan, Y. Matsumoto, X. Cheng, A. Imai, S. Maruyama, H. L. Xin, M. B. Okatan, S. Jesse, S. V. Kalinin, and V. Nagarajan, "Deterministic arbitrary switching of polarization in a ferroelectric thin film," Nat. Commun. **5**, 4971 (2014).

[18] E. Gradauskaite, M. Campanini, B. Biswas, C. W. Schneider, M. Fiebig, M. D. Rossell, and M. Trassin, "Robust in-plane ferroelectricity in ultrathin epitaxial aurivillius films," Adv. Mater. Interfaces **7**, 2000202 (2020).

[19]H. Béa, B. Ziegler, M. Bibes, A. Barthélémy, and P. Paruch, "Nanoscale polarization switching mechanisms in multiferroic $BiFeO_3$ thin films," J. Phys. Condens. Matter **23**, 142201 (2011).

[20]J. Guyonnet, H. Béa, and P. Paruch, "Lateral piezoelectric response across ferroelectric domain walls in thin films," J. Appl. Phys. **108**, 42002 (2010).

[21]M. Dawber, N. Stucki, C. Lichtensteiger, S. Ganglio, P. Ghosez, and J. M. Triscone, "Tailoring the properties of artificially layered ferroelectric superlattices," Adv. Mater. **19**, 4153–4159 (2007).

[22]P. Zubko, N. Stucki, C. Lichtensteiger, and J.-M. Triscone, "X-Ray Diffraction Studies of 180° Ferroelectric Domains in $PbTiO_3/SrTiO_3$ Superlattices under an Applied Electric Field," Phys. Rev. Lett. **104**, 187601 (2010).

[23]A. K. Yadav, C. T. Nelson, S. L. Hsu, Z. Hong, J. D. Clarkson, C. M. Schlepüetz, A. R. Damodaran, P. Shafer, E. Arenholz, L. R. Dedon, D. Chen, A. Vishwanath, A. M. Minor, L. Q. Chen, J. F. Scott, L. W. Martin, and R. Ramesh, "Observation of polar vortices in oxide superlattices," Nature **530**, 198–201 (2016).

[24]N. Strkalj, C. Gattinoni, A. Vogel, M. Campanini, R. Haerdi, A. Rossi, M. D. Rossell, N. A. Spaldin, M. Fiebig, and M. Trassin, "In-situ monitoring of interface proximity effects on polarization in ultrathin ferroelectrics," Nat. Commun. **11**, 5815 (2020).

[25]Y. L. Tang, Y. L. Zhu, X. L. Ma, A. Y. Borisevich, A. N. Morozovska, E. A. Eliseev, W. Y. Wang, Y. J. Wang, Y. B. Xu, Z. D. Zhang, and S. J. Pennycook, "Observation of a periodic array of flux-closure quadrants in strained ferroelectric $PbTiO_3$ films," Science **348**, 547–551 (2015).

[26]Y. Liu, Y.-J. Wang, Y.-L. Zhu, C.-H. Lei, Y.-L. Tang, S. Li, S.-R. Zhang, J. Li, and X.-L. Ma, "Large scale two-dimensional flux-closure domain arrays in oxide multilayers and their controlled growth," Nano Lett. **17**, 7258–7266 (2017).

[27]S. Li, Y. Wang, Y. Zhu, Y. Tang, Y. Liu, J. Ma, M. Han, B. Wu, and X. Ma, "Evolution of flux-closure domain arrays in oxide multilayers with misfit strain," Acta Mater. **171**, 176 – 183 (2019).

[28]Y. Sun, A. Y. Abid, C. Tan, C. Ren, M. Li, N. Li, P. Chen, Y. Li, J. Zhang, X. Zhong, J. Wang, M. Liao, K. Liu, X. Bai, Y. Zhou, D. Yu, and P. Gao, "Subunit cell–level measurement of polarization in an individual polar vortex," Science Advances **5**, eaav4355 (2019).

[29]A. L. Roitburd, "Equilibrium structure of epitaxial layers," physica status solidi (a) **37**, 329–339 (1976).

[30]V. A. Stephanovich, I. A. Luk'yanchuk, and M. G. Karkut, "Domain-Enhanced Interlayer Coupling in Ferroelectric/Paraelectric Superlattices," Phys. Rev. Lett. **94**, 47601 (2005).

[31]M. Hadjimichael, Y. Li, E. Zatterin, G. A. Chahine, M. Conroy, K. Moore, E. N. O. Connell, P. Ondrejkovic, P. Marton, J. Hlinka, U. Bangert, S. Leake, and P. Zubko, "Metal–ferroelectric supercrystals with periodically curved metallic layers," Nat. Mater. (2021), 10.1038/s41563-020-00864-6.

[32]P. Zubko, N. Jecklin, A. Torres-Pardo, P. Aguado-Puente, A. Gloter, C. Lichtensteiger, J. Junquera, O. Stéphan, and J.-M. Triscone, "Electrostatic Coupling and Local Structural Distortions at Interfaces in Ferroelectric/Paraelectric Superlattices," Nano Lett. **12**, 2846–2851 (2012).

[33]M. Hadjimichael, E. Zatterin, S. Fernandez-Peña, S. J. Leake, and P. Zubko, "Domain wall orientations in ferroelectric superlattices probed with synchrotron x-ray diffraction," Phys. Rev. Lett. **120**, 037602 (2018).

[34]S. Das, Y. L. Tang, Z. Hong, M. A. P. Gonçalves, M. R. McCarter, C. Klewe, K. X. Nguyen, F. Gómez-Ortiz, P. Shafer, E. Arenholz, V. A. Stoica, S.-L. Hsu, B. Wang, C. Ophus, J. F. Liu, C. T. Nelson, S. Saremi, B. Prasad, A. B. Mei, D. G. Schlom, J. Íñiguez, P. García-Fernández, D. A. Muller, L. Q. Chen, J. Junquera, L. W. Martin, and R. Ramesh, "Observation of room-temperature polar skyrmions," Nature **568**, 368–372 (2019).

[35]S. K. Streiffer, J. A. Eastman, D. D. Fong, C. Thompson, A. Munkholm, M. V. Ramana Murty, O. Auciello, G. R. Bai, and G. B. Stephenson, "Observation of nanoscale 180° stripe domains in ferroelectric $pbtio_3$ thin films," Phys. Rev. Lett. **89**, 067601 (2002).

[36]D. Denning, J. Guyonnet, and B. J. Rodriguez, "Applications of piezoresponse force microscopy in materials research: from inorganic ferroelectrics to biopiezoelectrics and beyond," Int. Mater. Rev. **61**, 46–70 (2016).

[37]A. Gruverman, M. Alexe, and D. Meier, "Piezoresponse force microscopy and nanoferroic phenomena," Nat. Commun. **10**, 1661 (2019).

[38]N. A. Pertsev, A. G. Zembilgotov, and A. K. Tagantsev, "Effect of Mechanical Boundary Conditions on Phase Diagrams of Epitaxial Ferroelectric Thin Films," Phys. Rev. Lett. **80**, 1988–1991 (1998).

[39]N. Balke, S. Choudhury, S. Jesse, M. Huijben, Y. H. Chu, A. P. Baddorf, L. Q. Chen, R. Ramesh, and S. V. Kalinin, "Deterministic control of ferroelastic switching in multiferroic materials," Nat. Nanotechnol. **4**, 868–875 (2009).

[40]A. Crassous, T. Sluka, A. K. Tagantsev, and N. Setter, "Polarization charge as a reconfigurable quasi-dopant in ferroelectric thin films," Nat. Nanotechnol. **10**, 614–618 (2015).

[41]L. You, Z. Chen, X. Zou, H. Ding, W. Chen, L. Chen, G. Yuan, and J. Wang, "Characterization and Manipulation of Mixed Phase Nanodomains in Highly Strained $BiFeO_3$ Thin Films," ACS Nano **6**, 5388–5394 (2012).

[42]Y.-C. Chen, Q. He, F.-N. Chu, Y.-C. Huang, J.-W. Chen, W.-I. Liang, R. K. Vasudevan, V. Nagarajan, E. Arenholz, S. V. Kalinin, and Y.-H. Chu, "Electrical Control of Multiferroic Orderings in Mixed-Phase $BiFeO_3$ Films," Adv. Mater. **24**, 3070–3075 (2012).

[43]C. Lichtensteiger, S. Fernandez-Pena, C. Weymann, P. Zubko, and J. M. Triscone, "Tuning of the depolarization field and nanodomain structure in ferroelectric thin films," Nano Lett. **14**, 4205–4211 (2014), 1507.08498.

[44]N. Strkalj, G. De Luca, M. Campanini, J. Pal, S., Schaab, C. Gattinoni, N. A. Spaldin, M. D. Rossell, M. Fiebig, and M. Trassin, "Depolarizing Field Effects in Epitaxial Capacitor Heterostructures," Phys. Rev. Lett. **123**, 147601 (2019).

[45]N. A. Pertsev and A. G. Zembilgotov, "Energetics and geometry of 90° domain structures in epitaxial ferroelectric and ferroelastic films," Journal of Applied Physics **78**, 6170–6180 (1995), https://doi.org/10.1063/1.360561.

[46]C. W. Huang, Z. H. Chen, and L. Chen, "Thickness-dependent evolutions of domain configuration and size in ferroelectric and ferroelectric-ferroelastic films," Journal of Applied Physics **113**, 094101 (2013).

Glossary

AFM atomic force microscopy

BF bright field

BFO bismuth ferrite

BTO barium titanate

DFT density functional theory

DSO dysprosium scandate

ED electric dipole

GSO gadolinium scandate

HAADF high-angle annular dark field

ISHG in-situ second harmonic generation

LSMO lanthanum-strontium manganate

PFM piezoresponse force microscopy

PLD pulsed laser deposition

PTO lead titanate

RHEED reflection high-energy electron diffraction

RSM reciprocal space mapping

SPM scanning probe microscopy

SRO strontium ruthanate

STO strontium titanate

STEM scanning transmission electron microscopy

THz-TDS terahertz time-domain spectrocopy

XPS x-ray photoelectron spectroscopy

XRD x-ray diffraction

Bibliography

[1] N. Jones. “How to stop data centres from gobbling up the world’s electricity”. *Nature* **561** (2018).

[2] A. S. G. Andrae and T. Edler. “On Global Electricity Usage of Communication Technology: Trends to 2030”. *Challenges* **6** 1 (2015).

[3] L. W. Martin, Y.-H. Chu, and R. Ramesh. “Advances in the growth and characterization of magnetic, ferroelectric, and multiferroic oxide thin films”. *Mater. Sci. Eng. R Rep.* **68** 4 (2010).

[4] A. Jain et al. “Commentary: The Materials Project: A materials genome approach to accelerating materials innovation”. *APL Mater.* **1** 1 (2013).

[5] R. Ramesh and D. G. Schlom. “Whither Oxide Electronics?” *MRS Bull.* **33** 11 (2008).

[6] J. Mannhart and D. G. Schlom. “Oxide Interfaces—An Opportunity for Electronics”. *Science* **327** 5973 (2010).

[7] J. A. Sulpizio, S. Ilani, P. Irvin, and J. Levy. “Nanoscale Phenomena in Oxide Heterostructures”. *Annu. Rev. Mater. Res.* **44** (2014).

[8] M. Lorenz et al. “The 2016 oxide electronic materials and oxide interfaces roadmap”. *J. Phys. D. Appl. Phys.* **49** 43 (2016).

[9] M. Coll et al. “Towards Oxide Electronics: a Roadmap”. *Appl. Surf. Sci.* **482** (2019).

[10] J. Valasek. “Piezoelectric and allied phenomena in Rochelle salt”. *Phys. Rev.* **17** 4 (1921).

[11] O. Auciello, J. F. Scott, and R. Ramesh. “The Physics of Ferroelectric Memories”. *Phys. Today* **51** 7 (1998).

[12] J. F. Scott and C. A. de Araujo. “Ferroelectric Memories”. *Science* **246** 4936 (1989).

[13] D. S. Jeong, R. Thomas, R. S. Katiyar, J. F. Scott, H. Kohlstedt, A. Petraru, and C. S. Hwang. “Emerging memories: resistive switching mechanisms and current status”. *Reports Prog. Phys.* **75** 7 (2012).

[14] J. F. Scott. “Applications of Modern Ferroelectrics”. *Science* **315** 5814 (2007).

[15] J. F. Scott. “Nanoferroelectrics: statics and dynamics.” *J. Phys. Condens. Matter* **18** 17 (2006).

[16] P. Zubko, S. Gariglio, M. Gabay, P. Ghosez, and J.-M. Triscone. “Interface Physics in Complex Oxide Heterostructures”. *Annu. Rev. Condens. Matter Phys.* **2** (2011).

[17] G. De Luca, N. Strkalj, S. Manz, C. Bouillet, M. Fiebig, and M. Trassin. “Nanoscale design of polarization in ultrathin ferroelectric heterostructures”. *Nat. Commun.* **8** 1419 (2017).

[18] J. Nordlander, G. De Luca, N. Strkalj, M. Fiebig, and M. Trassin. “Probing Ferroic States in Oxide Thin Films Using Optical Second Harmonic Generation”. *Appl. Sci.* **8** 4 (2018).

[19] N. Setter et al. “Ferroelectric thin films: Review of materials, properties, and applications”. *J. Appl. Phys.* **100** 5 (2006).

[20] L. W. Martin and A. M. Rappe. “Thin-film ferroelectric materials and their applications”. *Nat. Rev. Mater.* **2** 2 (2017).

[21] I. P. Batra, P. Wurfel, and B. D. Silverman. “Phase Transition, Stability, and Depolarization Field in Ferroelectric Thin Films”. *Phys. Rev. B* **8** 7 (1973).

[22] A. Kopal, T. Bahnik, and J. Fousek. “Domain formation in thin ferroelectric films: The role of depolarization energy”. *Ferroelectrics* **202** 1 (1997).

[23] V. Nagarajan et al. “Scaling of structure and electrical properties in ultrathin epitaxial ferroelectric heterostructures”. *J. Appl. Phys.* **100** 5 (2006).

[24] P. Zubko, H. Lu, C.-W. Bark, X. Martí, J. Santiso, C.-B. Eom, G. Catalan, and A. Gruverman. “On the persistence of polar domains in ultrathin ferroelectric capacitors”. *J. Phys. Condens. Matter* **29** 28 (2017).

[25] L. Xie et al. “Giant Ferroelectric Polarization in Ultrathin Ferroelectrics via Boundary-Condition Engineering”. *Adv. Mater.* **29** 30 (2017).

[26] H. Béa et al. “Influence of parasitic phases on the properties of BiFeO$_3$ epitaxial thin films”. *Appl. Phys. Lett.* **87** 7 (2005).

[27] C. Weymann, C. Lichtensteiger, S. Fernandez-Peña, L. R. Dedon, L. W. Martin, A. B. Naden, J.-M. Triscone, and P. Paruch. “Full control of polarisation in ferroelectric thin films through growth temperature defect engineering”. *Adv. Electron. Mater.* (2020).

[28] I. S. Vorotiahin, A. N. Morozovska, and Y. A. Genenko. “Hierarchy of domain reconstruction processes due to charged defect migration in acceptor doped ferroelectrics”. *Acta Mater.* **184** (2020).

[29] C. Lichtensteiger, S. Fernandez-Peña, C. Weymann, P. Zubko, and J.-M. M. Triscone. “Tuning of the depolarization field and nanodomain structure in ferroelectric thin films”. *Nano Lett.* **14** 8 (2014).

[30] N. Strkalj, G. De Luca, M. Campanini, S. Pal, J. Schaab, C. Gattinoni, N. A. Spaldin, M. D. Rossell, M. Fiebig, and M. Trassin. “Depolarizing Field Effects in Epitaxial Capacitor Heterostructures”. *Phys. Rev. Lett.* **123** 14 (2019).

[31] P. Yu, Y.-H. Chu, and R. Ramesh. “Oxide interfaces: pathways to novel phenomena”. *Mater. Today* **15** 7 (2012).

[32] R. V. Wang et al. “Reversible Chemical Switching of a Ferroelectric Film”. *Phys. Rev. Lett.* **102** 047601 (2009).

[33] M. J. Highland, T. T. Fister, D. D. Fong, P. H. Fuoss, C. Thompson, J. A. Eastman, S. K. Streiffer, and G. B. Stephenson. “Equilibrium polarization of ultrathin $PbTiO_3$ with surface compensation controlled by oxygen partial pressure”. *Phys. Rev. Lett.* **107** 187602 (2011).

[34] J. Shin, V. B. Nascimento, G. Geneste, J. Rundgren, E. W. Plummer, B. Dkhil, S. V. Kalinin, and A. P. Baddorf. “Atomistic Screening Mechanism of Ferroelectric Surfaces: An In Situ Study of the Polar Phase in Ultrathin $BaTiO_3$ Films Exposed to H_2O”. *Nano Lett.* **9** 11 (2009).

[35] Y. Tian et al. “Water printing of ferroelectric polarization”. *Nat. Commun.* **9** 3809 (2018).

[36] N. Domingo, I. Gaponenko, K. Cordero-Edwards, N. Stucki, V. Perez Dieste, C. Escudero, E. Pach, A. Verdaguer, and P. Patrycja. “Surface Charged Species and Electrochemistry of Ferroelectric Thin Films”. *Nanoscale* **11** (2019).

[37] Y. L. Tang et al. “Observation of a periodic array of flux-closure quadrants in strained ferroelectric $PbTiO_3$ films”. *Science* **348** 6234 (2015).

[38] A. K. Yadav et al. “Observation of polar vortices in oxide superlattices”. *Nature* **530** 7589 (2016).

[39] Z. Hong et al. “Stability of Polar Vortex Lattice in Ferroelectric Superlattices”. *Nano Lett.* **17** 4 (2017).

[40] A. R. Damodaran et al. “Phase coexistence and electric-field control of toroidal order in oxide superlattices”. *Nat. Mater.* **16** 1003 (2017).

[41] S. Das et al. “Observation of room-temperature polar skyrmions”. *Nature* **568** 7752 (2019).

[42] V. A. Stoica et al. “Optical creation of a supercrystal with three-dimensional nanoscale periodicity”. *Nat. Mater.* **18** 4 (2019).

[43] Y. Sun et al. “Subunit cell–level measurement of polarization in an individual polar vortex”. *Sci. Adv.* **5** 11 (2019).

[44] S.-L. Hsu, M. R. McCarter, C. Dai, Z. Hong, L.-Q. Chen, C. T. Nelson, L. W. Martin, and R. Ramesh. “Emergence of the Vortex State in Confined Ferroelectric Heterostructures”. *Adv. Mater.* **31** 36 (2019).

[45] Y. J. Wang et al. “Polar meron lattice in strained oxide ferroelectrics”. *Nat. Mater.* (2020).

[46] V. K. Wadhawan. *Introduction to ferroic materials*. Gordon & Breach, 2000.

[47] C. Kittel. *Introduction to Solid State Physics*. Wiley, 2004.

[48] M. E. Lines and A. M. Glass. *Principles and Applications of Ferroelectrics and Related Materials*. Oxford University Press, 2001.

[49] W. Cochran. “Crystal stability and the theory of ferroelectricity”. *Adv. Phys.* **9** 36 (1960).

[50] J. F. Scott. “Soft-mode spectroscopy: Experimental studies of structural phase transitions”. *Rev. Mod. Phys.* **46** 1 (1974).

[51] L. D. Landau and E. M. Lifshitz. “To the Theory of Magnetic Permeability Dispersion in Ferromagnetic Solids”. *Sov. Phys* **8** (1935).

[52] C. Kittel. “Theory of the Structure of Ferromagnetic Domains in Films and Small Particles”. *Phys. Rev.* **70** 11-12 (1946).

[53] C. Kittel. “Physical Theory of Ferromagnetic Domains”. *Rev. Mod. Phys.* **21** 4 (1949).

[54] T. Mitsui and J. Furuichi. “Domain Structure of Rochelle Salt and $\mathrm{KH_2PO_4}$”. *Phys. Rev.* **90** 2 (1953).

[55] A. L. Roitburd. “Equilibrium structure of epitaxial layers”. *Phys. status solidi* **37** 1 (1976).

[56] G. Catalan, J. F. Scott, A. Schilling, and J. M. Gregg. “Wall thickness dependence of the scaling law for ferroic stripe domains”. *J. Phys. Condens. Matter* **19** 2 (2006).

[57] A. Schilling, T. B. Adams, R. M. Bowman, J. M. Gregg, G. Catalan, and J. F. Scott. “Scaling of domain periodicity with thickness measured in BaTi$\mathrm{O_3}$ single crystal lamellae and comparison with other ferroics”. *Phys. Rev. B* **74** 2 (2006).

[58] G. Catalan, I. Lukyanchuk, A. Schilling, J. Gregg, and J. Scott. “Effect of wall thickness on the ferroelastic domain size of BaTi$\mathrm{O_3}$”. *J. Mater. Sci.* **44** 19 (2009).

[59] N. A. Pertsev and A. G. Zembilgotov. “Energetics and geometry of 90° domain structures in epitaxial ferroelectric and ferroelastic films”. *J. Appl. Phys.* **78** 10 (1995).

[60] C. W. Huang, Z. H. Chen, and L. Chen. “Thickness-dependent evolutions of domain configuration and size in ferroelectric and ferroelectric-ferroelastic films”. *J. Appl. Phys.* **113** 9 (2013).

[61] R. E. Cohen. “Origin of ferroelectricity in perovskite oxides”. *Nature* **358** 6382 (1992).

[62] Z.-X. Chen, Y. Chen, and Y.-S. Jiang. “DFT Study on Ferroelectricity of $BaTiO_3$”. *J. Phys. Chem. B* **105** 24 (2001).

[63] Z.-X. Chen, Y. Chen, and Y.-S. Jiang. “Comparative Study of ABO_3 Perovskite Compounds. 1. $ATiO_3$ (A = Ca, Sr, Ba, and Pb) Perovskites”. *J. Phys. Chem. B* **106** 39 (2002).

[64] C.-L. Jia, V. Nagarajan, J.-Q. He, L. Houben, T. Zhao, R. Ramesh, K. Urban, and R. Waser. “Unit-cell scale mapping of ferroelectricity and tetragonality in epitaxial ultrathin ferroelectric films”. *Nat. Mater.* **6** 1 (2007).

[65] U. V. Waghmare and K. M. Rabe. “Ab initio statistical mechanics of the ferroelectric phase transition in $PTiO_3$”. *Phys. Rev. B* **55** 10 (1997).

[66] S. Kisaka, S. Ikegami, and H. Sasaki. “Dielectric Properties of Mixed Crystals of Barium-Strontium Titanate”. *J. Phys. Soc. Jpn.* **14** 12 (1959).

[67] M. G. Harwood, P. Popper, and D. F. Rushman. “Curie Point of Barium Titanate”. *Nature* **160** 4054 (1947).

[68] A. M. Glazer and S. A. Mabud. “Powder profile refinement of lead zirconate titanate at several temperatures. II. Pure $PbTiO_3$”. *Acta Crystallogr. Sect. B* **34** 4 (1978).

[69] M. Kupriyanov, D. Kovtun, A. Zakharov, G. Kushlyan, S. Yagunov, R. Kolesova, and K. Abdulvakhidov. “Summary data on ferroelectric PbTiO3 structure”. *Phase Transitions* **64** 3 (1998).

[70] A. M. Bratkovsky and A. P. Levanyuk. “Abrupt Appearance of the Domain Pattern and Fatigue of Thin Ferroelectric Films”. *Phys. Rev. Lett.* **84** (2000).

[71] D. D. Fong, G. B. Stephenson, S. K. Streiffer, J. A. Eastman, O. Auciello, P. H. Fuoss, and C. Thompson. “Ferroelectricity in Ultrathin Perovskite Films”. *Science* **304** 2001 (2004).

[72] J. Junquera and P. Ghosez. “Critical thickness for ferroelectricity in perovskite ultrathin films”. *Nature* **422** 6931 (2003).

[73] D. G. Schlom, L.-Q. Chen, C.-B. Eom, K. M. Rabe, S. K. Streiffer, and J.-M. Triscone. “Strain tuning of ferroelectric thin films”. *Annu. Rev. Mater. Res.* **37** (2007).

[74] P. Yu et al. “Interface control of bulk ferroelectric polarization”. *PNAS* **109** 25 (2012).

[75] N. Strkalj, E. Gradauskaite, J. Nordlander, and M. Trassin. “Design and Manipulation of Ferroic Domains in Complex Oxide Heterostructures”. *Materials* **12** 19 (2019).

[76] M. Stengel and N. A. Spaldin. “Origin of the dielectric dead layer in nanoscale capacitors”. *Nature* **443** 7112 (2006).

[77] M. Stengel, P. Aguado-Puente, N. A. Spaldin, and J. Junquera. “Band alignment at metal/ferroelectric interfaces: Insights and artifacts from first principles”. *Phys. Rev. B* **83** 23 (2011).

[78] C. Lichtensteiger, M. Dawber, N. Stucki, J.-M. Triscone, J. Hoffman, J.-B. Yau, C. H. Ahn, L. Despont, and P. Aebi. “Monodomain to polydomain transition in ferroelectric $PbTiO_3$ thin films with $La_{0.67}Sr_{0.33}MnO_3$ electrodes”. *Appl. Phys. Lett.* **90** 5 (2007).

[79] R. R. Mehta, B. D. Silverman, and J. T. Jacobs. “Depolarization fields in thin ferroelectric films”. *J. Appl. Phys.* **44** 8 (1973).

[80] M. Dawber, P. Chandra, P. B. Littlewood, and J. F. Scott. “Depolarization corrections to the coercive field in thin-film ferroelectrics”. *J. Phys. Condens. Matter* **15** 24 (2003).

[81] C. T. Black and J. J. Welser. “Electric-field penetration into metals: consequences for high-dielectric-constant capacitors”. *IEEE Trans. Electron Devices* **46** 4 (1999).

[82] M. Stengel, D. Vanderbilt, and N. A. Spaldin. “Enhancement of ferroelectricity at metal–oxide interfaces”. *Nat. Mater.* **8** 5 (2009).

[83] A. M. Bratkovsky and A. P. Levanyuk. “Continuous Theory of Ferroelectric States in Ultrathin Films with Real Electrodes”. *J. Comput. Theor. Nanosci.* **6** 3 (2009).

[84] D. D. Fong et al. “Stabilization of Monodomain Polarization in Ultrathin $PbTiO_3$ Films”. *Phys. Rev. Lett.* **96** (2006).

[85] G. B. Stephenson and M. J. Highland. “Equilibrium and stability of polarization in ultrathin ferroelectric films with ionic surface compensation”. *Phys. Rev. B* **84** (2011).

[86] R. Ramesh and V. G. Keramidas. “Metal-Oxide Heterostructures”. *Annu. Rev. Mater. Sci.* **25** 1 (1995).

[87] C. Gattinoni, N. Strkalj, R. Haerdi, M. Fiebig, M. Trassin, and N. A. Spaldin. “Interface and surface stabilization of thepolarization in ferroelectric thin films”. *PNAS* **117** 46 (2020).

[88] M. Ohring. *Materials Science of Thin Films*. Academic Press, 2002.

[89] M. D. Biegalski, J. H. Haeni, S. Trolier-McKinstry, D. G. Schlom, C. D. Brandle, and A. J. V. Graitis. “Thermal expansion of the new perovskite substrates $DyScO_3$ and $GdScO_3$”. *J. Mater. Res.* **20** 4 (2005).

[90] E. Langenberg, H. Paik, E. H. Smith, H. P. Nair, I. Hanke, S. Ganschow, G. Catalan, N. Domingo, and D. G. Schlom. “Strain-Engineered Ferroelastic Structures in $PbTiO_3$ Films and Their Control by Electric Fields”. *ACS Appl. Mater. Interfaces* **12** 18 (2020).

[91] C. Ederer and N. A. Spaldin. “Effect of Epitaxial Strain on the Spontaneous Polarization of Thin Film Ferroelectrics”. *Phys. Rev. Lett.* **95** 25 (2005).

[92] Y. L. Li, S. Y. Hu, Z. K. Liu, and L. Q. Chen. “Effect of substrate constraint on the stability and evolution of ferroelectric domain structures in thin films”. *Acta Mater.* **50** 2 (2002).

[93] N. A. Pertsev, A. K. Tagantsev, and N. Setter. “Phase transitions and strain-induced ferroelectricity in $SrTiO_3$ epitaxial thin films”. *Phys. Rev. B* **61** 2 (2000).

[94] J. H. Haeni et al. “Room-temperature ferroelectricity in strained SrTiO3”. *Nature* **430** 7001 (2004).

[95] M. Tyunina, J. Narkilahti, M. Plekh, R. Oja, R. M. Nieminen, A. Dejneka, and V. Trepakov. “Evidence for Strain-Induced Ferroelectric Order in Epitaxial Thin-Film $KTaO_3$”. *Phys. Rev. Lett.* **104** 22 (2010).

[96] A. L. Roytburd. “Thermodynamics of polydomain heterostructures. I. Effect of macrostresses”. *J. Appl. Phys.* **83** 1 (1998).

[97] T. Tomio, H. Miki, H. Tabata, T. Kawai, and S. Kawai. “Control of electrical conductivity in laser deposited $SrTiO_3$ thin films with Nb doping”. *J. Appl. Phys.* **76** 10 (1994).

[98] J. B. Clark, P. W. Richter, and L. Toit. “High-pressure synthesis of $YScO_3$, $HoScO_3$, $ErScO_3$, and $TmScO_3$, and a reevaluation of the lattice constants of the rare earth scandates”. *J. Solid State Chem.* **23** 1 (1978).

[99] S. N. Amanyan, P. A. Arsen’ev, K. S. Bagdasarov, A. M. Kevorkov, D. I. Korolev, A. V. Potemkin, and V. V. Femin. “Synthesis and examination of $GdScO_3$ single crystals activated by Nd^{3+}”. *J. Appl. Spectrosc.* **38** 3 (1983).

[100] W. Wersing, W. Heywang, H. Beige, and H. Thomann. “The Role of Ferroelectricity for Piezoelectric Materials”. In: *Piezoelectricity*. Springer Berlin Heidelberg, 2008.

[101] C. R. Bowen, H. A. Kim, P. M. Weaver, and S. Dunn. “Piezoelectric and ferroelectric materials and structures for energy harvesting applications”. *Energy Environ. Sci.* **7** 1 (2014).

[102] P. Ferraro, S. Grilli, and P. D. Natale, eds. *Ferroelectric Crystals for Photonic Applications*. Springer Berlin Heidelberg, 2009.

[103] S. Abel et al. “Large Pockels effect in micro- and nanostructured barium titanate integrated on silicon”. *Nat. Mater.* **18** 1 (2019).

[104] K. Yao, B. K. Gan, M. Chen, and S. Shannigrahi. “Large photo-induced voltage in a ferroelectric thin film with in-plane polarization”. *Appl. Phys. Lett.* **87** 21 (2005).

[105] S. Y. Yang et al. “Above-bandgap voltages from ferroelectric photovoltaic devices”. *Nat. Nanotechnol.* **5** 2 (2010).

[106] E. Y. Tsymbal and H. Kohlstedt. “Tunneling Across a Ferroelectric”. *Science* **313** 5784 (2006).

[107] R. Oligschlaeger, R. Waser, R. Meyer, S. Karthäuser, and R. Dittmann. “Resistive switching and data reliability of epitaxial $(Ba,Sr)TiO_3$ thin films”. *Appl. Phys. Lett.* **88** 4 (2006).

[108] H. Kohlstedt, A. Petraru, K. Szot, A. Rüdiger, P. Meuffels, H. Haselier, R. Waser, and V. Nagarajan. “Method to distinguish ferroelectric from nonferroelectric origin in case of resistive switching in ferroelectric capacitors”. *Appl. Phys. Lett.* **92** 6 (2008).

[109] A. Q. Jiang, Y. Y. Lin, and T. A. Tang. “Charge injection and polarization fatigue in ferroelectric thin films”. *J. Appl. Phys.* **102** 7 (2007).

[110] X. Chen, G. Wu, H. Zhang, N. Qin, T. Wang, F. Wang, W. Shi, and D. Bao. “Nonvolatile bipolar resistance switching effects in multiferroic $BiFeO_3$ thin films on $LaNiO_3$-electrodized Si substrates”. *Appl. Phys. A* **100** 4 (2010).

[111] C. Wang, K.-j. Jin, Z.-t. Xu, L. Wang, C. Ge, H.-b. Lu, H.-z. Guo, M. He, and G.-z. Yang. “Switchable diode effect and ferroelectric resistive switching in epitaxial $BiFeO_3$ thin films”. *Appl. Phys. Lett.* **98** 19 (2011).

[112] A. M. Ionescu. “Nanoelectronics: Ferroelectric devices show potential”. *Nat. Nanotechnol.* **7** 2 (2012).

[113] V. Garcia and M. Bibes. “Ferroelectric tunnel junctions for information storage and processing”. *Nat. Commun.* **5** 1 (2014).

[114] J. Wang, D. Pesquera, R. Mansell, S. van Dijken, R. P. Cowburn, M. Ghidini, and N. D. Mathur. “Giant non-volatile magnetoelectric effects via growth anisotropy in $Co_{40}Fe_{40}B_{20}$ films on PMN-PT substrates”. *Appl. Phys. Lett.* **114** 9 (2019).

[115] S. Mathews, R. Ramesh, T. Venkatesan, and J. Benedetto. “Ferroelectric Field Effect Transistor Based on Epitaxial Perovskite Heterostructures”. *Science* **276** 5310 (1997).

[116] H. Shen, J. Liu, K. Chang, and L. Fu. “In-Plane Ferroelectric Tunnel Junction”. *Phys. Rev. Appl.* **11** 2 (2019).

[117] A. Kakekhani and S. Ismail-Beigi. “Ferroelectric-Based Catalysis: Switchable Surface Chemistry”. *ACS Catal.* **5** 8 (2015).

[118] A. Kakekhani and S. Ismail-Beigi. “Ferroelectric oxide surface chemistry: water splitting via pyroelectricity”. *J. Mater. Chem. A* **4** 14 (2016).

[119] B. O. Alawode and A. M. Kolpak. “$PbTiO_3$(001) Capped with ZnO(1120): An ab Initio Study of Effect of Substrate Polarization on Interface Composition and CO_2 Dissociation”. *J. Phys. Chem. Lett.* **7** 7 (2016).

[120] L. C. Tănase, N. G. Apostol, L. E. Abramiuc, C. A. Tache, L. Hrib, L. Trupină, L. Pintilie, and C. M. Teodorescu. “Ferroelectric triggering of carbon monoxide adsorption on lead zirco-titanate (001) surfaces”. *Sci. Rep.* **6** 1 (2016).

[121] I. Efe, C. Gattinoni, and N. A. Spaldin. “On the happiness of ferroelectric surfaces and its role in water dissociation: the example of bismuth ferrite”. *arXiv:2010.14895v1* (2020).

[122] P. Zubko, J. C. Wojdeł, M. Hadjimichael, S. Fernandez-Peña, A. Sené, I. Luk'yanchuk, J.-M. Triscone, and J. Íñiguez. “Negative capacitance in multidomain ferroelectric superlattices”. *Nature* **534** 7608 (2016).

[123] A. I. Khan, K. Chatterjee, B. Wang, S. Drapcho, L. You, C. Serrao, S. R. Bakaul, R. Ramesh, and S. Salahuddin. “Negative capacitance in a ferroelectric capacitor”. *Nat. Mater.* **14** 2 (2015).

[124] A. Chanthbouala et al. “A ferroelectric memristor”. *Nat. Mater.* **11** 10 (2012).

[125] S. Oh, H. Hwang, and I. K. Yoo. “Ferroelectric materials for neuromorphic computing”. *APL Mater.* **7** 9 (2019).

[126] S. Li, Y. L. Zhu, Y. J. Wang, Y. L. Tang, Y. Liu, S. R. Zhang, J. Y. Ma, and X. L. Ma. “Periodic arrays of flux-closure domains in ferroelectric thin films with oxide electrodes”. *Appl. Phys. Lett.* **111** 5 (2017).

[127] S. Estandía, F. Sánchez, M. F. Chisholm, and J. Gázquez. “Rotational polarization nanotopologies in $\mathrm{BaTiO_3}$/$\mathrm{SrTiO_3}$ superlattices”. *Nanoscale* **11** 44 (2019).

[128] S. Das, Z. Hong, M. McCarter, P. Shafer, Y.-T. Shao, D. A. Muller, L. W. Martin, and R. Ramesh. “A new era in ferroelectrics”. *APL Mater.* **8** 12 (2020).

[129] S. Chen et al. “Recent Progress on Topological Structures in Ferroic Thin Films and Heterostructures”. *Adv. Mater.* **n/a** n/a (2020).

[130] W. Geng et al. “Rhombohedral–Orthorhombic Ferroelectric Morphotropic Phase Boundary Associated with a Polar Vortex in BiFeO3 Films”. *ACS Nano* **12** 11 (2018).

[131] A. B. Mei, R. Ramesh, and D. G. Schlom. *Discovery of Ordered Vortex Phase in Multiferroic Oxide Superlattices.* 2018.

[132] P. Chen et al. “Atomic imaging of mechanically induced topological transition of ferroelectric vortices”. eng. *Nat. Commun.* **11** 1 (2020).

[133] S. Salahuddin and S. Datta. “Use of negative capacitance to provide voltage amplification for low power nanoscale devices”. *Nano Lett.* **8** 2 (2008).

[134] A. K. Yadav et al. “Spatially resolved steady-state negative capacitance”. *Nature* **565** 7740 (2019).

[135] J. Iñiguez, P. Zubko, I. Luk'yanchuk, and A. Cano. “Ferroelectric negative capacitance”. *Nat. Rev. Mater.* **4** 4 (2019).

[136] I. Luk'yanchuk, Y. Tikhonov, A. Sené, A. Razumnaya, and V. M. Vinokur. “Harnessing ferroelectric domains for negative capacitance”. *Commun. Phys.* **2** 1 (2019).

[137] D. G. Schlom, L.-Q. Chen, X. Pan, A. Schmehl, and M. A. Zurbuchen. “A thin film approach to engineering functionality into oxides”. *J. Am. Ceram. Soc.* **91** 8 (2008).

[138] D. P. Norton. *Pulsed Laser Deposition of Complex Materials: Progress Toward Applications*. Wiley, 2006.

[139] D. B. Chrisey and G. K. Hubler. *Pulsed laser deposition of thin films*. Wiley New York, 1994.

[140] G. J. H. M. Rijnders, G. Koster, D. H. A. Blank, and H. Rogalla. "In situ monitoring during pulsed laser deposition of complex oxides using reflection high energy electron diffraction under high oxygen pressure". *Appl. Phys. Lett.* **70** 14 (1997).

[141] G. Koster and A. J. Rijnders. "Reflection high-energy electron diffraction (RHEED) for in situ characterization of thin film growth". In: *situ Charact. thin Film growth*. Woodhead Publishing, 2011.

[142] J. Choi, C. B. Eom, G. Rijnders, H. Rogalla, and D. H. A. Blank. "Growth mode transition from layer by layer to step flow during the growth of heteroepitaxial $SrRuO_3$ on (001) $SrTiO_3$". *Appl. Phys. Lett.* **79** 10 (2001).

[143] P. S. Halasyamani and K. R. Poeppelmeier. "Noncentrosymmetric Oxides". *Chem. Mater.* **10** 10 (1998).

[144] R. W. Boyd. *Nonlinear Optics*. Academic Press, 2008.

[145] Y. R. Shen. *The Principles of Nonlinear Optics*. Wiley-Interscience, 2002.

[146] A. Prylepa et al. "Material characterisation with methods of nonlinear optics". *J. Phys. D. Appl. Phys.* **51** 4 (2018).

[147] S. A. Denev, T. T. A. Lummen, E. Barnes, A. Kumar, and V. Gopalan. "Probing ferroelectrics using optical second harmonic generation". *J. Am. Ceram. Soc.* **94** 9 (2011).

[148] R. R. Birss. *Symmetry and magnetism*. North-Holland Publishing Company, 1964.

[149] V. Gopalan and R. Raj. "Domain Structure-Second Harmonic Generation Correlation in Potassium Niobate Thin Films Deposited on a Strontium Titanate Substrate". *J. Am. Ceram. Soc.* **79** 12 (1996).

[150] C. J. Roh, S. Y. Hamh, C.-S. Woo, K.-E. Kim, C.-H. Yang, and J. S. Lee. "Ferroelectric domain states of a tetragonal $BiFeO_3$ thin film investigated by second harmonic generation microscopy". *Nanoscale Res. Lett.* **12** 353 (2017).

[151] M. Trassin, G. D. Luca, S. Manz, M. Fiebig, G. De Luca, S. Manz, and M. Fiebig. "Probing Ferroelectric Domain Engineering in $BiFeO_3$ Thin Films by Second Harmonic Generation". *Adv. Mater.* **27** 33 (2015).

[152] Y. Zhang et al. "Characterization of domain distributions by second harmonic generation in ferroelectrics". *npj Comput. Mater.* **4** 1 (2018).

[153] J.-s. Wang, K.-j. Jin, H.-z. Guo, J.-x. Gu, Q. Wan, X. He, X.-l. Li, X.-l. Xu, and G.-z. Yang. "Evolution of structural distortion in $BiFeO_3$ thin films probed by second-harmonic generation". *Sci. Rep.* **6** (2016).

[154] A. Kumar, S. Denev, R. J. Zeches, E. Vlahos, N. J. Podraza, A. Melville, D. G. Schlom, R. Ramesh, and V. Gopalan. “Probing mixed tetragonal/rhombohedral-like monoclinic phases in strained bismuth ferrite films by optical second harmonic generation”. *Appl. Phys. Lett.* **97** 11 (2010).

[155] N. Strkalj, C. Gattinoni, A. Vogel, M. Campanini, R. Haerdi, A. Rossi, M. D. Rossell, N. A. Spaldin, M. Fiebig, and M. Trassin. “In-situ monitoring of interface proximity effects on polarization in ultrathin ferroelectrics”. *Nat. Commun.* **11** 5815 (2020).

[156] M. F. Sarott, M. Fiebig, and M. Trassin. “Tracking ferroelectric domain formation during epitaxial growth of $\mathrm{PbTiO_3}$ films”. *Appl. Phys. Lett.* **117** 13 (2020).

[157] S. Cherifi-Hertel, H. Bulou, R. Hertel, G. Taupier, K. D. Dorkenoo, C. Andreas, J. Guyonnet, I. Gaponenko, K. Gallo, and P. Paruch. “Non-Ising and chiral ferroelectric domain walls revealed by nonlinear optical microscopy”. *Nat. Commun.* **8** (2017).

[158] G. De Luca, M. D. Rossell, J. Schaab, N. Viart, M. Fiebig, and M. Trassin. “Domain Wall Architecture in Tetragonal Ferroelectric Thin Films”. *Adv. Mater.* **29** 7 (2017).

[159] R. M. Corn and D. A. Higgins. “Optical second harmonic generation as a probe of surface chemistry”. *Chem. Rev.* **94** 1 (1994).

[160] G. Lüpke. “Characterization of semiconductor interfaces by second-harmonic generation”. *Surf. Sci. Rep.* **35** 3 (1999).

[161] T. Stehlin, M. Feller, P. Guyot-Sionnest, and Y. R. Shen. “Optical second-harmonic generation as a surface probe for noncentrosymmetric media”. *Opt. Lett.* **13** 5 (1988).

[162] V. Jähnke, U. Conrad, J. Güdde, and E. Matthias. “SHG investigations of the magnetization of thin Ni and Co films on Cu(001)”. *Appl. Phys. B* **68** 3 (1999).

[163] D. D. Fong and C. Thompson. “In situ synchrotron x-ray studies of ferroelectric thin films”. *Annu. Rev. Mater. Res.* **36** 1 (2006).

[164] J. Sinsheimer, S. J. Callori, B. Ziegler, B. Bein, P. V. Chinta, A. Ashrafi, R. L. Headrick, and M. Dawber. “In-situ x-ray diffraction study of the growth of highly strained epitaxial $\mathrm{BaTiO_3}$ thin films”. *Appl. Phys. Lett.* **103** 24 (2013).

[165] B. Bein, H.-C. Hsing, S. J. Callori, J. Sinsheimer, P. V. Chinta, R. L. Headrick, and M. Dawber. “In situ X-ray diffraction and the evolution of polarization during the growth of ferroelectric superlattices”. *Nat. Commun.* **6** (2015).

[166] K. J. Choi et al. “Enhancement of Ferroelectricity in Strained $\mathrm{BaTiO_3}$ Thin Films”. *Science* **306** 5698 (2004).

[167] A. R. Damodaran, E. Breckenfeld, Z. Chen, S. Lee, and L. W. Martin. “Enhancement of ferroelectric curie temperature in $BaTiO_3$ films via strain-induced defect dipole alignment”. *Adv. Mater.* **26** 36 (2014).

[168] S. K. Streiffer, J. A. Eastman, D. D. Fong, C. Thompson, A. Munkholm, M. V. Ramana Murty, O. Auciello, G. R. Bai, and G. B. Stephenson. “Observation of Nanoscale 180° Stripe Domains in Ferroelectric $PbTiO_3$ Thin Films”. *Phys. Rev. Lett.* **89** (2002).

[169] G. Catalan, A. Lubk, A. H. G. Vlooswijk, E. Snoeck, C. Magen, A. Janssens, G. Rispens, G. Rijnders, D. H. A. Blank, and B. Noheda. “Flexoelectric rotation of polarization in ferroelectric thin films”. *Nat. Mater.* **10** 12 (2011).

[170] H. Lu, C.-W. Bark, D. Esque de los Ojos, J. Alcala, C. B. Eom, G. Catalan, and A. Gruverman. “Mechanical Writing of Ferroelectric Polarization”. *Science* **336** 6077 (2012).

[171] S. M. Park, B. Wang, S. Das, S. C. Chae, J.-S. Chung, J.-G. Yoon, L.-Q. Chen, S. M. Yang, and T. W. Noh. “Selective control of multiple ferroelectric switching pathways using a trailing flexoelectric field”. *Nat. Nanotechnol.* **13** 5 (2018).

[172] R. Roth, M. Koch, J. Schaab, M. Lilienblum, F. Syrowatka, T. Band, T. Thurn-Albrecht, and K. Dörr. “Aligning in-plane polarization multiplies piezoresponse in P(VDF-TrFE) films on graphite”. *New J. Phys.* **20** 10 (2018).

[173] D. Denning, J. Guyonnet, and B. J. Rodriguez. “Applications of piezoresponse force microscopy in materials research: from inorganic ferroelectrics to biopiezoelectrics and beyond”. *Int. Mater. Rev.* **61** 1 (2016).

[174] A. Gruverman, M. Alexe, and D. Meier. “Piezoresponse force microscopy and nanoferroic phenomena”. *Nat. Commun.* **10** 1 (2019).

[175] N. Balke, S. Choudhury, S. Jesse, M. Huijben, Y. H. Chu, A. P. Baddorf, L. Q. Chen, R. Ramesh, and S. V. Kalinin. “Deterministic control of ferroelastic switching in multiferroic materials”. *Nat. Nanotechnol.* **4** 12 (2009).

[176] A. Crassous, T. Sluka, A. K. Tagantsev, and N. Setter. “Polarization charge as a reconfigurable quasi-dopant in ferroelectric thin films”. *Nat. Nanotechnol.* **10** 7 (2015).

[177] S. Matzen, O. Nesterov, G. Rispens, J. A. Heuver, M. Biegalski, H. M. Christen, and B. Noheda. “Super switching and control of in-plane ferroelectric nanodomains in strained thin films”. *Nat. Commun.* **5** 4415 (2014).

[178] R. K. Vasudevan, Y. Matsumoto, X. Cheng, A. Imai, S. Maruyama, H. L. Xin, M. B. Okatan, S. Jesse, S. V. Kalinin, and V. Nagarajan. “Deterministic arbitrary switching of polarization in a ferroelectric thin film”. *Nat. Commun.* **5** 4971 (2014).

[179] L. You, Z. Chen, X. Zou, H. Ding, W. Chen, L. Chen, G. Yuan, and J. Wang. "Characterization and Manipulation of Mixed Phase Nanodomains in Highly Strained $BiFeO_3$ Thin Films". *ACS Nano* **6** 6 (2012).

[180] Y.-C. Chen et al. "Electrical Control of Multiferroic Orderings in Mixed-Phase $BiFeO_3$ Films". *Adv. Mater.* **24** 22 (2012).

[181] M. Birkholz. *Principles of X-ray Diffraction*. Wiley, 2005.

[182] C. Lichtensteiger, J.-M. Triscone, J. Junquera, and P. Ghosez. "Ferroelectricity and Tetragonality in Ultrathin $PbTiO_3$ Films". *Phys. Rev. Lett.* **94** 4 (2005).

[183] M. Dawber, C. Lichtensteiger, M. Cantoni, M. Veithen, P. Ghosez, K. Johnston, K. M. Rabe, and J.-M. Triscone. "Unusual Behavior of the Ferroelectric Polarization in $PbTiO_3/SrTiO_3$ Superlattices". *Phys. Rev. Lett.* **95** 17 (2005).

[184] Y. Li, V. Nagarajan, S. Aggarwal, R. Ramesh, L. G. Salamanca-Riba, and L. J. Martınez-Miranda. "Depth profile study of ferroelectric $PbZr_{0.2}Ti_{0.8}O_3$ films". *J. Appl. Phys.* **92** 11 (2002).

[185] K. Saito, T. Kurosawa, T. Akai, T. Oikawa, and H. Funakubo. "Structural characterization and 90° domain contribution to ferroelectricity of epitaxial $Pb(Zr_{0.35},Ti_{0.65})O_3$ thin films". *J. Appl. Phys.* **93** 1 (2002).

[186] G. Xu, H. Hiraka, G. Shirane, J. Li, J. Wang, and D. Viehland. "Low symmetry phase in (001) $BiFeO_3$ epitaxial constrained thin films". *Appl. Phys. Lett.* **86** 18 (2005).

[187] H. W. Jang et al. "Domain Engineering for Enhanced Ferroelectric Properties of Epitaxial (001) $BiFeO_3$ Thin Films". *Adv. Mater.* **21** 7 (2009).

[188] Y.-H. Chu, Q. He, C.-H. Yang, P. Yu, L. W. Martin, P. Shafer, and R. Ramesh. "Nanoscale Control of Domain Architectures in $BiFeO_3$ Thin Films". *Nano Lett.* **9** 4 (2009).

[189] C. Thompson, D. D. Fong, R. V. Wang, F. Jiang, S. K. Streiffer, K. Latifi, J. A. Eastman, P. H. Fuoss, and G. B. Stephenson. "Imaging and alignment of nanoscale 180° stripe domains in ferroelectric thin films". *Appl. Phys. Lett.* **93** 18 (2008).

[190] R. Erni, M. D. Rossell, C. Kisielowski, and U. Dahmen. "Atomic-Resolution Imaging with a Sub-50-pm Electron Probe". *Phys. Rev. Lett.* **102** 9 (2009).

[191] G. Grüner. *Millimeter and Submillimeter Wave Spectroscopy of Solids*. Springer Berlin Heidelberg, 1998.

[192] S. Nashima, O. Morikawa, K. Takata, and M. Hangyo. "Measurement of optical properties of highly doped silicon by terahertz time domain reflection spectroscopy". *Appl. Phys. Lett.* **79** 24 (2001).

[193] D. M. A. Mackenzie, P. R. Whelan, P. Bøggild, P. U. Jepsen, A. Redo-Sanchez, D. Etayo, N. Fabricius, and D. H. Petersen. “Quality assessment of terahertz time-domain spectroscopy transmission and reflection modes for graphene conductivity mapping”. *Opt. Express* **26** 7 (2018).

[194] B. G. Alberding, W. Robert Thurber, and E. J. Heilweil. “Direct comparison of time-resolved terahertz spectroscopy and Hall Van der Pauw methods for measurement of carrier conductivity and mobility in bulk semiconductors”. *J. Opt. Soc. Am. B* **34** 7 (2017).

[195] M. P. Seah and W. A. Dench. “Quantitative electron spectroscopy of surfaces: A standard data base for electron inelastic mean free paths in solids”. *Surf. Interface Anal.* **1** (1979).

[196] V. Garcia et al. “Ferroelectric Control of Spin Polarization”. *Science* **327** 5969 (2010).

[197] J. J. Steffes, R. A. Ristau, R. Ramesh, and B. D. Huey. “Thickness scaling of ferroelectricity in $\mathrm{BiFeO_3}$ by tomographic atomic force microscopy”. *PNAS* **116** 7 (2019).

[198] A. M. Bratkovsky and A. P. Levanyuk. “Phase transitions and ferroelectricity in very thin films: homogeneous and inhomogeneous (domain) states”. *Integr. Ferroelectr.* **84** 1 (2006).

[199] D. Toyota et al. “Thickness-dependent electronic structure of ultrathin $\mathrm{SrRuO_3}$ films studied by in situ photoemission spectroscopy”. *Appl. Phys. Lett.* **87** 16 (2005).

[200] J. Xia, W. Siemons, G. Koster, M. R. Beasley, and A. Kapitulnik. “Critical thickness for itinerant ferromagnetism in ultrathin films of $\mathrm{SrRuO_3}$”. *Phys. Rev. B* **79** 14 (2009).

[201] X. Shen, X. Qiu, D. Su, S. Zhou, A. Li, and D. Wu. “Thickness-dependent metal-insulator transition in epitaxial $\mathrm{SrRuO_3}$ ultrathin films”. *J. Appl. Phys.* **117** (2015).

[202] G. Shibata et al. “Thickness-dependent ferromagnetic metal to paramagnetic insulator transition in $\mathrm{La_{0.6}Sr_{0.4}MnO_3}$ thin films studied by x-ray magnetic circular dichroism”. *Phys. Rev. B* **89** 23 (2014).

[203] Z. Liao, F. Li, P. Gao, L. Li, J. Guo, X. Pan, R. Jin, E. W. Plummer, and J. Zhang. “Origin of the metal-insulator transition in ultrathin films of $\mathrm{La_{2/3}Sr_{1/3}MnO}3$”. *Phys. Rev. B* **92** 12 (2015).

[204] Y. K. Vayunandana Reddy and D. Mergel. “Structural and electrical properties of $\mathrm{RuO_2}$ thin films prepared by rf-magnetron sputtering and annealing at different temperatures”. *J. Mater. Sci. Mater. Electron.* **17** 12 (2006).

[205] P. D. C. King, H. I. Wei, Y. F. Nie, M. Uchida, C. Adamo, S. Zhu, X. He, I. Božović, D. G. Schlom, and K. M. Shen. “Atomic-scale control of competing electronic phases in ultrathin $\mathrm{LaNiO_3}$”. *Nat. Nanotechnol.* **9** 6 (2014).

[206] M. Golalikhani et al. “Nature of the metal-insulator transition in few-unit-cell-thick $LaNiO_3$ films”. *Nat. Commun.* **9** 1 (2018).

[207] A. M. Bratkovsky and A. P. Levanyuk. “Very large dielectric response of thin ferroelectric films with the dead layers”. *Phys. Rev. B* **63** 13 (2001).

[208] A. Ojeda-G-P, C. W. Schneider, T. Lippert, and A. Wokaun. “Pressure and temperature dependence of the laser-induced plasma plume dynamics”. *J. Appl. Phys.* **120** 22 (2016).

[209] M. Lippmaa, N. Nakagawa, M. Kawasaki, S. Ohashi, and H. Koinuma. “Growth mode mapping of $SrTiO_3$ epitaxy”. *Appl. Phys. Lett.* **76** 17 (2000).

[210] P. Zubko, N. Stucki, C. Lichtensteiger, and J.-M. Triscone. “X-Ray Diffraction Studies of 180° Ferroelectric Domains in $PbTiO_3$/$SrTiO_3$ Superlattices under an Applied Electric Field”. *Phys. Rev. Lett.* **104** 18 (2010).

[211] P. Zubko, N. Jecklin, A. Torres-Pardo, P. Aguado-Puente, A. Gloter, C. Lichtensteiger, J. Junquera, O. Stéphan, and J.-M. Triscone. “Electrostatic Coupling and Local Structural Distortions at Interfaces in Ferroelectric/Paraelectric Superlattices”. *Nano Lett.* **12** 6 (2012).

[212] P. Zubko, N. Jecklin, N. Stucki, C. Lichtensteiger, G. Rispens, and J.-M. Triscone. “Ferroelectric Domains in $PbTiO_3$/$SrTiO_3$ Superlattices”. *Ferroelectrics* **433** 1 (2012).

[213] M. Hadjimichael, E. Zatterin, S. Fernandez-Peña, S. J. Leake, and P. Zubko. “Domain Wall Orientations in Ferroelectric Superlattices Probed with Synchrotron X-Ray Diffraction”. *Phys. Rev. Lett.* **120** 3 (2018).

[214] L. W. Martin and A. M. Rappe. “Thin-film ferroelectric materials and their applications”. *Nat. Rev. Mater.* **2** 16087 (2016).

[215] L. Li et al. “Observation of Strong Polarization Enhancement in Ferroelectric Tunnel Junctions”. *Nano Lett.* (2019).

[216] N. A. Pertsev and V. G. Koukhar. “Polarization Instability in Polydomain Ferroelectric Epitaxial Thin Films and the Formation of Heterophase Structures”. *Phys. Rev. Lett.* **84** 16 (2000).

[217] N. A. Pertsev, A. G. Zembilgotov, and A. K. Tagantsev. “Effect of Mechanical Boundary Conditions on Phase Diagrams of Epitaxial Ferroelectric Thin Films”. *Phys. Rev. Lett.* **80** 9 (1998).

[218] S. Prosandeev et al. *Ferroelectric Vortices and Related Configurations*. Wiley Online Books. 2016.

[219] J. Y. Jo, P. Chen, R. J. Sichel, S. J. Callori, J. Sinsheimer, E. M. Dufresne, M. Dawber, and P. G. Evans. “Nanosecond Dynamics of Ferroelectric/Dielectric Superlattices”. *Phys. Rev. Lett.* **107** 5 (2011).

[220] J. Park, J. Mangeri, Q. Zhang, M. H. Yusuf, A. Pateras, M. Dawber, M. V. Holt, O. G. Heinonen, S. Nakhmanson, and P. G. Evans. “Domain alignment within ferroelectric/dielectric $PbTiO_3/SrTiO_3$ superlattice nanostructures”. *Nanoscale* **10** 7 (2018).

[221] E. Bousquet, M. Dawber, N. Stucki, C. Lichtensteiger, P. Hermet, S. Gariglio, J.-M. Triscone, and P. Ghosez. “Improper ferroelectricity in perovskite oxide artificial superlattices”. *Nature* **452** (2008).

[222] S. R os, A. Ruediger, A. Q. Jiang, J. F. Scott, H. Lu, and Z. Chen. “Orthorhombic strontium titanate in $BaTiO_3$–$SrTiO_3$ superlattices”. *J. Phys. Condens. Matter* **15** 21 (2003).

[223] V. Stepkova, P. Marton, N. Setter, and J. Hlinka. “Closed-circuit domain quadruplets in $BaTiO_3$ nanorods embedded in a $SrTiO_3$ film”. *Phys. Rev. B* **89** 6 (2014).

[224] D. Peng, X. Yang, and W. Jiang. “Three-dimensional polarization vortex configuration evolution in compressed $BaTiO_3/SrTiO_3$ superlattice”. *J. Appl. Phys.* **126** 24 (2019).

[225] L. Lahoche, I. Luk’yanchuk, and G. Pascoli. “Stability of vortex phases in ferroelectric easy-plane nano-cylinders”. *Integr. Ferroelectr.* **99** 1 (2008).

[226] F. De Guerville, I. Luk’yanchuk, L. Lahoche, and M. El Marssi. “Modeling of ferroelectric domains in thin films and superlattices”. *Mater. Sci. Eng. B* **120** 1 (2005).

[227] Y. Liu, Y.-J. Wang, Y.-L. Zhu, C.-H. Lei, Y.-L. Tang, S. Li, S.-R. Zhang, J. Li, and X.-L. Ma. “Large scale two-dimensional flux-closure domain arrays in oxide multilayers and their controlled growth”. *Nano Lett.* **17** 12 (2017).

[228] I. Luk’yanchuk, Y. Tikhonov, A. Razumnaya, and V. M. Vinokur. “Hopfions emerge in ferroelectrics”. *Nat. Commun.* **11** 1 (2020).

[229] Y. Tikhonov et al. “Controllable skyrmion chirality in ferroelectrics”. *Sci. Rep.* **10** 1 (2020).

[230] M. Hadjimichael et al. “Metal–ferroelectric supercrystals with periodically curved metallic layers”. *Nat. Mater.* (2021).

[231] Y. Ahn, J. Park, A. Pateras, M. B. Rich, Q. Zhang, P. Chen, M. H. Yusuf, H. Wen, M. Dawber, and P. G. Evans. “Photoinduced Domain Pattern Transformation in Ferroelectric-Dielectric Superlattices”. *Phys. Rev. Lett.* **119** 5 (2017).

[232] K. Du, M. Zhang, C. Dai, Z. N. Zhou, Y. W. Xie, Z. H. Ren, H. Tian, L. Q. Chen, G. Van Tendeloo, and Z. Zhang. “Manipulating topological transformations of polar structures through real-time observation of the dynamic polarization evolution”. *Nat. Commun.* **10** 4864 (2019).

[233] X. Li et al. “Atomic-scale observations of electrical and mechanical manipulation of topological polar flux closure”. *PNAS* **117** 32 (2020).

[234] E. K. H. Salje. “Ferroelastic Materials”. *Annu. Rev. Mater. Res.* **42** (2012).

[235] N. Strkalj, M. Bernet, M. F. Sarott, J. Schaab, T. Weber, M. Fiebig, and M. Trassin. “Stabilization and manipulation of in-plane polarization in a ferroelectric|dielectric superlattice”. *Journal of Applied Physics* **129** 17 (2021).

[236] M. Dawber, N. Stucki, C. Lichtensteiger, S. Ganglio, P. Ghosez, and J. M. Triscone. “Tailoring the properties of artificially layered ferroelectric superlattices”. *Adv. Mater.* **19** 23 (2007).

[237] V. G. Koukhar, N. A. Pertsev, and R. Waser. “Thermodynamic theory of epitaxial ferroelectric thin films with dense domain structures”. *Phys. Rev. B* **64** 21 (2001).

[238] V. G. Kukhar, N. A. Pertsev, H. Kohlstedt, and R. Waser. “Polarization states of polydomain epitaxial PbZr$_{1-x}$Ti$_x O_3$ thin films and their dielectric properties”. *Phys. Rev. B* **73** 21 (2006).

[239] Z. Gu et al. “Resonant domain-wall-enhanced tunable microwave ferroelectrics”. *Nature* **560** 7720 (2018).

[240] E. Khestanova, N. Dix, I. Fina, M. Scigaj, J. M. Rebled, C. Magén, S. Estradé, F. Peiró, G. Herranz, and J. Fontcuberta. “Untangling Electrostatic and Strain Effects on the Polarization of Ferroelectric Superlattices”. *Adv. Funct. Mater.* **26** 35 (2016).

[241] R. Ramesh and D. G. Schlom. “Creating emergent phenomena in oxide superlattices”. *Nat. Rev. Mater.* **4** 4 (2019).

[242] V. A. Stephanovich, I. A. Luk’yanchuk, and M. G. Karkut. “Domain-Enhanced Interlayer Coupling in Ferroelectric/Paraelectric Superlattices”. *Phys. Rev. Lett.* **94** 4 (2005).

[243] N. Balke, M. Gajek, A. K. Tagantsev, L. W. Martin, Y.-H. Chu, R. Ramesh, and S. V. Kalinin. “Direct Observation of Capacitor Switching Using Planar Electrodes”. *Adv. Funct. Mater.* **20** 20 (2010).

[244] J. Zhou et al. “Directed assembly of nano-scale phase variants in highly strained BiFeO$_3$ thin films”. *J. Appl. Phys.* **112** 6 (2012).

[245] J. Nordlander et al. “Ferroelectric domain architecture and poling of BaTiO$_3$ on Si”. *Phys. Rev. Mater.* **4** 3 (2020).

[246] E. Gradauskaite, M. Campanini, B. Biswas, C. W. Schneider, M. Fiebig, M. D. Rossell, and M. Trassin. “Robust In-Plane Ferroelectricity in Ultrathin Epitaxial Aurivillius Films”. *Adv. Mater. Interfaces* **7** 2000202 (2020).

[247] J. Guyonnet, H. Béa, and P. Paruch. “Lateral piezoelectric response across ferroelectric domain walls in thin films”. *J. Appl. Phys.* **108** 4 (2010).

[248] H. Béa, B. Ziegler, M. Bibes, A. Barthélémy, and P. Paruch. “Nanoscale polarization switching mechanisms in multiferroic BiFeO3thin films”. *J. Phys. Condens. Matter* **23** 14 (2011).

[249] O. Nesterov, S. Matzen, C. Magen, A. H. G. Vlooswijk, G. Catalan, and B. Noheda. “Thickness scaling of ferroelastic domains in $PbTiO_3$ films on $DyScO_3$”. *Appl. Phys. Lett.* **103** 14 (2013).

[250] G. Catalan, H. Béa, S. Fusil, M. Bibes, P. Paruch, A. Barthélémy, and J. F. Scott. “Fractal Dimension and Size Scaling of Domains in Thin Films of Multiferroic $BiFeO_3$”. *Phys. Rev. Lett.* **100** 2 (2008).

[251] M. Mtebwa, L. Feigl, P. Yudin, L. J. McGilly, K. Shapovalov, A. K. Tagantsev, and N. Setter. “Room temperature concurrent formation of ultra-dense arrays of ferroelectric domain walls”. *Appl. Phys. Lett.* **107** 14 (2015).

[252] L. J. McGilly, A. Schilling, and J. M. Gregg. “Domain Bundle Boundaries in Single Crystal $BaTiO_3$ Lamellae: Searching for Naturally Forming Dipole Flux-Closure/Quadrupole Chains”. *Nano Lett.* **10** 10 (2010).

[253] L. Feigl, P. Yudin, I. Stolichnov, T. Sluka, K. Shapovalov, M. Mtebwa, C. S. Sandu, X.-K. Wei, A. K. Tagantsev, and N. Setter. “Controlled stripes of ultrafine ferroelectric domains”. *Nat. Commun.* **5** 1 (2014).

[254] P. Sharma, Q. Zhang, D. Sando, C. H. Lei, Y. Liu, J. Li, V. Nagarajan, and J. Seidel. “Nonvolatile ferroelectric domain wall memory”. *Sci. Adv.* **3** 6 (2017).

[255] P. S. Bednyakov, B. I. Sturman, T. Sluka, A. K. Tagantsev, and P. V. Yudin. “Physics and applications of charged domain walls”. *npj Comput. Mater.* **4** 1 (2018).

[256] J. Schaab et al. “Electrical half-wave rectification at ferroelectric domain walls”. *Nat. Nanotechnol.* **13** 11 (2018).

[257] J. A. Mundy et al. “Functional electronic inversion layers at ferroelectric domain walls”. *Nat. Mater.* **16** 6 (2017).

Data

Data presented in this thesis is archived at

\3-PhD\2021\NStrkalj\Data

in the Ferroic Results directory. A zipped archive is also available in ETH Zurich's Research Collection. The folders are organized according to the chapters of the thesis. Illustrations are provided as svg files. Where applicable, the Origin file and the dat file containing the plotted data are provided. Images are provided in tiff format.